



Cite this: *Mater. Adv.*, 2020, **1**, 1506

Catalytic conversion of CO₂ to chemicals and fuels: the collective thermocatalytic/photocatalytic/electrocatalytic approach with graphitic carbon nitride

Subhajyoti Samanta * and Rajendra Srivastava *
(✉) subhajyoti.samanta@iitrpr.ac.in, rajendra@iitrpr.ac.in

Rapid industrial development and the excessive use of fossil fuels have produced a significantly large volume of CO₂ in the atmosphere. The efficient conversion of CO₂ to useful chemicals and fuels is an important step towards reducing the concentration of CO₂. To overcome the thermodynamic and kinetic barriers involved in CO₂ activation and conversion, an effective heterogeneous catalyst and a suitable form of energy, such as thermal, photochemical, and electrochemical, are necessary. Considering a wide variety of catalytic materials for CO₂ conversion using all forms of energy resources discussed above, earth-abundant carbon materials have exhibited the capability to catalyze the thermal, photo-assisted, and electrochemically mediated conversion of CO₂. Among carbon-based materials, graphitic carbon nitride (g-C₃N₄) is an inexpensive and sustainable catalyst that can be effectively used for CO₂ conversion. The chemical reactivity and optoelectronic properties of g-C₃N₄ can be finely tailored for its use as a conventional catalyst or photocatalyst or photoelectrocatalyst. This article aims to summarize the synthetic strategies to prepare various types of g-C₃N₄ materials as conventional catalysts/photocatalysts/electrocatalysts for the improved conversion of CO₂ to chemicals and fuels. This article reviews the utilization of CO₂ as a feedstock for chemical and fuel synthesis *via* insertion, carboxylation, and reduction reactions. Further, an in-depth understanding of the catalytic mechanism of various reactions discussed in this article will help in the design of a new generation of heterogeneous catalysts for CO₂ conversion. Special emphasis is placed on the various parameters influencing the photocatalytic and electrocatalytic CO₂ reduction. Finally, the underlying challenges and outlook for the future development of catalysts for CO₂ conversion to specialty chemicals and fuels are discussed.

Received 10th May 2020,
 Accepted 15th June 2020

DOI: 10.1039/d0ma00293c

rsc.li/materials-advances

1. Introduction

CO₂ is one of the major variable components in the troposphere that significantly influence human life.¹ A large amount of CO₂ is present in the soil as CaCO₃. However, only gaseous CO₂ present in the troposphere is responsible for global warming. The effect of carbon dioxide on Earth is being discussed at every forum and international meeting.^{2,3} A closer look reveals that several activities by millions of living entities (plants, animals, and human beings) have raised the CO₂ level in the atmosphere by 280 ppm in the last few centuries. However, after the industrial revolution, the CO₂ level in the atmosphere has risen from 280 ppm to 400 ppm and it is expected to reach up to 500 ppm by the 22nd century, which would raise the mean

temperature of the Earth by 1.9 °C.⁴ Today, each and every second of our life is dependent on energy resources. The energy dependency can be taken care of with the use of renewable and alternative resources such as wind, water, radioactive, and solar energy, which do not increase the CO₂ level in the atmosphere and provide a CO₂ emission-free environment.⁵ In recent times, several alternative energy generation systems, such as fuel cells, are being developed which do not emit CO₂.⁷ However, the H₂ required in fuel cells is produced by steam reforming, which produces a large amount of CO₂ in the atmosphere.⁶ Future energy demands and current technologies suggest that it is a long journey and by that time a significant amount of CO₂ will be released into the atmosphere. If the CO₂ concentration increases beyond 600 ppm it would be difficult for human beings to breathe because it is difficult for the human respiratory system to operate in the presence of a greater concentration of CO₂ even though an excess of O₂ is present in the atmosphere. Thus, there is a high priority in developing strategies to reduce the CO₂ concentration in the environment. This can be achieved *via* two

Catalysis Research Laboratory, Department of Chemistry, Indian Institute of Technology Ropar, Rupnagar, Punjab-140001, India.
E-mail: subhajyoti.samanta@iitrpr.ac.in, rajendra@iitrpr.ac.in;
Tel: +91-1881-242175



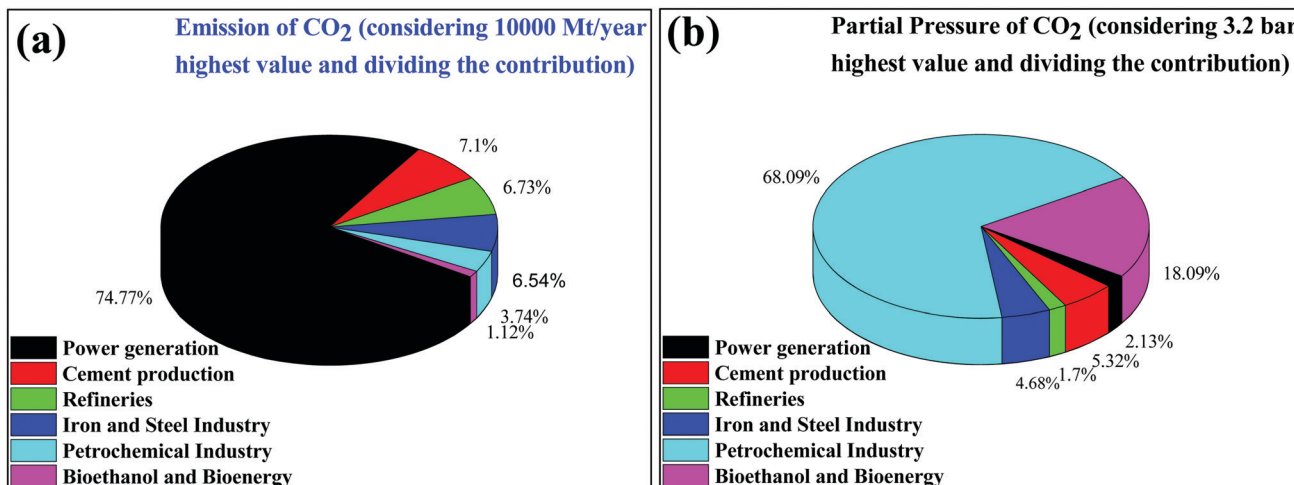


Fig. 1 (a) Emission of CO₂ and (b) partial pressure of CO₂ emitted from different stationary sources.

strategies: (1) CO₂ capture and storage (CCS) and (2) CO₂ capture and utilization (CCU) to useful chemicals and fuels.⁷ This article is focused on the CO₂ conversion to useful chemicals and fuels; therefore, only a brief discussion is provided for CO₂ capture and storage.

The various types of stationary plants and their corresponding CO₂ emission (amount and partial pressure) are summarized in pie charts (Fig. 1). It is very easy to capture CO₂ from point sources where the CO₂ concentration is high but it is very difficult to capture CO₂ from low concentration sites, such as on city roads

or houses where the concentration ranges fall at the ppm level.⁸ Besides being the most desirable task, direct CO₂ capture and storage are undoubtedly challenging.^{9,10} In general, liquid CO₂ scrubbers and metal oxides are used to absorb CO₂ from flue gases.^{11–20} Aqueous amine based liquid CO₂ scrubbers are commonly used but their associated energy consumption and cost remain a constraint for further development.⁹ Similarly, solid materials such as alkali metal oxides, layered double hydroxides, solid amines, etc. are widely explored materials for CO₂ adsorption.¹⁴ However, CO₂ absorption using the CO₂



Subhajyoti Samanta

Mr Subhajyoti Samanta received his Master of Science in Chemistry from Guru Ghasidas Central University, Chhattisgarh, India in 2011 after completion of his bachelor's degree with honors in Chemistry from Vidyasagar University, West Bengal, India in 2009. Since July 2014, he has been working under the supervision of Dr Rajendra Srivastava in the Department of Chemistry at the Indian Institute of Technology Ropar (IIT Ropar), Punjab, India.

Prior to joining his Ph.D. research, he had also worked as a project Junior Research Fellow at CSIR-IIMT, Bhubaneswar, India (June 2013–January 2014). His research concentration circumvents the area of nano-engineering metal oxides and their composites with carbon materials for their applications in heterogeneous catalysis. He has particularly developed materials for a variety of photocatalytic oxidation reactions, CO₂ reduction, and water oxidation by both electrocatalytic and photocatalytic methods. He has published 15 research articles in the Journals of International repute to his credit. He has also been recognized as a young scientist and participated in the Global Young Scientist Summit-2020, Singapore.



Rajendra Srivastava

Dr Rajendra Srivastava joined the Department of Chemistry, IIT Ropar in 2009 as an Assistant Professor, headed the department from March 2015 to May 2018, and is currently working as an Associate Professor. He acquired his Ph.D. degree from CSIR-National Chemical Laboratory, Pune, India where his doctoral work won him the best thesis award of 2006, conferred by the Catalysis Society of India. Afterward, he worked as a postdoctoral research fellow in KAIST, South Korea (2005–2007) and as a JSPS fellow in the Hokkaido University, Japan (2007–2009). He received the NASI-SCOPUS Young Scientist Award 2017, The Catalysis Society of India Young Scientist Award 2018, and Mid-career Faculty Research and Innovation Award 2019 by IIT Ropar. His fields of interest include designing and synthesis of nanostructured functional materials for catalytic applications, including electrocatalysis (actuators, sensors, supercapacitors and energy harvesters), and photocatalysis. He has published more than 130 peer-reviewed original research articles in reputed international journals and has filed 8 patents.



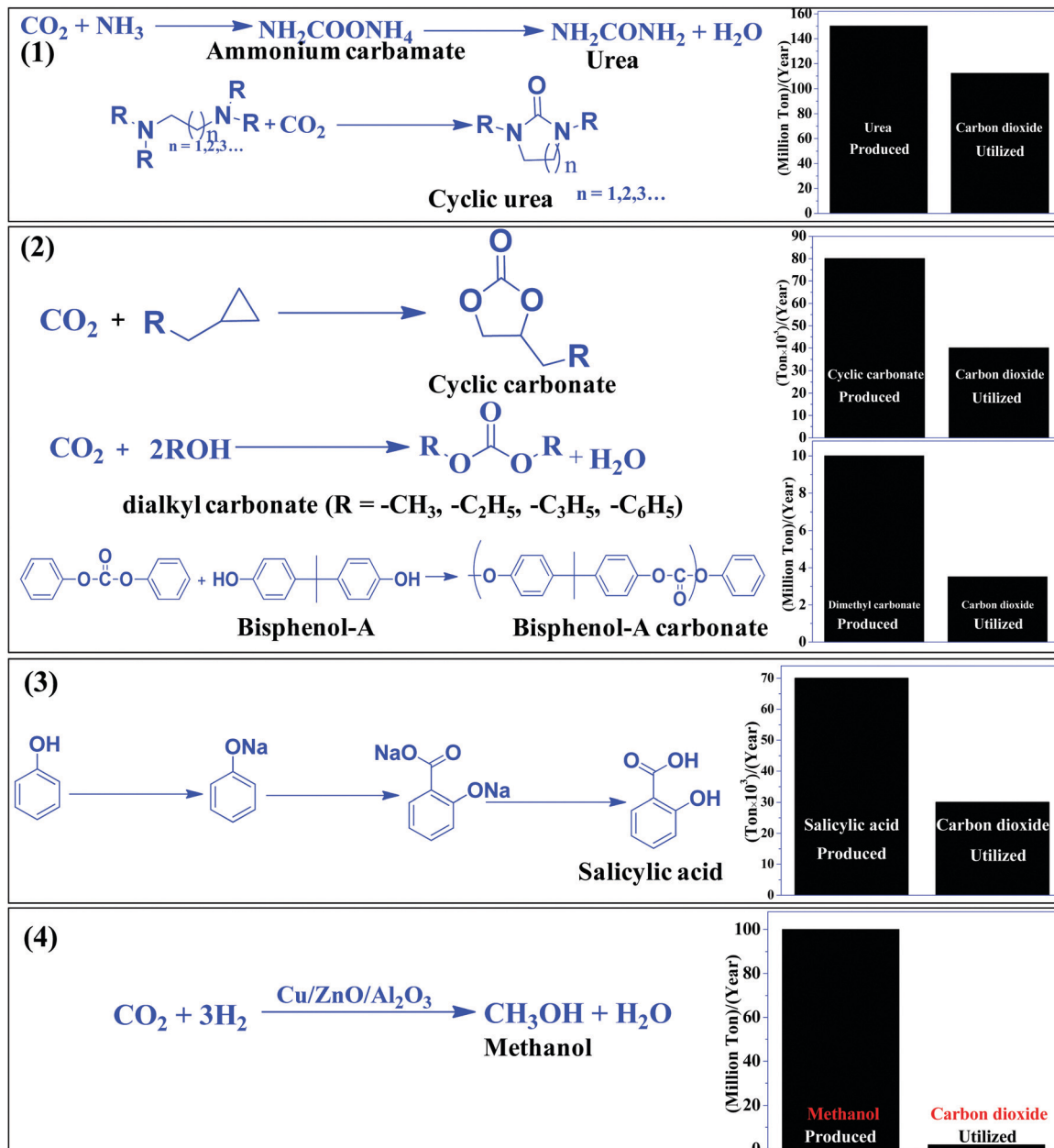
scrubbers and solid materials discussed above is energetically reversible due to the strong bonding of CO_2 to these materials. Several types of nanoporous materials based on zeolites,^{17,18} metal-organic frameworks,^{17–19} and carbon^{20,21} have been developed for this purpose. All of those above-mentioned materials have functional amines and metal sites for the efficient adsorption of CO_2 over other gases present in flue gas. Apart from tuning the chemical properties, tailoring textural properties such as the surface area, pore size and porous architecture can improve the CO_2 adsorption capabilities. It is noteworthy that materials having a pore size greater than 0.33 nm and lower than 0.35 nm would be ideal for CO_2 adsorption over other gases present in flue gas (the kinetic diameters of CO_2 , O_2 , and N_2 are 0.33 nm, 0.345 nm, and 0.36 nm, respectively).²² However, such a fine porous material with specific requirements is yet to be developed. Therefore, high surface area materials having dense CO_2 adsorption sites with pore sizes in the range of 0.3 to 2 nm are being prepared.^{20,23,24} Thus the direct capture of CO_2 from the air (in which the O_2/CO_2 ratio is more than 500 or even more) is very demanding but challenging for research scientists and engineers. However, plants do this job very efficiently when the present CO_2 level is <400 ppm. Plants abstract CO_2 from the atmosphere and convert it to carbohydrate with the aid of sunlight and grow and liberate O_2 .

The most efficient strategy to reduce the concentration of CO_2 in the atmosphere is to convert CO_2 to useful chemicals and fuels. CO_2 is a thermodynamically inert molecule with a high C=O bond dissociation energy of 750 kJ mol⁻¹ which is much higher than the C–O bond (327 kJ mol⁻¹) and even higher than the C–C (336 kJ mol⁻¹) and C–H (441 kJ mol⁻¹) bonds.²⁵ Due to such high stability, it is difficult to transform CO_2 into useful chemicals. The energy gap between its highest occupied molecular orbital and lowest unoccupied molecular orbital is 13.7 eV and the electron affinity of CO_2 is (-0.6 ± 0.2 eV), which leads to a very negative redox potential for one-electron transfer $\text{CO}_2 + \text{e}^- \rightarrow \text{CO}_2^-$ ($E_{\text{redox}}^0 = -1.90$ eV vs. NHE).^{26,27} Such a high energy requirement for electron transfer to generate active species for CO_2 conversion makes photocatalytic and electrocatalytic processes highly challenging tasks. Due to such a high energy requirement, only a few chemicals have been commercialized, which utilizes a large amount of CO_2 to give useful chemicals such as urea, methanol, salicylic acid, cyclic carbonates, and dimethyl carbonate (Scheme 1). Synthesis of urea and cyclic urea is not a 100% atom economic process because water is formed as a by-product. In an atom economic process, the total number of atoms present in the reactants is incorporated into the product. Synthesis of cyclic carbonates takes place by an insertion reaction in which CO_2 is inserted into a three-membered epoxide ring to produce a five-membered cyclic carbonate *via* a 100% atom economic process.^{28,29} Dimethyl carbonate (DMC), a solvent, can be produced by the reaction of methanol and CO_2 .^{30,31} DMC reacts with phenol using a $\text{Pb}(\text{OPh})_2$ catalyst to produce diphenyl carbonate (DPC). Then DPC reacts with bisphenol-A to produce a polycarbonate *via* a melt polymerization method (Scheme 1).³² Salicylic acid is manufactured

by the reaction of phenol and CO_2 in a strongly basic medium.³³ Another bulk chemical is methanol, which is produced annually at a rate of 100 million tons by utilizing 2 million tons of CO_2 ³⁴ (Scheme 1). Industrial processes for chemical synthesis using CO_2 as a reactant are operated at high temperature and pressure due to the thermodynamic stability and inertness of CO_2 . Such reactions can be catalyzed under mild conditions if the CO_2 is efficiently activated. Since CO_2 is an acidic molecule, therefore it can be activated using basic catalysts such as alkali and alkaline earth metal-based oxides and hydroxides. Various organic amines (N-heterocyclics, DBU, guanidine, melamine, phthalocyanine, and porphyrins) and polyamines have also been used in chemical synthesis utilizing CO_2 as the reactant. In general, organic amines are more reactive than inorganic bases and thus various ionic liquids, metal-organic frameworks, silica, and zeolite based materials with functional amine groups have been utilized for chemical synthesis involving CO_2 as a reactant. Nitrogen-containing carbon materials, such as carbon nitrides, are a unique class of materials which can be prepared with economical nitrogen and carbon-containing precursors. Since these materials have a large nitrogen content, they can be used for CO_2 activation and adsorption.

In this review, we will present the advances, challenges, and prospects of carbon nitride based catalysts, photocatalysts, and electrocatalysts in CO_2 conversion to chemicals and fuels. After a brief introduction to CO_2 conversion, the requirements of CO_2 storage and conversion, the industrial process for CO_2 to chemicals, and the types of materials required for CO_2 activation and conversion are described in Section 1. Sections 2–6 focus on carbon nitride-based catalysts in the conventional catalytic conversion of CO_2 to chemicals and photocatalytic and electrocatalytic conversion of CO_2 to C_1 fuels. Section 2 presents a brief description of nitrogen-containing carbon-based materials, types of carbon nitride, and the structural elucidation of $\text{g-C}_3\text{N}_4$ for catalytic applications. Section 3 deals with the synthesis strategy adopted for the preparation of $\text{g-C}_3\text{N}_4$ for improved catalysis and photocatalysis involving CO_2 as a reactant. Sections 4 and 5 provide detailed information about photocatalytic and electrocatalytic CO_2 conversion to C_1 fuels, respectively, their basic concepts, the influence of various parameters influencing the CO_2 conversion and C_1 fuel selectivity, deep insight into the reaction mechanisms *via* *in situ* characterization techniques and product identification, catalytic activity assessment and result presentation, and the experimental set-up required for photocatalytic and electrocatalytic measurements. Finally, this review will be concluded with a summary, underlying challenges, and opportunities for the future development of catalysts for CO_2 conversion to chemicals and fuels.

This focused review aims to concisely cover almost all the important points, starting from the requirements of CO_2 conversion, fundamentals of CO_2 activation, strategies adopted for $\text{g-C}_3\text{N}_4$ preparation for improved CO_2 conversion, structure elucidation of $\text{g-C}_3\text{N}_4$, and structure–activity relationship, followed by critical operational parameters for collective ‘thermo-photo-electro’-chemical CO_2 conversion focusing on the $\text{g-C}_3\text{N}_4$ catalyst,



Scheme 1 CO_2 based commercial processes and amount of CO_2 utilized vs. product formed in the given process.

which is not available in a single article hitherto reported in the literature.

2. Carbon nitride, a versatile material for CO_2 adsorption and conversion: structural elucidation for catalysis

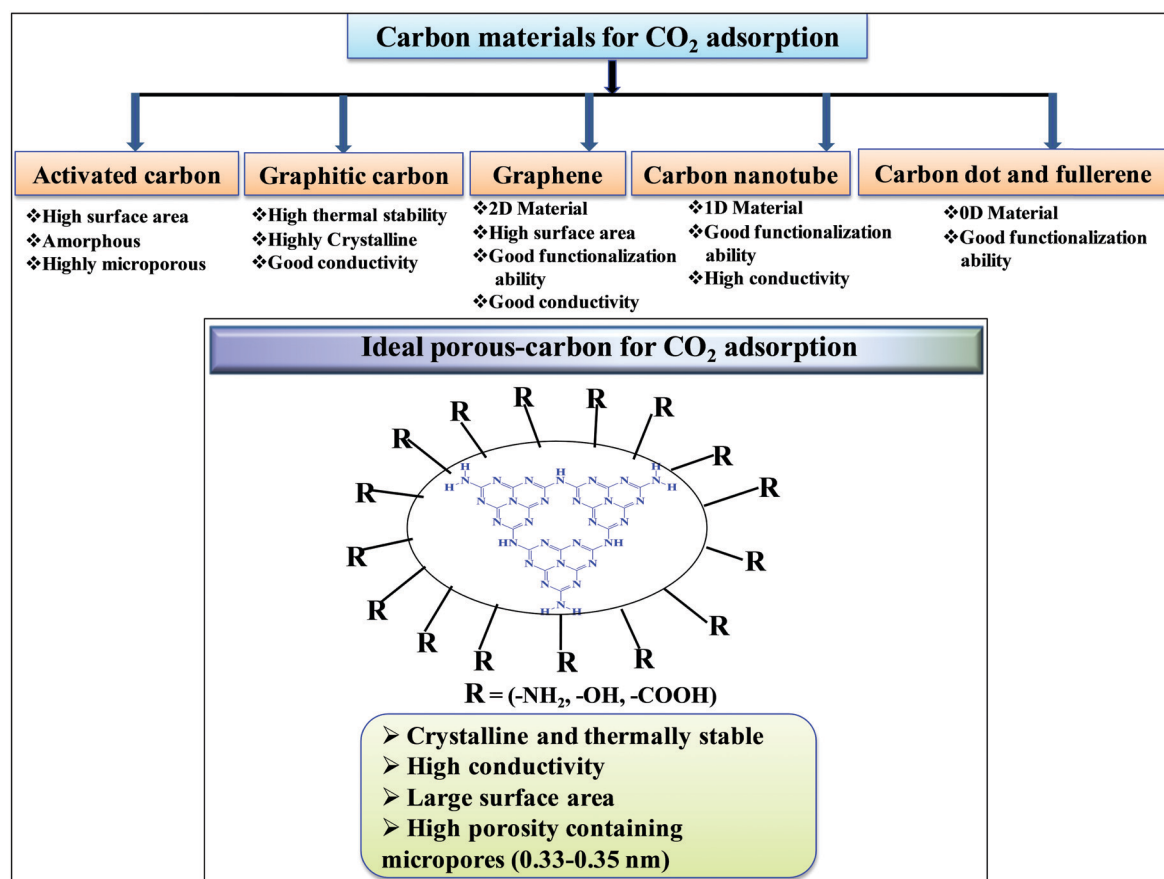
Among porous materials, carbon materials have a high surface area, tunable porosity, hydrophobicity for CO_2 adsorption under hydrated conditions, high thermal and chemical stability, and functional ability.³⁵⁻³⁷ Activated carbon is the most economical and widely available carbon material having micropores,

mesopores, and macropores.³⁸ Due to the porous architecture and high surface area, it can significantly adsorb large amounts of CO_2 by the physisorption process but it finds difficulty in the activation and utilization of CO_2 in chemical synthesis due to the inability to chemisorb and activate CO_2 .³⁹ Biomass pyrolysis and KOH activation can produce high surface area activated carbon, suitable for CO_2 physisorption.⁴⁰ N-Doped micro-porous carbon prepared with coconut shell and urea has exhibited high CO_2 adsorption and CO_2/N_2 selectivity at 1 bar, confirming that N-doping has improved the CO_2 adsorption.⁴¹ Similar to inorganic porous materials, sol-gel methods have been applied for the synthesis of porous carbon materials in water and/or ethanol medium followed by acid activation



leading to the formation of porous carbon with high surface area and pore volume.^{42,43} Hydrothermal polymerization is employed to prepare porous carbon materials with higher surface area after chemical activation.⁴⁴ The hydrothermal method provides the opportunity to prepare carbon materials with functionalized carbon in the presence of other functional organic compounds. Such functionalized materials (carboxyl rich carbon materials) have exhibited high CO₂ capture performances at 1 bar and under flue gas conditions.⁴⁵ Hard template⁴⁶ and soft template⁴⁷ methods have been developed for the preparation of mesoporous carbon. The carbon materials discussed above are amorphous porous carbon. It is also possible to synthesize crystalline carbon materials with different allotropy. 0D carbon dots and fullerenes, 1D carbon nanotubes, 2D graphene, and 3D graphite are the various allotropic forms of carbon materials (Scheme 2). In general 3D graphitic carbon can be prepared by heating a carbon precursor at a very high temperature 2000–3000 °C. However, such graphitic carbon possesses very low surface area and porosity. Metal catalyst mediated synthesis produces graphitic carbon at a very low temperature of 700–800 °C with higher surface area and porosity.⁴⁸ Moreover, microwave mediated, metal activated synthesis produces graphitic carbon with very high surface area and porosity.⁴⁹ Graphene, carbon nanotubes, and fullerenes have been prepared under varying controlled conditions using a unique vapor deposition method

in the presence and absence of metal catalysts. Due to the high surface area and surface to volume ratio, these materials can be easily functionalized using various amines for the efficient adsorption of CO₂.^{50,51} These porous carbons have varied surface area, morphology, and porosity and, thus, the extent of CO₂ adsorption over these materials varies depending on their tunable textural properties. However, the adsorption and chemisorption capability improves if nitrogen-doped or nitrogen-containing carbon materials are considered. Nitrogen-containing carbon materials induce interactive forces between CO₂ and nitrogen groups present in the material. CO₂ is a weak Lewis acidic molecule because the carbon atom in CO₂ is electron-deficient. Nitrogen-doped carbon atoms are negatively charged and nitrogen sites act as electron donors and behave like a Lewis base; therefore, nitrogen-containing carbon materials have acid–base interactions through which CO₂ molecules are chemisorbed. The strong dipolar C=O bond generates an electric quadrupole moment in the CO₂ molecule, whereas nitrogen doping induces local polarization in the porous carbon matrix.⁵² Notably, N₂ has a lower electric dipole moment than CO₂. Hence, the interaction between the CO₂ molecular quadrupole moment and high electrostatic potential of N-doped carbons enhances the CO₂ adsorption energy, leading to selective and higher CO₂ adsorption from flue gases. Experimental and computational studies have shown that surface hydroxyl



Scheme 2 Porous carbon materials for CO₂ adsorption.



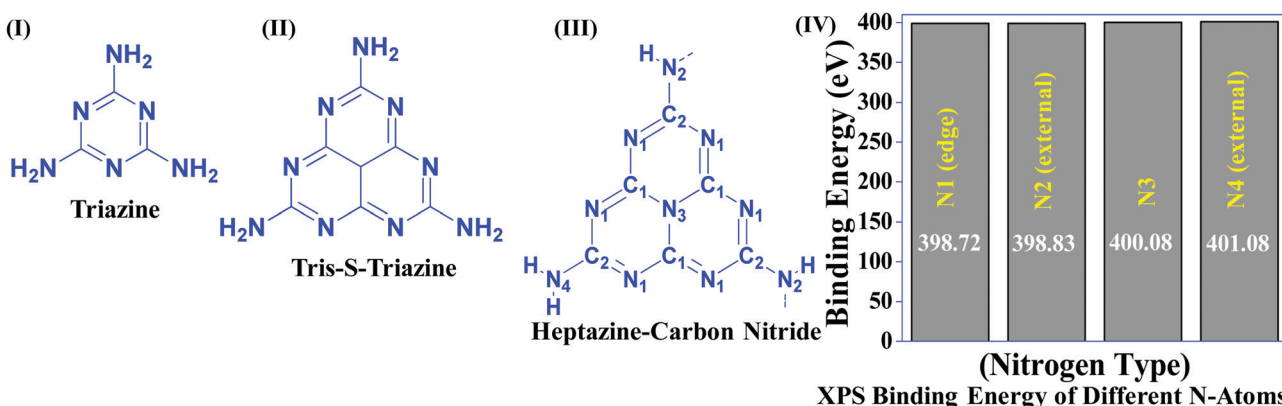
Table 1 Nitrogen-containing carbon materials and their CO₂ uptake capacity⁴⁴

E. no.	Material	S _{BET} (m ² g ⁻¹)	Nitrogen content (%)	CO ₂ uptake mmol ⁻¹ g ⁻¹ (298 K)
1	NMC-600	272	6.33	3.90
2	NMC-700	518	6.06	3.60
3	AC-600-0.5	508	6.70	3.00
4	AC-600-2	966	4.50	3.64
5	AC-800-2	2448	3.90	3.00
6	Sk-0.5-700	1060	0.48	4.24
7	SK-4-700	2792	0.18	3.05
8	PGC-K	1143	8.30	4.00
9	FCP-1-KC	800	0.60	5.20

groups present in the N-doped carbon skeleton enhance the interaction between –OH and –NH functionalities leading to high CO₂ adsorption in N-doped carbon materials.⁵³ Nitrogen doping and surface functionalized amines have different types of interaction. Surface functionalized amines interact with electropositive carbon of CO₂ and form ammonium carbamate leading to high CO₂ adsorption on the surface.⁵⁴ However, surface and pore blockage and thermal instability of functionalized amines are some of the demerits of surface amine-functionalized carbon materials; therefore, nitrogen-doped carbon is superior over amine-functionalized carbon materials. Based on the varied textural properties and chemical properties (due to N doping and amine functionalization), it can be concluded that high surface area and high nitrogen contents both are important factors contributing to high CO₂ adsorption (Table 1).⁴⁴ Moreover, when CO₂ activation and utilization for chemical synthesis are considered both these factors play important roles.

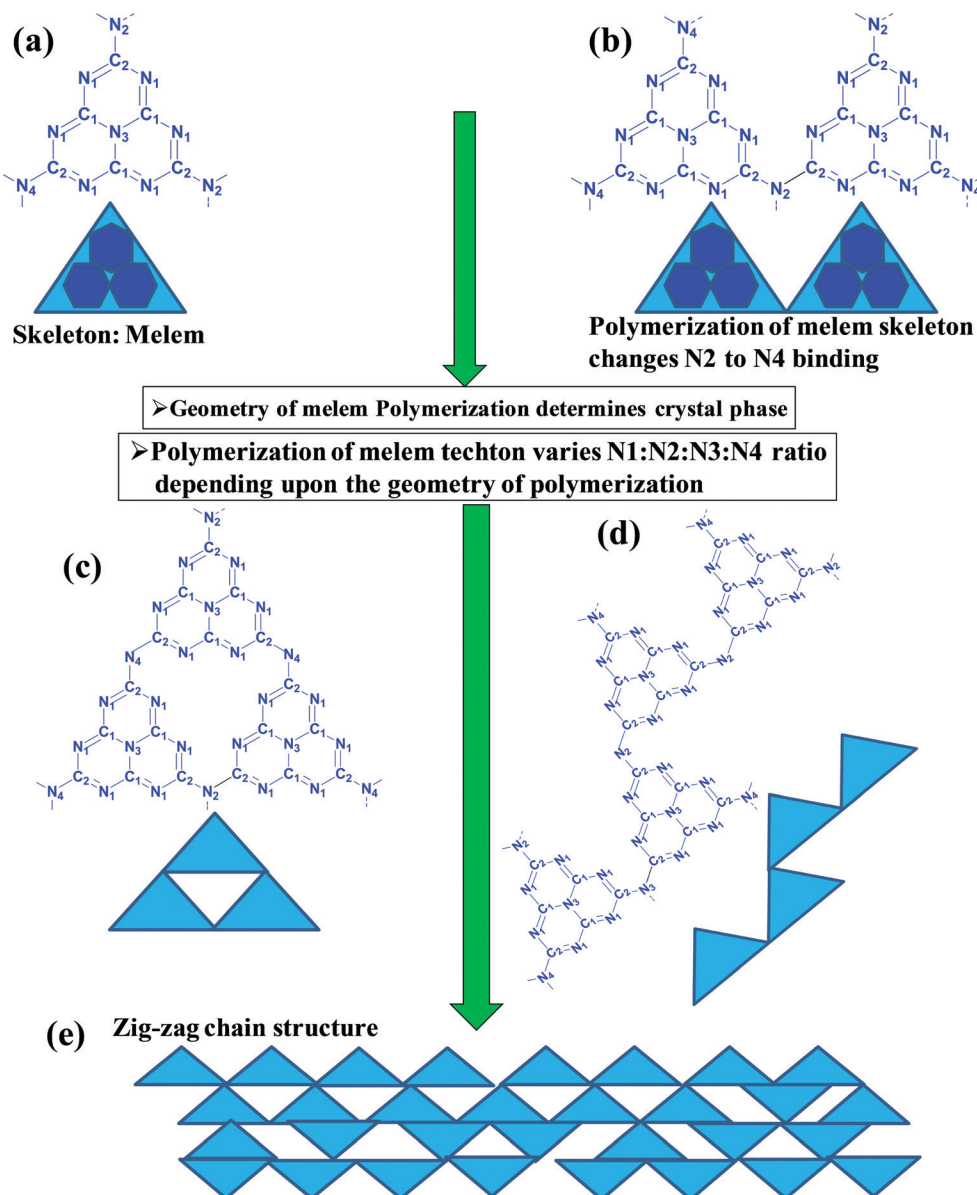
Table 1 suggests that a large number of framework substituted N atoms in a carbon matrix is required for high CO₂ adsorption. The graphitic carbon framework provides high thermal stability and conductivity, which would be good for photocatalysis and electrocatalysis. An ideal porous carbon material and its properties are listed in Scheme 2. Based on these characteristic features, a unique carbonaceous material known as graphitic carbon nitride (g-C₃N₄) can best serve this purpose. When a simple nitrogen-rich organic compound (such as urea, melamine, cyanamide, dicyandiamide, etc.) is thermally-

polymerized in the temperature range of 500–700 °C, it produces carbon nitride. This material was synthesized way back in 1834 by Berzelius;⁵⁵ however its potential as a catalyst⁵⁶ and photocatalyst⁵⁷ was realized in 2006 and 2009, respectively. This crystalline material exists in seven allotropes: α -C₃N₄, β -C₃N₄, cubic C₃N₄, pseudocubic C₃N₄, *g-h*-triazine, *g-o*-triazine, and *g-h*-heptazine with bandgaps of 5.49, 4.85, 4.30, 4.13, 2.97, 0.93, and 2.88 eV, respectively.⁵⁸ These allotropes vary in their nitrogen environment and nitrogen contents. Theoretically, carbon nitride is predicted to have a C/N ratio of 0.75 without any surface functional groups and hydrogen content but the reality is far from this prediction. Carbon nitrides have been actually obtained with varied C/N ratios using different nitrogen-containing organic compounds at varied reaction temperature. It is possible to synthesize carbon nitrides such as C₃N, C₃N₂, C₁₀N₃, C₅N, C₃N₅, C₃N₆, C₃N₇, etc., having different nitrogen contents than the theoretically predicted ideal C₃N₄ and those are termed as nitrogen-rich (C/N < 0.75) and nitrogen lean (C/N > 0.75) C₃N₄.⁵⁹ Whenever a six-membered conducting atomic-scaffold is envisaged, structures such as those of benzene or borazine pop-up in our minds. Based on this perception, the triazine-like structure of C₃N₄ can be predicted (Scheme 3(I)). But it has been found that triazine or tri-*s*-triazine units (Scheme 3(II)) (also known as tectonic units) propagate in three dimensions to produce allotropes of g-C₃N₄ (Scheme 3). Computational studies based on Density Functional Theory (DFT) suggest that the tri-*s*-triazine unit is more stable than the triazine unit by 30 J mol⁻¹.⁶⁰ Later, 2,5,8-triamine, tri-*s*-triazine (C₆N₁₀H₆) has been isolated, which confirms the building units of g-C₃N₄.⁶¹ Theoretical g-C₃N₄ should have an ideal C/N ratio of 0.75 and should not possess any H or O atoms; however, XPS and elemental analysis suggest that it has H and O atoms in small quantities in addition to C and N. Notably, H and O atoms are observed due to terminal amine groups and surface adsorbed water and (C=O), (O–N), and (C–OH) groups, for which the details are provided in Scheme 3. Various types of C and N are designated in one pictorial representation of a terminal tri-*s*-triazine unit of g-C₃N₄ (Scheme 3). The structure clearly shows that it has two different types of C represented as C1 and C2 (Scheme 3(III)). Similarly, four different types of

**Scheme 3** Chemical structure of (I) triazine, (II) tris-*s*-triazine, and (III) heptazine units of carbon nitride, and (IV) various N types and their binding energies.

nitrogen atoms are designated as N1 (pyridinic), N2, N3 (graphitic-N), and N4 (Scheme 3(III)). They can be easily distinguished from XPS analysis due to different electronic environments that provide different binding energies (Scheme 3(IV)).⁶²

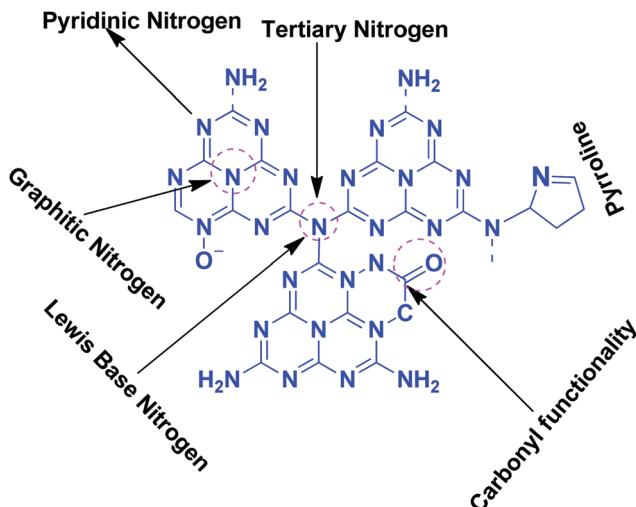
In a true heptazine building unit (also known as melem), N2 is absent and N1 : N3 : N4 should be present in the ratio 6 : 1 : 3 (Scheme 4a). When the melem monomer polymerizes, the N4-type of nitrogens are converted to the N2-type (Scheme 4b).



Sl. No.	N1	N2	N3	N4	N1 %	N2 %	N3 %	N4 %
Dimer	12	1	2	4	63.16	5.26	10.52	21.05
Tetramer	12	1	2	3	66.66	5.55	11.11	16.67
Octamer	12	1	2	2.5	68.85	5.71	11.43	14.28
Infinite chain	12	1	2	2	70.58	5.88	11.76	11.76

Scheme 4 Evolution of different geometry and N types present in C_3N_4 based on the variation of the linkages of melem units.⁵³





Scheme 5 Different types of N and O functionalities present in $\text{g-C}_3\text{N}_4$.

The N4/N2 ratio in the melem framework depends on the propagating direction to form $\text{g-C}_3\text{N}_4$ (Scheme 4c). Moreover, the stability of $\text{g-C}_3\text{N}_4$ also varies depending on the geometry of the final $\text{g-C}_3\text{N}_4$ polymer. When melem units are linked and form dimers, tetramers, octamers, and infinite chains, then the % N1 contribution increases. Moreover, the percentage of different N-types varies based on the geometry of their linkages as shown in Scheme 4 (inset table).⁶² The stability of $\text{g-C}_3\text{N}_4$ after catalysis can be estimated by the % of different types of N so that the breakage of linkages, chain fragmentation, and different structural changes can be predicted. CO_2 adsorption and its activation highly depend on the type of N-moieties present (pyridinic, pyrrolic/pyridonic, and graphitic nitrogen). Pyridinic and pyrrolic/pyridonic nitrogen groups have lone pair electrons that exhibit Lewis basicity and, thereby, have the capability towards CO_2 adsorption and activation. Pyridinic nitrogen exhibits a higher affinity for CO_2 molecules than pyrrolic nitrogen owing to the higher basic strength of the former than the latter (Scheme 5).^{63,64}

Pyridinic-N with a higher negative charge in the 2-D plane retains a lone pair of electrons that can bind CO_2 more efficiently than other types of N moieties.^{65,66} Quaternary graphitic nitrogen exhibits Lewis acidity.^{67,68} Electrons are mostly present in the π^* -antibonding orbital in graphitic-N and thus are less accessible to CO_2 for binding.⁶⁵⁻⁶⁷ Pyridinic-N and graphitic-N can be easily presented in the melem units; however, other types of N-species are formed during un-controlled thermal polymerization in an oxygen lean environment leading to partial terminal uncondensed amines, N-oxide, and pyrrolic N species as shown in Scheme 5. The various N-species discussed above have the ability to impart tunable basicity, H-bonding, and Lewis acidity (frustrated Lewis acid-base pairs) and are thus suitable for various types of catalytic reactions involving CO_2 as a reactant.

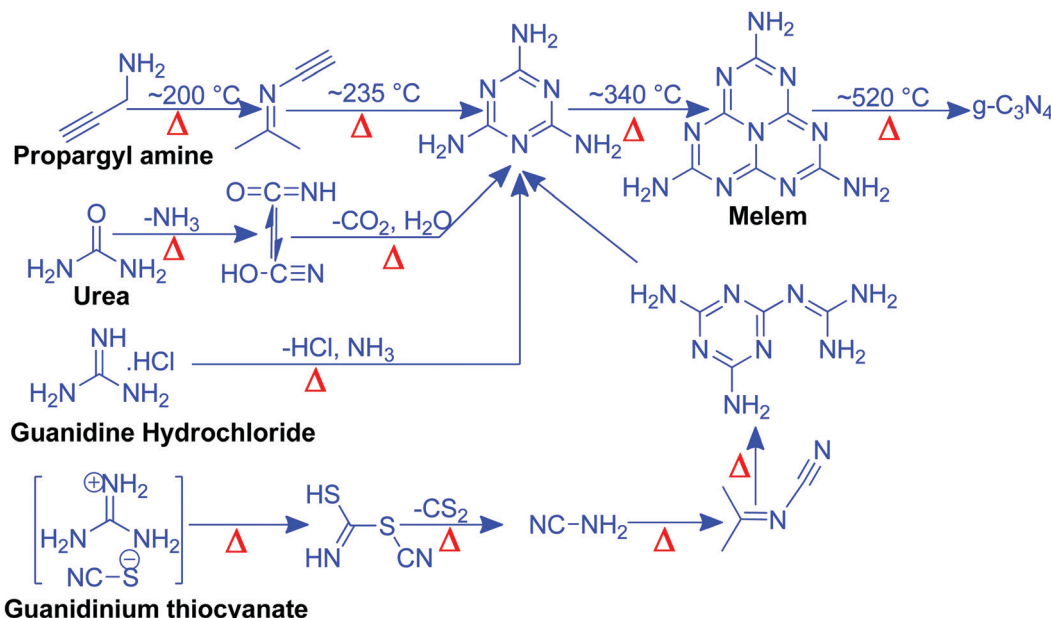
3. Synthesis strategies adopted for the preparation of carbon nitrides for improved CO_2 conversion

Based on the discussion so far we have understood that suitable micropores, high surface area, and pyridinic rich N sites are required for high CO_2 adsorption. CO_2 adsorption alone is not sufficient to catalyze various types of CO_2 based reactions because reactive partners also need to be efficiently adsorbed and suitably activated to synthesize various CO_2 derived chemicals. Further, bandgap and band edge positions can be finely tuned depending on the doping and crystallinity for light-induced CO_2 conversion. Thus, synthetic strategies, types of precursors, the temperature for synthesis along with the environment, and other parameters influence the physicochemical properties of $\text{g-C}_3\text{N}_4$. The following section describes the various synthesis strategies reported for the preparation of $\text{g-C}_3\text{N}_4$ for improved CO_2 activation.

3.1 Template free synthesis for improved catalysis and photocatalysis

Nitrogen-rich organic compounds such as melamine, cyanamide, and dicyandiamide are heated in semi-closed systems in oxygen-lean conditions to form $\text{g-C}_3\text{N}_4$ (Scheme 6). $\text{g-C}_3\text{N}_4$ is formed by various condensation steps in which the first melamine is formed at lower temperatures (< 350 °C) followed by removal of NH_3 leading to tris-s-triazine at a temperature around 400 °C. The polymerization of tris-s-triazine takes place at around 520 °C to form $\text{g-C}_3\text{N}_4$ (Scheme 6).⁶⁹ TGA investigation reveals that this framework is stable up to 550 °C. Even oxygen-containing precursors such as urea also follow the same sequence and form $\text{g-C}_3\text{N}_4$ via a melamine intermediate (Scheme 6). The nitrogen content and surface area of $\text{g-C}_3\text{N}_4$ depend upon the precursor and the pyrolysis temperature. With the increase in the pyrolysis temperature, the C/N ratio increases whereas the bandgap decreases.⁷⁰ During the polymerization process, the amine groups of tris-s-triazine don't condense completely, which results in the formation of uncondensed amine group-containing $\text{g-C}_3\text{N}_4$ with about 2% H content with a C/N ratio less than 0.75. Such a structural defect is important for the adsorption of reactant molecules, which is good for catalytic reactions.⁷¹ It may be noted that if the uncondensed groups (discussed above) are present in higher numbers then it might be good for conventional catalysis but is definitely not suitable for photocatalysis due to the less efficient charge transportation and separation of charge carriers. High-temperature polymerization leads to the formation of crystalline $\text{g-C}_3\text{N}_4$, which is better for charge carrier separation and a higher degree of π -conjugation and thus good for photocatalysis.⁷² Moreover, with the increase in the pyrolysis temperature, aggregated bulk $\text{g-C}_3\text{N}_4$ changes to a nanosheet and nanoflake like morphology with improved surface area.^{73,74} Also, urea and thiourea derived $\text{g-C}_3\text{N}_4$ exhibit better surface area due to the removal of CO_2 at higher temperatures, leading to high porosity and improved surface area when compared to the cyanamide precursor.





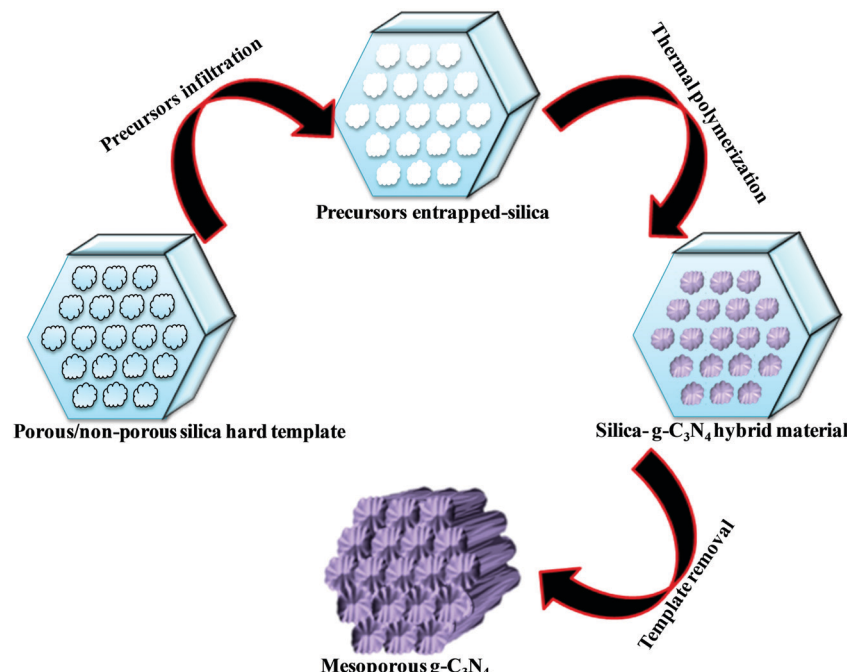
Scheme 6 Synthesis of $\text{g-C}_3\text{N}_4$ via the melem unit using different precursors.

Further, the surface area of urea derived $\text{g-C}_3\text{N}_4$ is improved if the pyrolysis is carried out for a longer time.⁷⁴ During such prolonged heating the layered structure of $\text{g-C}_3\text{N}_4$ is exfoliated and splitting takes place to produce low yield $\text{g-C}_3\text{N}_4$ with better surface area and photocatalytic activity.⁷⁵ Inspired by the synthetic paradigm of $\text{g-C}_3\text{N}_4$ from urea which has resulted in higher surface area due to the liberation of CO_2 during urea pyrolysis, sucrose and melamine have been pyrolyzed together. The reason for selecting sucrose is that it will generate a large amount of CO_2 during pyrolysis and produce $\text{g-C}_3\text{N}_4$ with N-deficiency and improved surface area (6 fold higher) and porosity.⁷⁶ The type of N species and surface area can be tailored by selecting different precursors. For example, guanidine hydrochloride or guanidine thiocyanate pyrolysis results in $\text{g-C}_3\text{N}_4$ via a melem intermediate and produced materials with high surface area and enhanced photocatalytic activity (Scheme 6).⁷⁷ The bandgap of $\text{g-C}_3\text{N}_4$ can be reduced and mid-gap creation is possible if a nitrogen-vacancy is created in the material. Nitrogen deficiency in $\text{g-C}_3\text{N}_4$ leaves additional electrons and creates nitrogen-vacancy related C^{3+} states leading to a reduced bandgap material. This can be easily achieved by heating the material in an H_2 atmosphere. H_2 , being a small molecule, can easily penetrate and diffuse to the interior lattice sites and reduce the lattice N sites and liberate NH_3 and create an N vacancy. In this process, the terminal N sites are more prone to reduction due to the lowest change in the energy of the molecule. Such an N vacancy in the system reduces the bandgap by downshifting of the CB and up-shifting of the VB position. Another situation can also arise in which new C and N sites are generated, which increases the H contents in the material and alters the bandgap of the material. Experimental analysis suggests that a three coordinated N-vacancy and H-substitution at the N sites decrease the bandgap by 0.2 and 0.55 eV.⁷⁸ This lowering in the bandgap is due to the formation

of additional band states below the CB by the defect C sites leading to lowering the bandgap values. The N-vacancy moves the VB energy to more negative values and H-substitution lowers the CB to more positive values and improves the visible light absorption capacity. The surface area of $\text{g-C}_3\text{N}_4$ can be improved by exfoliating bulk $\text{g-C}_3\text{N}_4$ in different solvent media such as water, ethanol, acetone, IPA, and NMP. Among these solvents, NMP has been found to be the best choice.⁷⁹ However, it is difficult to remove NMP from the exfoliated $\text{g-C}_3\text{N}_4$. Thus IPA has been explored as the next most desirable solvent to exfoliate bulk $\text{g-C}_3\text{N}_4$, so as to produce high surface area $\text{g-C}_3\text{N}_4$ of the order of $300\text{--}400 \text{ m}^2 \text{ g}^{-1}$. For exfoliation of bulk $\text{g-C}_3\text{N}_4$, aqueous alkaline and acidic solutions have also been explored with the aim of obtaining higher surface area.^{80,81} Although an improvement in the surface area is observed by varying the precursors, reaction temperatures, and pyrolysis environment, however, the materials still remain nonporous in nature. In order to introduce porosity in the material, template-assisted synthetic strategies have also been adopted as discussed below.

3.2 Template-mediated synthesis strategy to produce $\text{g-C}_3\text{N}_4$ with high surface area and porosity for improved CO_2 adsorption

Various hard template-mediated synthetic strategies utilize silica-based mesoporous materials (SBA-15, SBA-16, KIT-6, MCM-41, and MCM-48) as the template (Scheme 7). Nitrogen-containing organic precursors or carbon and nitrogen precursors are infiltrated into the porous architecture of silica materials via the incipient wet impregnation or wet impregnation method followed by pyrolysis, which results in the formation of $\text{g-C}_3\text{N}_4$ /silica hybrid materials. Finally, the silica template is removed by chemical etching using various etching agents, for example, NaOH , HF , and NH_4HF_2 . The final material has the same architecture as that of the original silica material.⁸²



Scheme 7 Hard template mediated synthesis of mesoporous $\text{g-C}_3\text{N}_4$.

Even silica nanoparticles have produced porous $\text{g-C}_3\text{N}_4$ with an average pore diameter of 12 nm, which is equivalent to the original silica nanoparticles.⁸³ In general, the pore diameter of the resulting material is smaller than the porous silica materials due to volume shrinkage of $\text{g-C}_3\text{N}_4$ filled inside the pores during the condensation.⁸⁴ The surface area and porosity significantly depend on the Si/precursor, hard template, and etching agent. The surface area can be further improved if the original silica material is treated with acid to enhance the surface reactivity, which allows a large number of organic precursors to in-filter, which improves the surface area of the resultant material.⁸⁵ This synthetic strategy produces a low yield of $\text{g-C}_3\text{N}_4$ and, therefore, is difficult for application in the large scale synthesis of mesoporous $\text{g-C}_3\text{N}_4$. Further, hazardous and costly HF and NH_4HF_2 limit its industrial-scale production.⁸⁶ To overcome this problem, CaCO_3 has been used as a hard template in which the template is removed with dilute HCl after polymerization, leading to the formation of high surface area $\text{g-C}_3\text{N}_4$ with improved photocatalytic activity.⁸⁷

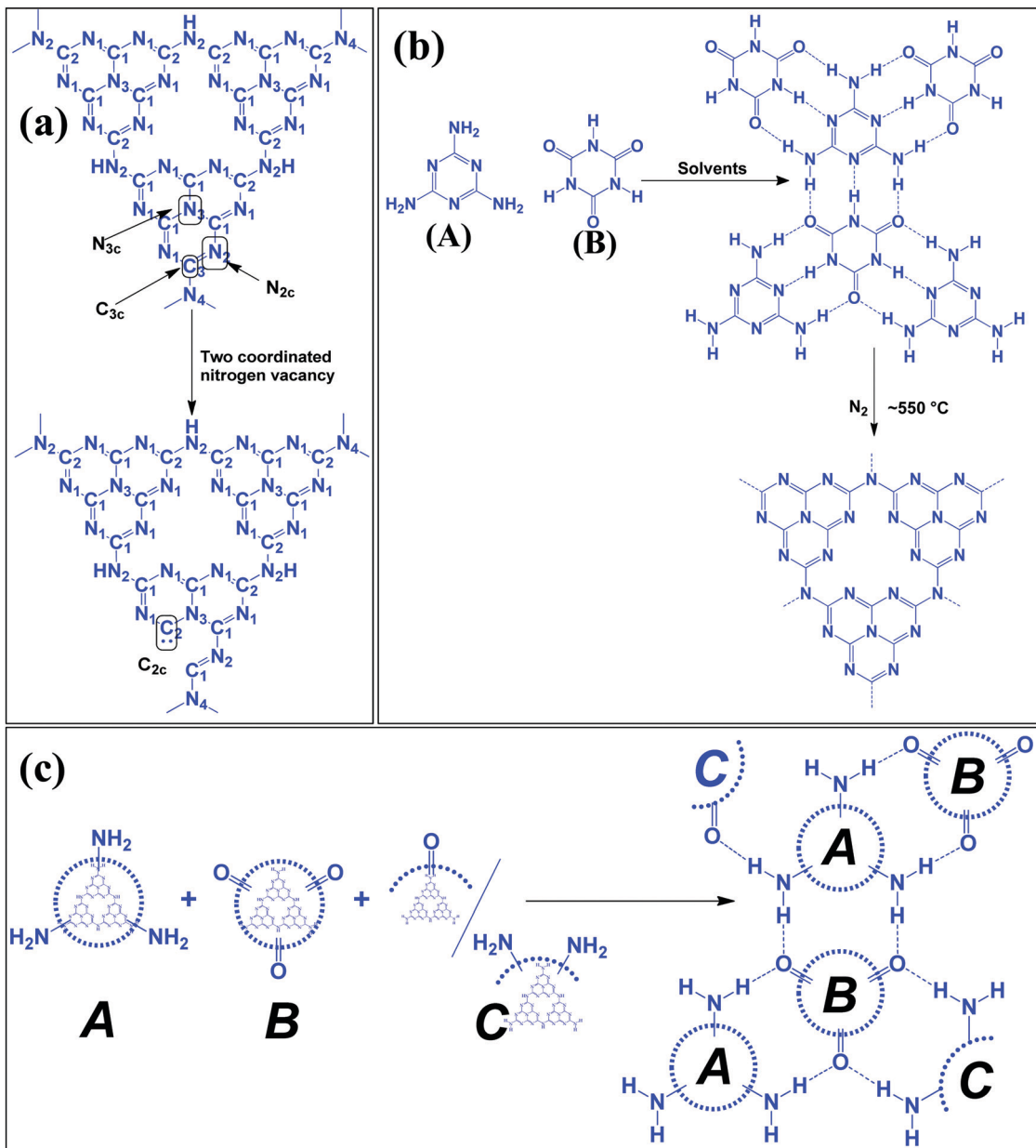
Large scale synthesis of mesoporous $\text{g-C}_3\text{N}_4$ can be achieved using the soft template method. Since the soft template is a carbon-based compound, therefore $\text{g-C}_3\text{N}_4$ with higher C/N is formed with diverse functionality. Ionic liquids and block copolymer-based soft templates have been widely used to prepare mesoporous $\text{g-C}_3\text{N}_4$. Among the soft templates, only a few templates such as Triton-100 and ionic liquids have produced $\text{g-C}_3\text{N}_4$ with large surface area and porosity.⁸⁷⁻⁸⁹ Ionic liquids act as soft modifiers for the thermal polymerization, leading to tunable textural properties, morphology, and reactivity. Anions of the ionic liquids participate in the growth process *via* C–N condensation.⁹⁰ Dual templating methods and cooperative assembly of two surfactants lead to formation of a

mesophase, which results in the formation of nanostructured materials. A similar strategy can be applied to synthesize mesoporous $\text{g-C}_3\text{N}_4$. Cooperative supramolecular assembly of surfactants, or a reactant and a surfactant, or reactants induced by hydrogen bonding and other weak electrostatic forces can act as a template to form mesoporous $\text{g-C}_3\text{N}_4$. Nitrogen-rich organic precursors can easily form hydrogen bonding with “O” containing organic compounds to form self-assembled porous $\text{g-C}_3\text{N}_4$. For example, melamine can form hydrogen bonding with cyanuric acid in DMSO and form stable aggregates that easily precipitate out (Scheme 8). Such precipitates can be thermally polymerized to form mesoporous $\text{g-C}_3\text{N}_4$.⁹¹ In fact, supramolecular aggregates can be formed by the hydrogen bonding between three reactants such as melamine, cyanuric acid with urea/barbituric acid/caffeine, *etc.* in a different solvent medium, which results in different morphology of mesoporous $\text{g-C}_3\text{N}_4$ on thermal polymerization with different textural properties and photophysical characteristics (Scheme 8).⁹²⁻⁹⁴ Template mediated synthesis strategies can provide materials with high surface area and porosity but it is difficult to tune the N contents and type of nitrogen due to the specific use of a suitable template and nitrogen precursor. Thus more work is needed to develop soft-template mediated synthesis recipes with variable N contents and functional amine sites using a diverse range of C and N containing precursors for the appointed applications.

3.3 Strategies to functionalize and dope elements to improve catalytic activities and light absorption properties

Template-mediated synthetic strategies can improve the surface area and porosity. However, for tuning the catalytic activities relating to the efficient adsorption of reactants and





Scheme 8 Supramolecular assembly of precursors leading to formation of mesoporous $\text{g-C}_3\text{N}_4$.

light absorption, suitable doping and functionalization are required. By varying the nitrogen precursors, the C/N ratio can be tailored, but for doping other elements such as O and S, suitable precursors containing O and S should be used during the synthesis of $\text{g-C}_3\text{N}_4$. Just by H_2O_2 treatment, O doped $\text{g-C}_3\text{N}_4$ with high surface area is obtained, which exhibits efficient charge carrier separation, and a red-shift in the absorption spectra.⁹⁵ An oxygen group containing melamine precursor also produces O doped $\text{g-C}_3\text{N}_4$.⁹⁶ Organic surfactant mediated synthesis produces C doped $\text{g-C}_3\text{N}_4$.⁹⁷ Diammonium hydrogen phosphate, hexachloro-cyclotriphosphazene, 2-aminoethylphosphonic acid, *etc.* have been used as a P source to dope P into the $\text{g-C}_3\text{N}_4$ framework.^{98–100} H_2S treatment, thiourea, and

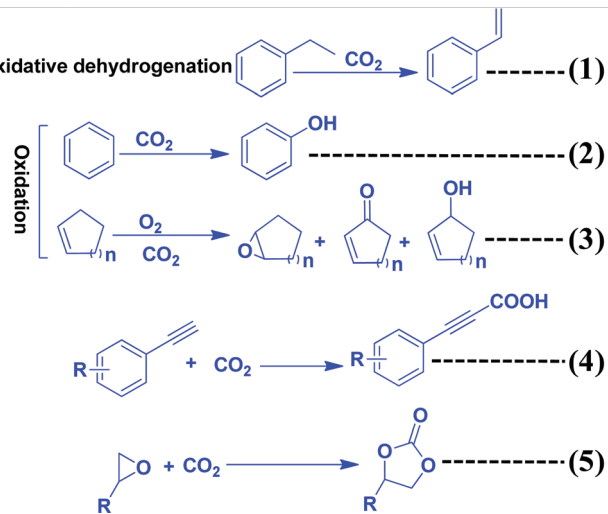
tri-thiocyanic acid precursors are known to dope S in the $\text{g-C}_3\text{N}_4$ framework.^{101–103} B-Doped $\text{g-C}_3\text{N}_4$ has been prepared by heating melamine and B_2O_3 above 520°C to introduce B into the $\text{g-C}_3\text{N}_4$ framework.¹⁰⁴ BH_3NH_3 and sodium-tetraphenyl boron have been used as precursors to prepare B-doped $\text{g-C}_3\text{N}_4$.^{105,106} Recently, it has been reported that exfoliation of $\text{g-C}_3\text{N}_4$ (prepared by urea and thiourea) with concentrated H_2SO_4 aqueous solution at 80°C has produced $-\text{SO}_3\text{H}$ functionalized $\text{g-C}_3\text{N}_4$.¹⁰⁷ Furthermore, it has been found that a small quantity of 2-methyl imidazole can be treated with urea-thiourea to produce O and C co-doped $\text{g-C}_3\text{N}_4$.¹⁰⁸ Thus, the choice of precursor and the treatment conditions can introduce desired elements and functionality in $\text{g-C}_3\text{N}_4$ to impart the desired catalytic activity.

4. Synthesis of chemicals and fuels from CO_2 using $\text{g-C}_3\text{N}_4$ as a catalyst in the conventional thermal catalytic process

Several recent review articles have been published, even using carbon nitrides as catalysts and photocatalysts.^{109–111} In this section, the role of CO_2 as a C_1 source to produce chemicals and fuels is described (Scheme 9). CO_2 can also act as an “O” source and can be utilized as an oxidant. CO_2 can be efficiently reduced to provide various chemicals and fuels. All these processes are non-atom efficient processes. CO_2 can be inserted in organic compounds like epoxides, amines, and alkynyl acids to produce organic carbonate and carbamate in a highly atom efficient process.

4.1 Role of CO_2 as a soft oxidant or promoter in the oxidation reaction

The oxidizing ability of various gases in coke oxidation follows the order: O_2 (105) > H_2O (3) > CO_2 (1), and thus CO_2 can act as a soft oxidant.¹¹² Such a weak oxidation ability is suitable in the oxidative dehydrogenation reaction. Oxidative dehydrogenation in the presence of oxygen leads to the generation of a large amount of CO_2 as a by-product due to the strong oxidizing ability of O_2 .¹¹³ CO_2 is a weaker oxidant and, therefore, it requires activation energy. In general, this activation can be achieved with alkali metals such as Li, K, Na, Ba, Ca, and Cs, which activate CO_2 to form MCO_2 .¹¹⁴ The activity of Li is higher among the above-mentioned metals due to the $\text{CO}_2\text{-M}$ valence bond angle, which is favorable for efficient CO_2 activation and utilization. In this dehydrogenation reaction, CO_2 facilitates the abstraction of hydrogen from hydrocarbons (alkanes, alkenes, alcohols, and alkyl aromatics) *via* catalytic activation to form CO and O species and suppress the total oxidation.¹¹⁵



Scheme 9 Synthesis of organic compounds using CO_2 as a reactant or oxidant or promoter and C_3N_4 as a catalyst.

$\text{g-C}_3\text{N}_4$ has been reported for the oxidation of benzene to phenol using CO_2 as a mild oxidant.¹¹⁶ CO_2 is activated *via* the secondary amine and pyridinic N of $\text{g-C}_3\text{N}_4$. Benzene is adsorbed weakly on $\text{g-C}_3\text{N}_4$. CO_2 splits into an O diradical, followed by its reaction with weakly adsorbing benzene to form the desired phenol as a product (Scheme 10). CO is eliminated after the reaction to regenerate the active sites for further CO_2 adsorption.¹¹⁶ CO_2 acts as a promoter in the cycloalkene oxidation using O_2 as an oxidant over a $\text{g-C}_3\text{N}_4$ catalyst (eqn (3), Scheme 9).¹¹⁷ CO_2 is efficiently adsorbed on $\text{g-C}_3\text{N}_4$ to form surface O species and produce CO (confirmed from the FT-IR study). Such surface O assists in the oxidation of cyclic olefins.¹¹⁶

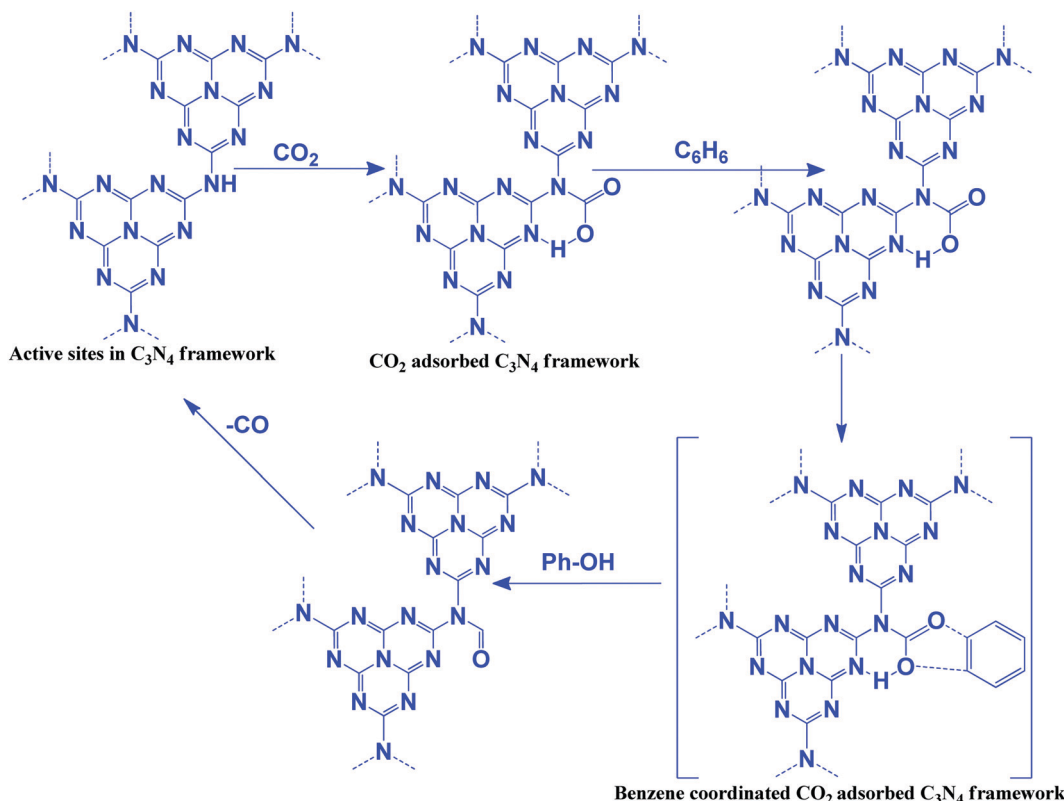
4.2 Carboxylation of terminal alkynes with CO_2

Alkynylcarboxylic acid is an important synthetic intermediate for several important compounds. For this reaction to proceed, both the alkyne and CO_2 need to be activated (Scheme 9, eqn (4)). CO_2 can be activated with $\text{g-C}_3\text{N}_4$ but for the efficient adsorption and activation of an alkyne, highly disperse active metals such as Cu or Ag are required. Ag NP decorated $\text{g-C}_3\text{N}_4$ has been reported for this reaction.¹¹⁸ This reaction follows the Langmuir–Hinshelwood mechanism in which CO_2 is absorbed and activated by $\text{g-C}_3\text{N}_4$ and the alkyne is adsorbed and activated by Ag NPs supported on $\text{g-C}_3\text{N}_4$. Alkyne acidic hydrogen is activated by the Ag NPs and forms silver acetylide and then this reactive intermediate reacts with activated CO_2 to produce silver carboxylate, which can be easily converted into cesium carboxylate with the help of Cs_2CO_3 *via* a transmetalation step. Finally, by workup with an acidified solution, it forms the desired alkynyl carboxylic acid.

4.3 Insertion of CO_2 into epoxides to form cyclic carbonates

The synthesis of cyclic carbonates by the reaction of CO_2 and epoxides is one of the most widely investigated reactions for CO_2 utilization because it is a 100% atom economic process. The cyclic carbonate product can be used as an intermediate for the production of value-added compounds such as Bisphenol-A carbonate (a synthetic polymer used in the packaging industry) and dimethyl carbonate (a methylating agent and a green solvent), the latter being a good fuel additive and a precursor for various other industrially important chemical transformations. CO_2 can be inserted in the epoxide ring *via* a non-concerted process to produce the cyclic carbonate. For this reaction, generally, a catalyst should contain a Lewis basic site, which acts as a nucleophile to activate the ‘C=O’ bond of the CO_2 molecule, while a Lewis acidic site acts as an electrophile for activating the epoxide ring.¹¹⁹ The Lewis acidic site polarizes the epoxide ring and forms an epoxide anion and then it acts as a nucleophile and attacks the CO_2 molecule, leading to the formation of a carbonate anion intermediate. The next step is either a ring-closing process for the formation of the cyclic carbonate or insertion of one or more epoxides and CO_2 molecules into the intermediate, which produces a polycarbonate.¹¹⁹ $\text{g-C}_3\text{N}_4$ has surface/edge located free $-\text{NH}_2$ groups which serve as Lewis basic sites and act as the





Scheme 10 Oxidation of benzene to phenol using CO_2 as an oxidant and $\text{g-C}_3\text{N}_4$ as a catalyst.

nucleophile to activate CO_2 . However, a Lewis acid site is absent to activate the epoxide. The weak activity of $\text{g-C}_3\text{N}_4$ towards this reaction is due to surface $-\text{OH}$ sites which have the ability to weakly activate the epoxide and produce a very low yield of the product. For this reaction to proceed efficiently, a co-catalyst such as tetra butyl ammonium bromide (TBAB) is used. However, suitable metal-free bi-functional $\text{g-C}_3\text{N}_4$ is reported to effectively catalyze this reaction.¹⁰⁷ Production of cyclic carbonates using different $\text{g-C}_3\text{N}_4$ based catalysts is summarized in Table 2. Conventional $\text{g-C}_3\text{N}_4$ exhibits very low activity (Table 2, entry 1).¹²⁰ Mesoporous $\text{g-C}_3\text{N}_4$ (prepared with different precursors) has exhibited better activity than conventional $\text{g-C}_3\text{N}_4$. Among the prepared materials, mesoporous $\text{g-C}_3\text{N}_4$ prepared with melamine exhibits 34% propylene oxide conversion, and 90% propylene carbonate selectivity with a TOF of 3.4 h^{-1} at moderate reaction conditions in DMF (Table 2, entries 2–4).¹²¹ A mixture of gas (50% O_2 and 50% CO_2) is used during this reaction and it has been proposed that O_2 plays a promotional role for the activation of the epoxide by supplying additional oxygen during the course of the reaction.¹²⁰ Further, to improve the surface area and dispersed active sites, SBA-15 supported $\text{g-C}_3\text{N}_4$ is employed for propylene carbonate synthesis under solvent-free conditions in the presence of doped metal ions, which act as Lewis acid sites. Among metal salts, Zn^{2+} exhibits the highest conversion and selectivity of 98.3% and >99%, respectively (Table 2, entries 5–8).¹²² The activity of doped Zn^{2+} is better than the supported ZnCl_2 catalyst (Table 2, entry 9).¹²³ It is proposed that the C_3N_4 nanosphere inside the mesopore

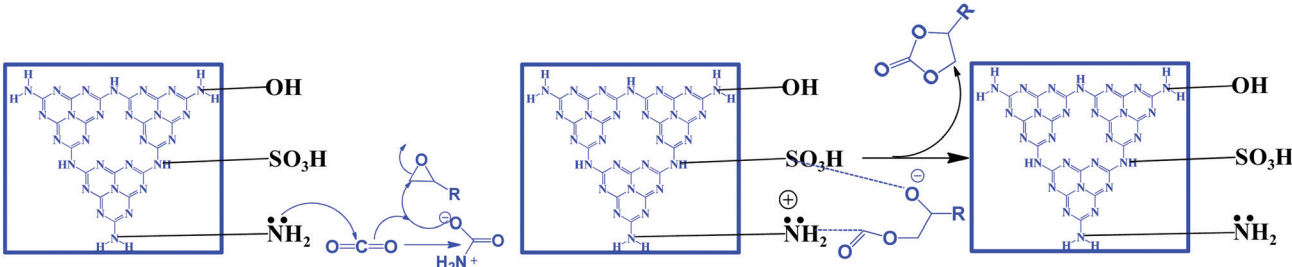
channel of silica supplies the activated CO_2 to the epoxide through a transfer mechanism and facilitates cyclic carbonate synthesis *via* Zn^{2+} activated epoxide species. Porous and amino rich $\text{g-C}_3\text{N}_4$ is prepared without using any hard template using urea as a precursor to form defective and edge enriched C_3N_4 . The urea derived C_3N_4 produces a wide variety of cyclic carbonates in the absence of any co-catalyst under solvent-free conditions (Table 2, entries 10–13).¹²⁴ It is suggested that the edge defects contain both primary amines ($-\text{NH}_2$) and secondary amine groups ($-\text{C}-\text{NH}-\text{C}$) and therefore they are able to activate CO_2 . The epoxide is activated by the defective C_3N_4 edge containing $-\text{OH}$ groups. Further, it has been revealed that urea derived C_3N_4 exhibits relatively higher surface area ($41 \text{ m}^2 \text{ g}^{-1}$) than dicyandiamide derived C_3N_4 and a porous nature, and the existence of macropores facilitates mass transfer and enhances the catalytic activity. *n*-Bromobutane grafted mesoporous $\text{g-C}_3\text{N}_4$ exhibits better catalytic activity for solvent-free propylene carbonate synthesis with 88% conversion and 98% selectivity (Table 2, entry 14).¹²⁵ In this process, the *in situ* depleted Br^- acts as the electrophile which activates the epoxide ring, while the defect rich edge positioned $-\text{NH}_2$ polarizes the CO_2 molecule leading to the bi-functional nature. Butane in conjugation with halides have been evaluated and it has been found that bromide exhibits the best activity because of its better leaving group ability. The better catalytic activity is attributed to the mesoporous nature (15 nm), high surface area ($241 \text{ m}^2 \text{ g}^{-1}$), and coexistence of terminal $-\text{NH}_2$ groups in $\text{g-C}_3\text{N}_4$ and X^- groups, which is even far better than the



Table 2 Comparative catalytic activity of various $g\text{-C}_3\text{N}_4$ based catalysts in the synthesis of cyclic carbonates

E. no.	Catalyst	S_{BET} ($\text{m}^2 \text{g}^{-1}$)	Co-catalyst	Reaction conditions	Conv. (%)	Select. (%)	TOF (h^{-1})	Ref.
1.	$g\text{-C}_3\text{N}_4$ (prepared with melamine)	64	—	ECH (5 mL), catalyst (50 mg), temp. (150 °C), press. (3.5 MPa), time (2 h)	5.6	96.7	3.3	120
2.	Mesoporous- C_3N_4 (prepared with melamine-2D mesoporous silica)	—	—	PO (1.5 mL), catalyst (20 mg), DMF (10), temp. (100 °C), press. (0.55 MPa), time (10 h)	34.0	90	—	121
3.	Mesoporous- C_3N_4 (prepared with urea-formaldehyde-2D mesoporous silica)	—	—	PO (1.5 mL), catalyst (20 mg), DMF (10), temp. (100 °C), press. (0.55 MPa), time (10 h)	28.0	92	—	121
4.	MS- C_3N_4 (prepared with melamine-glyoxal-2D mesoporous silica)	—	—	PO (1.5 mL), catalyst (20 mg), DMF (10), temp. (100 °C), press. (0.55 MPa), time (10 h)	25.0	98	—	121
5.	Mesoporous- C_3N_4 (prepared with dicyandiamide-SBA-15)	586	—	SO (3 mL), catalyst (100 mg), temp. (150 °C), press. (3.5 MPa), time (1.5 h)	28.8	99	4.8	122
6.	Mesoporous- C_3N_4 (prepared with dicyandiamide-SBA-15)	585	Zn^{2+} (0.8 wt%)	SO (3 mL), catalyst (100 mg), temp. (150 °C), press. (3.5 MPa), time (1.5 h)	94.5	99	15.8	122
7.	Mesoporous- C_3N_4 (prepared with dicyandiamide-SBA-15)	585	Zn^{2+} (0.8 wt%)	PO (3 mL), catalyst (100 mg), temp. (150 °C), press. (3.5 MPa), time (1.5 h)	97.1	99	16.2	122
8.	Mesoporous- C_3N_4 (prepared with dicyandiamide-SBA-15)	585	Zn^{2+} (0.8 wt%)	EO (3 mL), catalyst (100 mg), temp. (150 °C), press. (3.5 MPa), time (1.5 h)	98.3	99	16.4	122
9.	10% ZnCl_2 /mesoporous C_3N_4	206	Zn^{2+}	EO (7 mL), DMF (3 mL), catalyst (200 mg), temp. (140 °C), press. (2.5 MPa), time (6 h)	73.0	99.4	5.6	123
10.	$g\text{-C}_3\text{N}_4$ (prepared with urea and heated at 480 °C)	40.8	—	ECH (21.5 mmol), catalyst (100 mg), temp. (130 °C), press. (3.5 MPa), time (4 h)	99.6	96.4	—	124
11.	$g\text{-C}_3\text{N}_4$ (prepared with urea and heated at 480 °C)	40.8	—	EO (21.5 mmol), catalyst (100 mg), temp. (130 °C), press. (3.5 MPa), time (4 h)	91.7	99.3	—	124
12.	$g\text{-C}_3\text{N}_4$ (prepared with urea and heated at 480 °C)	40.8	—	SO (21.5 mmol), catalyst (100 mg), temp. (130 °C), press. (3.5 MPa), time (4 h)	98.0	99.8	—	124
13.	$g\text{-C}_3\text{N}_4$ (prepared with urea and heated at 480 °C)	40.8	—	PO (21.5 mmol), catalyst (100 mg), temp. (130 °C), press. (3.5 MPa), time (24 h)	99.3	99.6	—	124
14.	<i>n</i> -ButBr doped mesoporous C_3N_4 (prepared with cyanamide and 12 nm silica spheres)	248	Br^-	PO (10 mL), catalyst (200 mg), temp. (140 °C), press. (2.5 MPa), time (6 h)	88.0	99.7	9.6	125
15.	H_2SO_4 treated $g\text{-C}_3\text{N}_4$ (prepared with melamine)	32	—	ECH (5 mL), catalyst (50 mg), temp. (130 °C), press. (3.5 MPa), time (2 h)	99.1	99.5	58.1	120
16.	H_2SO_4 treated $g\text{-C}_3\text{N}_4$ (prepared with urea-thiourea)	10	—	ECH (63 mmol), catalyst (50 mg), Temp. (100 °C), press. (1.0 MPa), time (4 h)	93.5	99	—	107
17.	P-Doped $g\text{-C}_3\text{N}_4$ (prepared with melamine-hexachlorotriphosphazene)	—	Bu_4NBr	PO (28.6 mmol), catalyst (150 mg), Bu_4NBr (2.4 mol%), temp. (100 °C), press. (2.0 MPa), time (4 h)	99.8	99.9	—	126
18.	B-Doped $g\text{-C}_3\text{N}_4$ (prepared with melamine-BmimBF ₄)	11.1	—	ECH (14.3 mmol), catalyst (50 mg), temp. (130 °C), press. (2.8 MPa), time (6 h)	89.0	98.0	5.8	127
19.	B-Doped $g\text{-C}_3\text{N}_4$ (prepared with melamine-BmimBF ₄)	11.1	—	PO (14.3 mmol), catalyst (50 mg), temp. (130 °C), press. (2.8 MPa), time (6 h)	31.0	99.9	1.5	127
20.	B-Doped mesoporous $g\text{-C}_3\text{N}_4$ (prepared with dicyandiamide-B(OH) ₃ -SBA-15)	123	—	SO (1 mL), catalyst (30 mg), temp. (130 °C), press. (3.0 MPa), time (24 h)	97.8	96.8	—	129
21.	$g\text{-C}_3\text{N}_4$ (prepared with melamine)	—	Bu_4NBr	Light assisted method, ECH/SO (13.7 mmol), catalyst (50 mg), Bu_4NBr (1.8 mol%) temp. (105 °C), press. (1 atm, balloon), time (20 h)	100	100	—	130

ECH = epichlorohydrin, PO = propylene oxide, SO = styrene oxide, TOF = turnover frequency, conv. = epoxide conversion, selec. = cyclic carbonate selectivity, S_{BET} = surface area.



Scheme 11 Synthesis of cyclic carbonates using bi-functional $\text{g-C}_3\text{N}_4$, reproduced with permission, Copyright Royal Society of Chemistry, ref. 107.

externally induced *n*-bromobutane to carbon nitride during the course of the reaction (Table 1, entry 14).¹²⁵ Huang *et al.* have reported H_2SO_4 treated, protonated acidic functionality containing carbon nitride, which has been investigated for the solvent-free cycloaddition of CO_2 with epichlorohydrin for the synthesis of the corresponding carbonate (Table 2, entry 15).¹²⁶ This protonation process has altered the electronic and textural properties and surface chemistry, which results in the incorporation of hydroxyl groups and amine groups into the bulk urea derived carbon nitride, which provides 17 fold higher catalytic activity. Surface hydroxyl groups ($-\text{OH}$) and amine groups ($-\text{NH}_2$) are responsible for this improved reactivity. Inspired by this work, Samanta *et al.* have synthesized urea and thiourea derived carbon nitride CN-(UTU), which exhibits moderate catalytic activity better than the counterparts urea/thiourea under solvent-free cyclic carbonate synthesis from epichlorohydrin without any co-catalyst (Table 2, entry 16) (Scheme 11).¹⁰⁷ Further, to improve the catalytic activity, the resultant materials have been chemically exfoliated with H_2SO_4 , which results in the simultaneous incorporation of $-\text{SO}_3\text{H}$ and $-\text{NH}_2$ groups into the melem framework (Scheme 11).

The bi-functional catalyst (which is ideal for the CO_2 activation reaction) has been investigated in the CO_2 insertion reaction by varying the epoxide under very mild conditions (100 °C and 1 MPa). Excellent conversion and selectivity are achieved over this bi-functional CN-(UTU) catalyst. The simultaneous introduction of $-\text{NH}_2$ groups (that act as basic sites for activating CO_2) and $-\text{SO}_3\text{H}$ groups (that polarize the epoxide ring) has been confirmed from CO_2/NH_3 -TPD. The synergistic participation of $-\text{NH}_2$ and $-\text{SO}_3\text{H}$ groups during the reaction is the main reason for obtaining the excellent product yield. Moreover, doping with non-metals (such as P and B) over $\text{g-C}_3\text{N}_4$ is also reported for the synthesis of cyclic carbonates, which is found to be very effective for this reaction.^{126–129} The $-\text{B}(\text{OH})$ and $-\text{P}(\text{OH})$ groups are found to be responsible for the catalytic activity enhancement (Table 2, entries 19–20). All the reactions discussed above require CO_2 pressure higher than one atmosphere. Only one report is available in which a cyclic carbonate is synthesized at 1 atm pressure under solvent-free conditions but in the presence of external co-catalyst (1.8%) TBAB (Table 2, entry 22).¹³⁰ Therefore, more work should be carried out to synthesize efficient catalysts that can catalyze this reaction under solvent-free conditions at atmospheric pressure.

5. Photocatalytic CO_2 reduction reaction (CO_2 photoreduction)

Photocatalytic CO_2 reduction is a surface catalytic reaction which employs light-induced holes and electrons generated over the surface of the catalyst and protons from the reaction medium. In ideal conditions, CO_2 reduction follows some fundamental steps, like other light assisted reactions such as water splitting, N_2 reduction, and organic transformations.^{131–140} The basic operating steps involved in the photocatalytic CO_2 reduction reaction are summarized in two categories, namely optoelectronic and physicochemical steps, that are complementary to each other:

(A) Optoelectronic steps (Scheme 12A):

(1) Creation of charge carriers ($e^- - h^+$) on the semiconductor surface by illumination with light having energy greater than the bandgap: $E_{hv} \geq E_g$.

(2) Light-induced charge carrier dissociation and migration on the catalytic surface.

(3) Charge-carrier recombination followed by the dissipation of energy in the form of heat.

(4) The transported electrons participate in CO_2 reduction whereas holes participate in the oxidation of H_2O to O_2 , and H^+ or any other reducing agents to their corresponding oxidized products.

(B) Physicochemical steps (Scheme 12B):

(1) Adsorption of CO_2 on the catalyst surface.

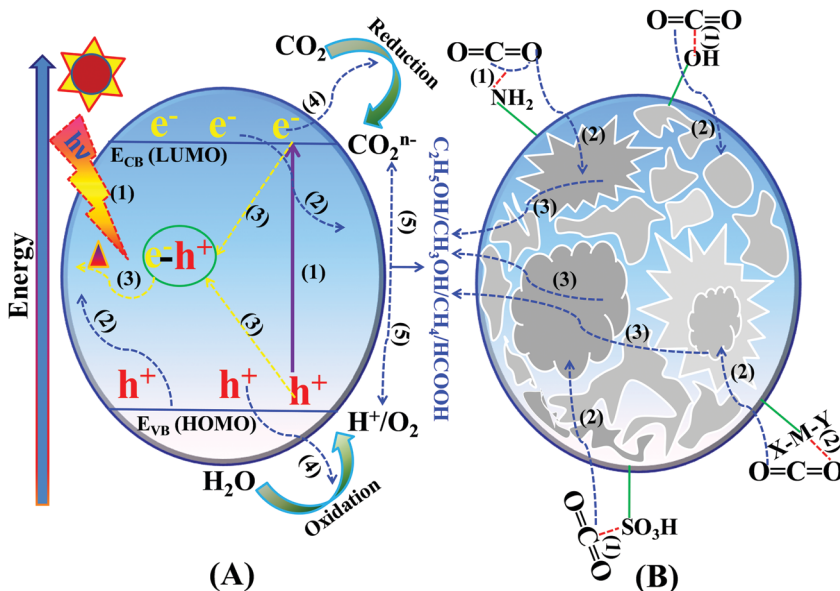
(2) CO_2 activation by the inherent functional groups of the catalyst.

(3) Intermediate species adsorption and desorption of the products from the catalytically active sites during the reduction reaction.

5.1 Factors and parameters governing the mechanism of CO_2 photoreduction

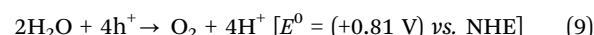
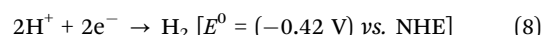
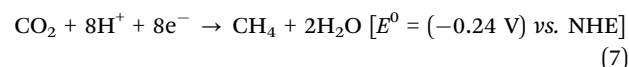
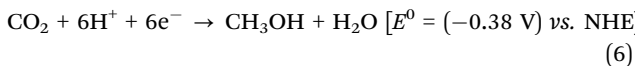
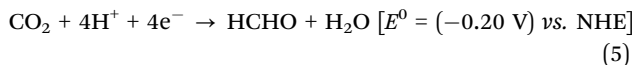
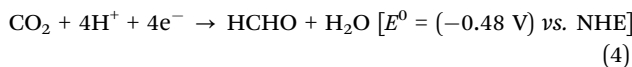
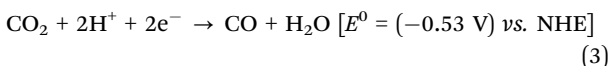
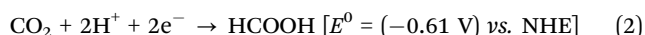
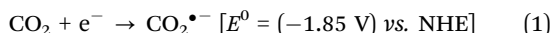
Carbon dioxide is the most stable and inert oxidized product, while methane is a completely reduced form of carbon (Scheme 13a). The light-induced conversion of CO_2 to hydrocarbons and oxygenated hydrocarbons depends on various factors and parameters. These factors determine the fate of the reaction as well as the CO_2 conversion and product distribution. Various factors influencing CO_2 reduction, especially with graphitic carbon nitride as a photocatalyst, are discussed in this section.

5.1.1 Thermodynamic factors. CO_2 conversion is a thermodynamically uphill energy process that requires a tremendous



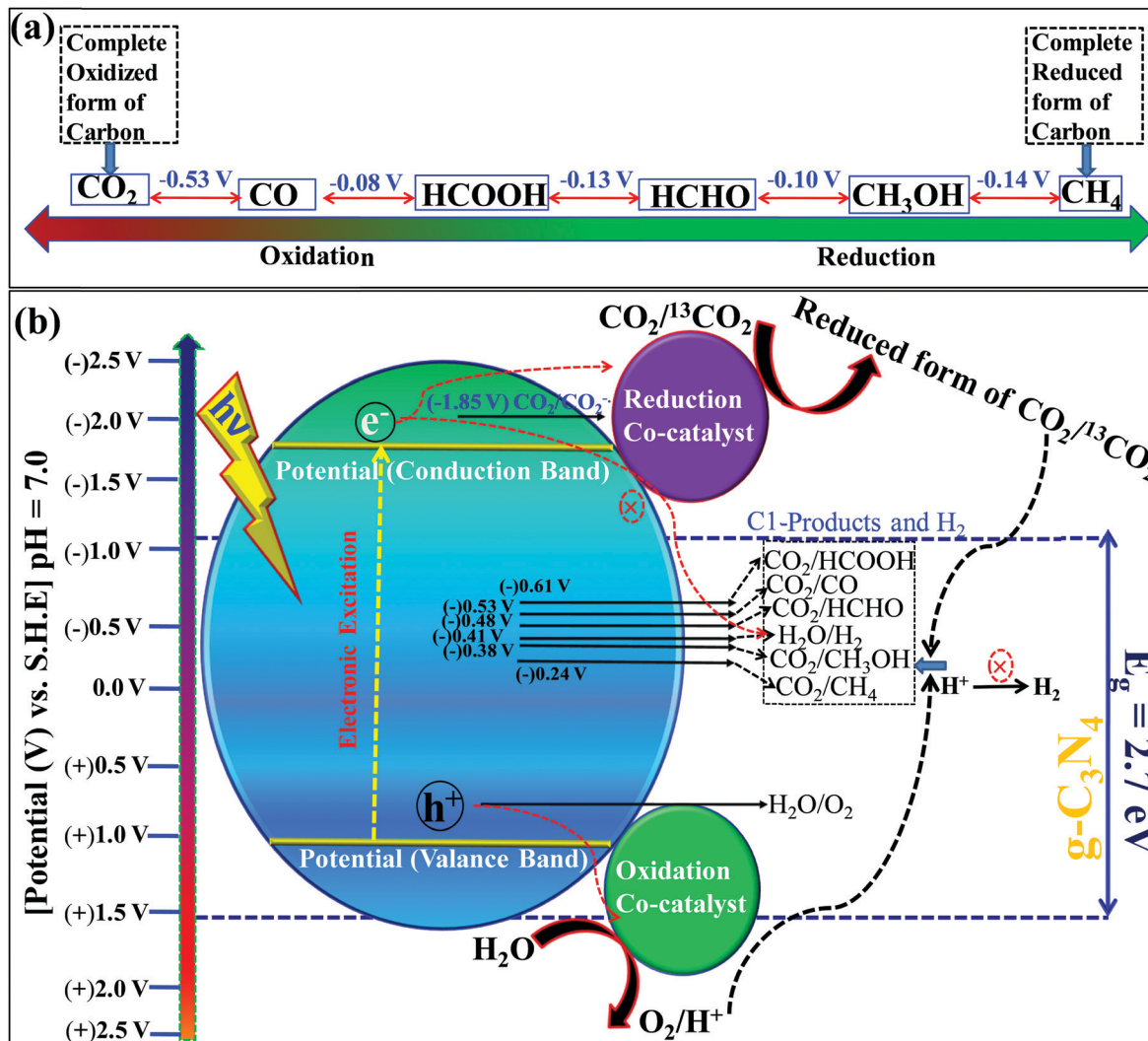
Scheme 12 Basic mechanism of the photocatalytic process: (A) optoelectronic steps and (B) physicochemical steps involved in the CO_2 reduction reaction.

energy input because of its stable and inert nature. An energy of 750 kJ mol^{-1} is required for the splitting of one ‘C=O’ bond in the CO_2 molecule. CO_2 has a low electron affinity and a high energy gap of 13.7 eV between its lowest unoccupied molecular orbital (LUMO) and highest occupied molecular orbital (HOMO).¹³⁷ CO_2 is a linear molecule and electronic accumulation in the empty LUMO (antibonding Π^* orbital) facilitates the transformation of a linear to a bent geometry over the catalyst surface, which in turn expedites the kinetic barrier and enables its smooth conversion to appropriate products. The band edge position of any photocatalyst decides this electron accumulation and, accordingly, the product distributions occur. Particularly, the valence band edge must be positioned at a more negative electrode potential than the standard reduction potential of CO_2 to any other products otherwise the process is not thermodynamically feasible (Scheme 13b). Based on the standard reduction potential,¹³⁸ the reduced products are given below, which must be considered to analyze the reaction products after the reaction to establish the plausible mechanism of the reaction (Scheme 13b).



Among these reactions, eqn (1) is the most unfavorable one and, thus, the proton-coupled electron transfer process always occurs on the catalyst surface with the production of different products.

5.1.2 Reaction mechanism and selectivity control. CO_2 reduction occurs sequentially involving multiple electrons and protons. Also, it requires the splitting of highly stable ‘C=O’ bonds and the creation of C-H bonds. The complete reduction occurs *via* the formation of several radical intermediates, which also tend to recombine at different stages during the course of a reaction.¹³⁹ The product distribution depends upon the specific set of reaction conditions. The simultaneous and competitive photo-oxidation and reduction reactions bring complexity to CO_2 photoreduction. The most important parameters influencing these reactions include the type of photocatalyst, band edge potentials and bandgap, reaction conditions and medium, co-catalyst, *etc.*, which are briefly described here. The first study reported for CO_2 photoreduction involves TiO_2 powder under photo-electrochemical conditions.¹⁴⁰ Based on the mechanistic investigation reported in the literature, three possible pathways have been proposed, (I) the formaldehyde pathway forming $\text{CO}_2 \rightarrow \text{CH}_4$ (fast hydrogenation pathway), (II) the carbene pathway forming $\text{CO}_2 \rightarrow \text{CH}_4$ (fast deoxygenation pathway), and (III) the glyoxal pathway (Scheme 14I-III).^{131,141} It may be noted that at some stage of the reaction, all the suggested



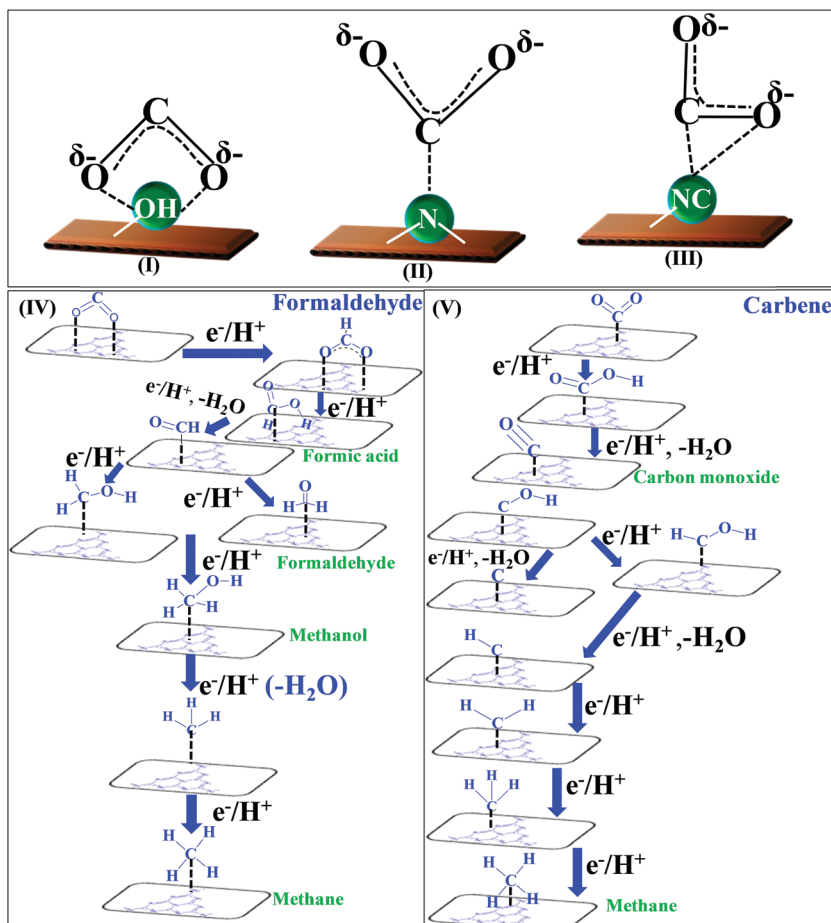
Scheme 13 (a) The different states of carbon with the potential difference, and (b) photocatalytic CO_2 reduction with respect to the standard redox potential of different products and band straddling.

pathways can equally dominate. The elementary steps based on the specific reaction conditions need more work to establish the possible involvement of several radical species. The above-mentioned pathways are specifically discussed here.

The conversion of CO_2 through the formaldehyde pathway involves multiple electrons and protons, which leads to the formation of several products such as HCHO , HCOOH and CH_3OH , and finally the deoxygenated product CH_4 . Starting from CO_2 involving $2\text{e}^-/2\text{H}^+$, it first produces HCOOH (oxy-hydrogenation), followed by involving $2\text{e}^-/2\text{H}^+$ again in the next step, which produces HCHO (reductive dehydrogenation).¹⁴² These two species formed during the reaction are intermediates and not side products. They can proceed to form unstable and reactive intermediates like $(^\bullet\text{CHO})/(^\bullet\text{COOH})$, which in the next step takes up $2\text{e}^-/2\text{H}^+$ to produce CH_3OH . CH_3OH can split to form $(^\bullet\text{CH}_3)$ and $(^\bullet\text{OH})$ radicals. $(^\bullet\text{CH}_3)$ can take one $(^\bullet\text{H})$ produced from the cleavage of HCHO to form CH_4 at the end. The formation of $\text{CH}_3\text{OH}/\text{HCHO}$ also depends on the adsorption and desorption energy over the catalyst surface. If the

coordination is strong enough and the desorption process is not facile, then $\text{CH}_3\text{OH}/\text{HCHO}$ will be the main product (Scheme 14(IV)). However, a weak binding energy allows this intermediate to produce the completely reduced CH_4 .¹⁴¹ Depending upon the intermediate binding energy, the yields and selectivity are regulated.

If the conversion process of $\text{CO}_2 \rightarrow \text{CH}_4/\text{CH}_3\text{OH}$ follows the carbene pathway, then several reactive intermediates can form *via* de-oxygenation followed by hydrogenation elementary steps. It can propagate like $\text{CO}_2 \rightarrow \text{CO} \rightarrow (^\bullet\text{C}) \rightarrow (^\bullet\text{CH}_3) \rightarrow \text{CH}_3\text{OH}/\text{CH}_4$. Thus this suggests the following: (1) CO_2 formation and radical formation of $(^\bullet\text{C})$ and $(^\bullet\text{CH}_3)$. (2) In the second step, the competitive reduction tendency between $(^\bullet\text{CH}_3)/(\bullet\text{C})$ and $(^\bullet\text{OH})/\text{H}$ often determines the product selectivity. In the first step, CO_2 is adsorbed on the catalyst surface through carbon co-ordination by the $1\text{e}^-/1\text{H}^+$ attachment to form the carboxyl radical $(^\bullet\text{COOH})$. After coupling with several e^-/H^+ , this can undergo decarboxylation to produce the formyl radical $(^\bullet\text{CHO})$. In the next step, it can break into $(^\bullet\text{C})$ and also can take three protons



Scheme 14 Co-ordination geometry of CO_2 over the catalyst surface (I–III), and plausible reaction mechanism of CO_2 reduction: formaldehyde pathway (IV), carbene pathway (V).

to produce the ($\cdot\text{CH}_3$) radical intermediate. In the final state, it couples with one H^+ or ($\cdot\text{OH}$) to form CH_3OH or CH_4 as the end product (Scheme 14(V)).¹⁴³ The adsorption strength of CO on the catalyst surface also influences the product selectivity. If the CO absorption is very strong then it could lead to the formation of several interim products and, consequently, desorption as different products. But if the absorption is weaker, then the easy desorption produces CO as an exclusive reduced product. In this process, the formation of radical species ($\cdot\text{CH}_3$) and ($\cdot\text{C}$) has been postulated and therefore electron paramagnetic resonance (EPR) measurements are very crucial to obtain a clear understanding of the reaction mechanism.

In the glyoxal mechanism, the first step is the formation of the one-electron reduction of ($\text{CO}_2\cdot^-$), which takes $1e^-/1\text{H}^+$ to form the formyl radical ($\cdot\text{CHO}$). This further undergoes dimerization to form the glyoxal product. The complete sequence of the elementary steps involves oxidation and reduction reactions as follows: $(\text{CO}_2 \rightarrow \text{CO}_2\cdot^-) \rightarrow (\cdot\text{CHO}) \rightarrow \text{CHO-CHO} \rightarrow \text{CH}_2\text{OH-CHO} \rightarrow (\cdot\text{CH}_2\text{-CHO}) \rightarrow \text{CHO-CH}_3 \rightarrow (\text{CH}_3\text{OC}\cdot) \rightarrow (\cdot\text{CH}_3) \rightarrow \text{CH}_4/\text{CH}_3\text{OH}$. However, this process is less explored and not completely understood yet.¹⁴⁴ Various C_2 products such as $\text{C}_2\text{H}_5\text{OH}$ or CH_3COOH etc. are believed to proceed through this pathway.

Based on the experimental observation and radical trapping/detection experiments, mechanistic routes are postulated, which requires further exploration. However, recent theoretical calculations suggest that defects and preferable coordination such as oxygen or carbon binding of the reactant, CO_2 , over the catalyst frequently determine the selectivity of the obtained product. A defect-less catalyst surface produces CH_4 only, while oxygen defect containing $\text{g-C}_3\text{N}_4$ catalysts simultaneously form $\text{CH}_3\text{OH}/\text{CH}_4$.^{145,146} This is an interesting observation and more detailed work is required.

5.1.3 Light-harvesting capacity and band straddling. Apparently, 40% is visible radiation within the spectral range of 0.4 to 0.7 μm , 51% is infrared radiation in the spectral region of 0.7 to 4 μm and 4% is UV radiation of the solar radiation received on the Earth's surface on a sunny day.¹⁴⁷ The total radiation energy emitted by the Sun in unit time remains practically constant. A blue shift of the light-harvesting domain also changes the thermal energy associated with the phonons. However, in a lab-scale reaction system, the most widely used 1.5 AM G light source provides energy equivalent to the energy of 1 Sun, which is 100 mW cm^{-2} .¹⁴⁸ The focus should be on developing materials that absorb in a wide area of the light spectrum and have a bandgap of 1.23 eV or higher so that the kinetic

energy to eject electron–hole pairs is sufficient to drive the catalytic reaction. A high light absorption coefficient is also a crucial factor for accelerating the electron-driven reduction reaction. More importantly, if a catalyst possesses a conduction edge position more negative than the standard one-electron reduction potential of CO_2 (eqn (1)), then it would be highly beneficial for this purpose.¹⁴⁹ Moreover, this particular conduction band edge position has been scarcely achieved so far. In standard conditions, the conduction band edge must be located at a more negative potential than the standard reduction potential of $E^0(\text{CO}_2/\text{HCOOH}) = -0.61 \text{ V vs. NHE}$, while the valence band edge position should be more positive than the water oxidation potential $E^0(\text{H}_2\text{O}/\text{O}_2) = +0.81 \text{ V vs. NHE}$.¹³¹ Additionally, the competitive H^+ reduction tendency must be suppressed to achieve better product yield. If the protons derived from water oxidation get reduced simultaneously then the proton coupled electron transfer to reduce CO_2 is also hampered. This will be discussed in the latter part. Thus, appropriate band straddling is one of the pivotal criteria in the light energy-driven CO_2 reduction reaction, similar to the thermal energy provided by heat. The standard electrode potential values for different CO_2 reduced products have very little energy difference (Scheme 13b). Therefore, the band edge potentials crucially determine the selectivity of a particular photocatalyst. A generalized tendency is to suppress the back reaction by lowering the valence band position so as to allow the holes to oxidize water molecules efficiently, which provides more electrons to the CO_2 molecules for their effective reduction. Another approach is to make the conduction band more negatively positioned so that competitive reduction could be minimized. Facile and faster hole–electron transfer sometimes appears to be a pivotal factor in the CO_2 photoreduction reaction. If the hole and electron mobility are getting affected, for example, trapping inside the defect sites over the photocatalyst's surface, then they may not reach the reactive sites. This ultimately affects the overall efficiency of the reduction reaction. In general, holes have slower mobility than electrons, which can be tailored by defect site engineering.¹⁵⁰ Accelerating the hole mobility may enhance the OER, which would provide more protons for CO_2 hydrogenation, and thus the selectivity can be controlled.

5.1.4 Promotional effects of H_2O oxidation. In common practice of CO_2 photoreduction, most of the time the OER is neglected and has been paid less attention. But from a fundamental point of view, it has an equal impact on CO_2 reduction.¹⁵¹ In ideal conditions, CO_2 behaves as the electron acceptor, while H_2O supplies the electron and proton to the surface-bound partially charged CO_2 . The water oxidation reaction consumes the light-induced holes and, thus, the photogenerated electrons become free to be used in the efficient reduction of CO_2 . Therefore, promoting H_2O oxidation reactions can tune the quenching of light-induced holes, minimizing the charge carrier recombination rate. Thus, sufficient numbers of photogenerated electrons would be made available in CO_2 reduction. Indeed, this promotional OER influences the product selectivity of CO_2 photoreduction.

5.1.5 CO_2 -Philicity. CO_2 adsorption on the photocatalyst surface is the very first and crucial step. Higher CO_2 philicity

would provide better catalytic activity. Adsorption is performed at two different temperatures to obtain the CO_2 binding energy of a particular photocatalyst. The higher CO_2 binding affinity implies its favorable reduction tendency. The adsorption interaction leads to the formation of a partially charged $\text{CO}_2^{\delta-}$ species with bent geometry having a lower LUMO level (Scheme 14(I)).¹³¹ Various modes of CO_2 adsorption geometry on the surface of photocatalysts are provided in Scheme 14(I)–(III), which are categorized into oxygen coordination, carbon coordination, and mixed coordination.¹⁵² $\text{g-C}_3\text{N}_4$ exhibits bidentate binding with oxygen coordination. Another absorption mode is carbon coordination, resulting in a carbonate-like radical species. When bi-functionality is present in $\text{g-C}_3\text{N}_4$, it favors mixed coordination. Different binding modes of $\text{CO}_2^{\delta-}$ often decide the reaction pathways. For example, the monodentate binding geometry by the C atom to the Lewis base centers (N atom of $-\text{NH}_2$ in $\text{g-C}_3\text{N}_4$) prefers the formation of the carboxyl radical ($^{\bullet}\text{COOH}$).¹⁴¹ On the other hand, bidentate coordination by two O atoms favors H-bonding to the carbon of $\text{CO}_2^{\delta-}$, leading to formate anion coordination in bidentate geometry over the catalyst surface. The formation of different interim intermediates greatly influences the reaction mechanism and thus tunes the product selectivity. In $\text{g-C}_3\text{N}_4$, surface functionalization with different CO_2 -philic molecules like amines, phosphates, sulfates, and hydroxyl groups greatly improves its CO_2 absorption capacity. Moreover, doping or intrinsic surface modification is another promising approach to improve the CO_2 -philicity of the $\text{g-C}_3\text{N}_4$ photocatalyst.

5.1.6 Effect of the reaction medium. CO_2 photoreduction can be carried out in two different reaction conditions, liquid phase suspension and solid–gas interaction.¹⁵³ In the suspension medium, the photocatalyst is dispersed in water medium. In the second one the photocatalyst is immobilized on a solid substrate and then water vapor is introduced through the reactor. In the first case, sometimes a CO_2 miscibility agent like acetonitrile or DMF is used, which is not an ideal reaction condition. The catalyst at the periphery of the reactor would get less light illumination and thus uniform light absorption may not be achieved. Moreover, the symmetrical photocatalyst particle distribution also depends upon mechanical stirring and those particles in the close vicinity of water molecules would contribute more to the resultant catalytic activity. The mixing of acetonitrile or DMF into water raises a question about the actual source of carbon during the CO_2 photoreduction reaction. So in ideal reaction conditions, a solid photocatalyst dispersed in CO_2 gas–pure water must be considered when performing this reaction to avoid any unwanted products. Besides, in the gas–solid medium, the gaseous CO_2 is allowed to react with the immobilized solid catalyst and H_2O vapor, which itself is in the gaseous phase. Considering the two states of H_2O and its ease of oxidation either in the liquid state or in the vapor phase, the activity and selectivity are greatly affected. Moreover, in this case, uniform light illumination is reached over the photocatalyst surface. Therefore, the total photons available in the solid–gas interaction are always more than in the case of the liquid-suspension medium. Additionally, the vapor phase of



H_2O is associated with extra thermal kinetic energy, which is eventually beneficial for overcoming the thermodynamic barriers. While in the first case oxygenated hydrocarbons like CH_3OH , HCOOH , *etc.* are preferably formed, in the second case complete hydrocarbons (CH_4) or oxy-carbons (CO) are achieved as products. Thus one should select different reaction media to obtain the desired product.

5.1.7 Impact of the CO_2 source. CO_2 can be directly inserted in the reaction medium from a gas cylinder or it can be *in situ* generated. The gaseous CO_2 is purged into water ($\text{pH} = 7$), which is a typical reaction condition of liquid-suspension medium as discussed in the previous section. It remains in a comparably less activated state than the *in situ* generated CO_2 from different sources.¹³⁹ Moreover, CO_2 can be *in situ* generated by the reaction between NaHCO_3 and H_2SO_4 or can be activated by employing NaOH . Sometimes elevated temperature and pressure are employed to make the interaction between CO_2 and the photocatalyst more kinetically favorable. This, in turn, favors HCO_3^- formation and also lowers the pH of the medium ($\text{pH} < 7$). Therefore, the CO_2 reduction follows the proton-coupled-electron-transfer (PCET) mechanism, leading to the formation of a wide range of products.¹⁵⁴ Ideally, employing additional thermal energy or *in situ* CO_2 generation inside the reactor is not a true photocatalytic reaction, but it is preferably used in the electrocatalytic process since NaHCO_3 itself acts as a CO_2 source as well as an electrolyte.

5.1.8 Influence of the reactor design. The reactor design and fabrication also significantly influence the CO_2 photoconversion efficiency. The major aim of designing a suitable photoreactor is to enhance the light-harvesting capacity uniformly, prohibiting the loss of photon energy, facilitating the ease of product separation, and allowing an appropriate interaction between the reactants and light energy with even distribution.¹⁵⁵ Basically, on the lab-scale, photoreactor systems can be classified into two categories: (1) a quartz glass reactor that allows light irradiation from the horizontal direction on the reaction system and (2) a moderately pressurized reactor containing a quartz glass window which can sustain a pressure up to 10 bar CO_2 and simultaneously allow light from the vertical direction. In the first case, both the liquid-suspension and the gas-solid system can be operated at atmospheric pressure where the CO_2 gas can be purged through a mass flow controller while H_2O vapor is inserted simultaneously. However, in the second case, only the liquid-suspension system can be operated where an external pressure and elevated temperature can be applied to activate the inert CO_2 gas. Since both the reactors involve a difference in their operating process, it is quite obvious that different efficiency and selectivity will be obtained in the two different reactors.¹⁵⁶ In the first case, light is passed through the reactor and therefore the catalyst encountering the light illumination on the front side will exhibit better activity than the backside one. However, in the gas-solid system, it will face the same light illumination with even intensity and so the obtained activity will be uniform. Therefore, the apparent quantum yield would be different depending upon the photoreactor since photocatalysis depends

on the area of illumination and not on the amount of catalyst. Similarly, in the second case, the catalyst at the bottom will get less light exposure and so its activity will be different from the catalyst placed at the top of the reactor. It is not possible to exactly propose the selectivity of the CO_2 photo-reduction products exactly based on the applied reactor. For example, the pressure sustaining reactor allows CO to stay inside the reactor, which may further undergo hydrogenation, leading to the formation of multiple products. On the contrary, in the continuous flow process, lower numbers of reduced products are achieved as it allows the reactant to spend less time inside the reactor.

5.1.9 Effect of sacrificial agents. Ideal CO_2 photoreduction uses water as the medium, where it acts as a sacrificial hole scavenging agent. But this fact totally depends upon the valence band edge position of the catalyst. If the valence band edge potential is more positive than the standard $E^0(\text{H}_2\text{O}/\text{O}_2)$, then it can exhibit sacrificial hole scavenging behavior. For the oxidation of one $\text{H}_2\text{O} \rightarrow \text{O}_2$, four holes are required and the produced O_2 can act as an oxidizing agent, which has an adverse impact on the CO_2 reduction reaction.^{141,153} But in several cases, additional sacrificial electron donors like triethanolamine (TEOA), *etc.* are used to facilitate the hole scavenging process, which makes the electrons free to reduce the CO_2 molecule. The hole induced oxidation of TEOA can also produce CO_2 and thus creates a disturbance in the operating reaction conditions. Therefore, the actual source of carbon in the reduced products is inevitably in doubt. Thus, a $^{13}\text{CO}_2$ isotope tracing experiment is also important in those cases where TEOA is used as a sacrificial electron donor. In some cases, H_2 gas is used as a proton and electron sources respectively. But it is imperative to state that a true CO_2 photoreduction reaction involves H_2O only as a sacrificial electron donor.

5.1.10 Effect of a co-catalyst. Noble metal-based co-catalysts such as Pt, Ag, and Au are widely used over a solid catalyst to add extra momentum to the overall thermodynamics of the CO_2 photoreduction reaction.^{157,158} This has a severe influence on both the performance and product selectivity of the CO_2 photoreduction process. It is well documented that when noble metals like Au, Pt, and Pd are decorated over a photocatalyst, a Schottky barrier is created at the junction. At this interface, the metal nanoparticles act as electron traps and prohibit the recombination of the photo-generated charge carriers. Additionally, plasmonic nanoparticles, specifically Au and Ag, facilitate photocatalysts to harness an extended range of visible light and enhance their photocatalytic performance. Also, the localized surface plasmon resonance induces the injection of hot electrons into the conduction band of the appointed photocatalyst and therefore electron accumulation enhances the CO_2 reduction tendency. These exciting features of noble metal co-catalysts are applicable to provide additional benefits in the CO_2 photocatalytic reaction. At the same time, they also enhance the competitive H_2 reduction tendency, which prohibits the CO_2 reduction reaction. But the overall bandgap, as well as the band edge positions, is altered, which provides opportunities to produce different CO_2 photo-reduction products



if it is the case of *ex situ* decoration of noble metals. Another distinctive point to be noted here is that the different affinity towards different interim species over different noble metal nanoparticles truly regulates the product distribution. Since noble metals are costly, their application as a co-catalyst is rather discouraging in ideal reaction conditions. But to obtain better activity and desired selectivity, one can employ such a co-catalyst.

5.1.11 Stoichiometric ratio of reaction consumed electrons and holes against the yield of the products. The stoichiometric involvement of electrons and holes in CO_2 reduction and H_2O oxidation is another important parameter because this will definitely influence the rate of formation of different products after the reaction. For example, the rate of total reactant conversion can be correlated with the rate of the different products formed and the numbers of electrons and holes consumed. For the reduction of 2 CO_2 molecules to produce 2 CH_3OH molecules, 12 electrons are required and, at the same instance, 12 holes must be consumed by the water molecules to produce 6 O_2 molecules. This is also a feasible thermodynamic concern in the CO_2 photo-reduction reaction, which can provide a meaningful idea about the photo-reduction and light-induced charge consumption during the reaction.

5.2 Graphitic carbon nitride as a CO_2 reduction photocatalyst

The basic phenomenon of CO_2 photo-reduction, especially with respect to heterogeneous catalysis, have already been addressed through several critical, tutorial, perspective, and edge articles by eminent researchers across the globe.^{159–165} Most importantly, CO_2 photoreduction over $\text{g-C}_3\text{N}_4$ has also been reviewed recently.^{153–165} Still, various aspects of this material and its further manipulation for CO_2 photoreduction catalytic efficiency improvement remain uncovered.

It is pertinent to mention that $\text{g-C}_3\text{N}_4$ has been continuously investigated in different photocatalytic applications since its application as a semiconductor HER photocatalyst by Wang *et al.* in 2009. However, among the seven different types of polymorphic phases (all are semiconductors), only the *g-h*-heptazine and *g-h*-triazine phases possess appropriate band-gaps and band straddling to catalyze various photocatalytic reactions. But, a close look at the valence band edge potential and theoretical calculations confirm that only *g-h*-heptazine fulfills the thermodynamic requirements for water oxidation.⁶² Notably, the *g-h*-heptazine based polymorphic $\text{g-C}_3\text{N}_4$ material has been most widely investigated as a photocatalyst with a bandgap of 2.7 eV where the conduction band is situated at (−1.2 V vs. NHE) and the valence band is positioned at (+1.5 V vs. NHE) at pH = 7. The CB and VB indicate that it is capable of reducing the CO_2 molecule and also can oxidize H_2O to produce O_2 and H^+ required for the production of hydrocarbons/oxygenated hydrocarbons in CO_2 photoreduction. Thus various nanostructured carbon nitrides with diverse morphologies such as nanosheets, microspheres, nanotubes, *etc.* are proven to be efficient catalysts for CO_2 photoreduction. Thermodynamic constraints and optoelectronic limitations are the main bottlenecks of this catalyst for CO_2 photoreduction as simultaneous CO_2 and H_2 reduction tendencies are observed for this particular catalyst.

Also, the rapid charge recombination and low active surface area are other shortcomings that significantly hamper the efficiency of this catalyst. Strategic improvement of the physico-chemical and optoelectronic properties is a pragmatic approach to overcome the poor CO_2 conversion efficiency of pristine $\text{g-C}_3\text{N}_4$. In the forthcoming sections, a concise summary of the recent literature reports dealing with CO_2 photoreduction efficiency improvement is compiled to give a clear understanding to researchers actively working in this area.

Dong *et al.* demonstrated, for the first time, CO_2 photoreduction involving porous carbon nitride (PCN) as a catalyst in 2012.¹⁶⁶ In this study, the authors propose that the porosity is introduced in bulk $\text{g-C}_3\text{N}_4$ by changing the precursors from melamine to melamine hydrochloride, which exhibits selective CO production of 4.5 mM in 11 h during CO_2 photoreduction. However, on the contrary, the activity of bulk $\text{g-C}_3\text{N}_4$ is shown to be better (20.6 mM in 11 h) than porous $\text{g-C}_3\text{N}_4$ and this is attributed to the presence of predominant inherent defect sites in PCN compared to bulk $\text{g-C}_3\text{N}_4$ that act as charge carrier recombination sites (Table 3, entry 1).¹⁶⁶ However, this adverse trend in the catalytic activity is unfortunately not fully understandable due to inadequate experimental evidence. Microstructure dependent CO_2 reduction activity has been reported by Mao *et al.* The authors have observed that urea derived, mesoporous, flake-like $\text{g-C}_3\text{N}_4$ has produced a mixture of oxygenated hydrocarbons ($\text{C}_2\text{H}_5\text{OH}$ and CH_3OH), while melamine derived, non-porous, flaky C_3N_4 has produced CO and CH_4 as products. The varied product selectivity is correlated to the reaction medium NaHCO_3 and CO_2 gas, where CO_2 is available in the activated form (HCO_3^-), which is more accessible to the catalyst. In this process, O_2 is obtained as a side product and it is established that the holes and electrons are consumed in a close ratio of ~1 during the reaction with an apparent quantum efficiency (A.Q.E.) of 0.18% at 420 nm (Table 3, entry 2).¹⁶⁷ The fine-tuning of the product selectivity is also reported in different studies, in which $\text{g-C}_3\text{N}_4$ nanosheets produce CH_4 as a selective product, while the bulk $\text{g-C}_3\text{N}_4$ produces CH_3CHO . This change in the product selectivity is proposed due to the switching of band edge potentials and also due to the different bandgap values. $\text{g-C}_3\text{N}_4$ nanosheets exhibit bandgap enlargement by 0.2 eV, which leads to a more positive valence band edge by 80 meV and a negative shift of the conduction band potential by 120 meV, which are the key reasons behind the different activity and selectivity as compared to bulk $\text{g-C}_3\text{N}_4$ (Table 3, entry 3).¹⁶⁸ Thermal polymerization of pre-synthesized urea derived C_3N_4 and red phosphorous (P) has formed a heterojunction and, with the aid of Pt as a co-catalyst, the optimized catalyst (PCN-30) has converted CO_2 to CH_4 with a rate of 295 $\mu\text{mol h}^{-1}\text{g}^{-1}$ in the suspension medium. The authors have proposed that the interfacial heterojunction has transferred the electrons from the high position $\text{g-C}_3\text{N}_4$ conduction band to a relatively lower position red P conduction band and the holes have been transferred in the reverse direction, which effectively reduces CO_2 to CH_4 and oxidizes OH to the (OH^\bullet) radical, respectively. However, the authors have not emphasized the exact role of Pt involved in the reaction as a co-catalyst.



Table 3 Photocatalytic CO_2 reduction reaction over $\text{g-C}_3\text{N}_4$ based photocatalysts

E. Catalyst/no. amount	$S_{\text{BET}} (\text{m}^2 \text{g}^{-1})$ /precursors and process	Co-catalyst	Reaction conditions		Products/rate	Time (h)	^{13}C isotope CO_2 tracing pressure Q.E.	Bandgap and band straddling	CO_2 adsorption	Ref.
			and (CO_2 source)	Light source						
1. $\text{g-C}_3\text{N}_4$ (100 mg)	—	None	CO_2 gas + H_2O	20.6 mM CO in 11 h 11	No	—	—	—	—	166
2. $\text{g-C}_3\text{N}_4$ (200 mg)	39.5	—	Supercritical fluid grade- CO_2 + NaOH solution	15.1 μmol CH_3OH + 12 10.8 μmol $\text{C}_2\text{H}_5\text{OH}$ +	—	—	0.18% At 420 \AA ($E_{\text{cb}} = -1.23 \text{ eV}$, $E_{\text{ob}} = \text{not defined}$)	2.78 eV	—	167
3. $\text{g-C}_3\text{N}_4$ nano-sheet (100 mg)	(306) dicyandiamide in thermal oxidation in air (Not provided)	—	CO_2 + H_2O	300 W Xe lamp	~0.12 μmol CH_4 and ~0.25 μmol CH_3CHO	5	No	0.06 MPa	—	168
4. Red P doped $\text{g-C}_3\text{N}_4$ PCN-30 (20 mg)	0.5 wt% Pt	CO_2 gas + H_2O	500 W Xe lamp	295 $\mu\text{mol h}^{-1} \text{g}^{-1}$	—	No	—	—	—	169
5. CN-12-1.5 (8 mg)	(240) (silica hard template/ cyanamide)	Ru co-catalyst	CO_2 gas + (H_2O + (3.9 $\mu\text{mol g}^{-1}$) TEOA) solution	400 W high-pressure Hg lamp	1854 nmol HCOOH	5	Yes	—	—	—
6. $\text{g-C}_3\text{N}_4$ nano-sheet CNU- $\text{BA}_{0.03}$ (30 mg)	(54) thermal polymerization of (urea and barbituric acid)	($\text{CoCl}_2 + 2,2'$ -CO ₂ + H ₂ O + (TEOA + cyanide) as electron donor)	—	—	—	—	—	E_g and E_{cb} not mentioned; $E_{\text{cb}} = (-1.29 \text{ V}) \text{ vs. Ag/AgCl at pH 6.6}$	—	170
7. S-Doped $\text{g-C}_3\text{N}_4$ (4.4) thermal poly-1 (TCN) (100 mg)	1 wt% Pt	($\text{CoCl}_2 + 2,2'$ -CO ₂ + H ₂ O + (TEOA + cyanide) as electron donor)	—	—	—	—	—	No data available Isotherm provided, binding energy did not mention	—	171
8. O-Doped $\text{g-C}_3\text{N}_4$ (36) melamine in tube (50 mg)	(36) melamine in two-step heating in air and N_2	$\text{NaHCO}_3 + \text{H}_2\text{SO}_4$	Not mentioned 2.6 μmol CH_3OH (420 nm)	3	No	1 atm	—	$E_g = 2.63 \text{ eV}$, no data available for band edge potentials	—	172
9. P-Doped $\text{g-C}_3\text{N}_4$ (13.4) melamine nanotube (50 mg)	—	$\text{NaHCO}_3 + \text{H}_2\text{SO}_4$	A high-pressure xenon lamp (300 W)	9.48 μmol CO and 7.24 μmol CH_4	4	No	1 atm	—	$E_g = 2.97 \text{ eV}$, $E_{\text{cb}} = -0.90 \text{ eV}$ vs. E_{NHE} at pH = 7, $E_{\text{ob}} = \text{not mentioned}$, $E_{\text{cb}} = -0.87 \text{ eV}$ vs. Ag/AgCl at pH = 7	174
10. Phenyl grafted $\text{g-C}_3\text{N}_4$ (100 mg)	(94.7) thermal polymerization of urea and phenyl urea at 550 °C for 2 h	DMF + TEOA + $\text{H}_2\text{O} + \text{CO}_2$	No information available 450 micromole $\text{CH}_3\text{OH} + 5 \mu\text{mol HCOOH}$	24	No	—	0.96% using $E_g = 2.97 \text{ eV}$, 20 W LED bulb	$E_{\text{cb}} = -1.01 \text{ eV}$, $E_{\text{ob}} = +1.65$	—	175
11. C ₆ O co-doped $\text{g-C}_3\text{N}_4$ (100 mg)	(56) thermal co-polymerization of (urea + thiourea + 2-methyl imidazole)	($\text{CO}_2 + \text{H}_2\text{O}$) + (TEOA Xenon lamp – acts as a sacrificial (300 W) electron donor)	4.18 mmol g^{-1} CH_3OH	6	No	1 atm	—	—	0.69 mmol g^{-1}	110

Table 3 (continued)

E. Catalyst/ no. amount	S_{BER} ($\text{m}^2 \text{g}^{-1}$) precursors and process	Co-catalyst	Reaction conditions and (CO_2 source)	Light source	Product/srate	Time (h)	^{13}C isotope CO_2 tracing pressure Q.E.	Band straddling and CO ₂ adsorption	Ref.	
12. mpg-CN _x (2 mg) and <i>in situ</i> synthesized cobalt phthalocyanine	(104) cyandiamide CoPPC	CO ₂ -Saturated (4:1) MeCN/TEOA	Xenon lamp, 100 mW cm ⁻² , AM 1.5G, $\lambda > 400$ nm	455 $\mu\text{mol g}^{-1}$ CO	24	Yes	—	(EQE) for CO: 0.11% vs. E_{NHE}^0 , $E_{\text{vb}} =$ at $\lambda_{\text{ex}} = 360$ and 400 nm	— 176	
13. DCN-0.05 (not mentioned)	(29.5) one step thermal polymerization of cyandiamide and tartaric acid	Bi-pyridine + CoCl ₂	CO ₂ gas saturated in 5 mL solution (4 mL ACN + 1 mL of TEOA) containing aq. bipyridine (10 mmol L ⁻¹ + 25 mL of 20 mmol L ⁻¹ CoCl ₂)	CO ₂ gas saturated in 300 W xenon 5 mL solution (4 mL ACN + 1 mL of TEOA + 10 mL H ₂ O)	284.7 $\mu\text{mol g}^{-1}$ CO and 51.6 $\mu\text{mol g}^{-1}$ H ₂	15	No	—	—	— 177
14. BA20-CNS-PDA15 (95) nanosphere (not mentioned)	(95) silica template Co(bpy) ₃ ²⁺ (150 mg 2,2'- bipyridine, +10 μmol CoCl ₂)	CO ₂ gas purged in 50 mL suspension (30 mL ACN + 10 mL TEOA + 10 mL H ₂ O)	300 W xenon lamp (420 nm cut off filter)	158 $\mu\text{mol CO} + 26$ $\mu\text{mol H}_2$ (86% selectivity)	4	No	—	—	$E_g = 2.63$ eV	
15. CN-ATZ-NaK (50 mg)	(15) (5-amino- tetrazole in a or NaCl/KCl eutectic mixture)	—	(0.084 g NaHCO ₃) + (0.3 mL 2 M H ₂ SO ₄) with an AM1.5 filter	350 W Xe lamp 14 $\mu\text{mol g}^{-1} \text{h}^{-1}$ CO Not mentioned $\text{CH}_4 + <1 \mu\text{mol g}^{-1}$ h ⁻¹ CH ₃ OH	—	No	—	—	$E_g = 2.53$ eV, $E_{\text{vb}} = (+1.87$ eV), $E_{\text{cb}} = (-0.66$ eV)	
16. O,C co-doped C ₃ N ₄ (MG ₃) (30 mg)	(10.8) (melamine + — glucose) water dispersion flowed by heating	CO ₂ gas purged in (ACN+ TEOA + H ₂ O) with a UV cut- off filter	300 W Xe lamp 55.2 $\mu\text{mol CO g}^{-1}$	12	No	—	—	$E_g = 2.66$ eV, $E_{\text{vb}} = (+1.38)$, $E_{\text{cb}} = (-1.28$ eV)	180	
17. Nitrogen defect- modified g-C ₃ N ₄ and NH ₄ Cl atomic layers: heating at different (CN ₅₅₀) (amount temperature not mentioned)	(103.1) (melamine — 1 μmol of cobalt chloride (CoCl ₂) ⁺ (15 mg of 2,2'- bipyridine)	Catalyst coated on a 500 W xenon graphite rod + H ₂ O + arc lamp assembled with a UV cut-off filter ($\lambda > 420$ nm)	>420 nm 9.28 $\mu\text{mol g}^{-1}$ CH ₄	8	No	—	0.089%	$E_g = 2.72$ eV, $E_{\text{vb}} = (+2.17)$, $E_{\text{cb}} = (-0.55$ eV)	181	
18. 1%B/g-C ₃ N ₄ (amount not mentioned)	(62.5) one-step calcination boric acid + urea	CO ₂ and H ₂ O vapor = (H ₂ SO ₄ solution + NaHCO ₃ powder) CO ₂ gas purged in 5 mL solution (1 mL TEOA + H ₂ O)	300 W Xe lamp 0.32 $\mu\text{mol g}^{-1}$ CH ₄ + 3 0.45 $\mu\text{mol g}^{-1}$ CO visible cut-off filter	—	Yes	—	—	Not provided	— 182	
19. CNU-TM-13.0 (30 mg)	(109.1) (urea + trimesic acid)	Co(bpy) ₃ ²⁺ , 1 μmol of cobalt chloride (CoCl ₂) ⁺ (15 mg of 2,2'- bipyridine)	CO ₂ gas purged in 5 Visible light ($\lambda > 420$ nm) and 14.99 $\mu\text{mol of}$ H ₂	70.63 $\mu\text{mol of CO}$ 4	Yes	1 bar	—	Not provided	Isotherm provided, binding energy did not mention 183	
20. B,K-Doped C ₃ N ₄ 5.3 (dicyandia- mide + KBH ₄) in H ₂ thermal etching (75) (urea + melamine + DI H ₂ O) hydrothermal treatment at 180 °C for 24 h	—	H ₂ O + CO ₂ gas	300 W Xe lamp 5.93 $\mu\text{mol g}^{-1}$ CH ₄ + 5 3.16 $\mu\text{mol g}^{-1}$ CO	—	No	2 bar	—	$E_g = 2.35$ eV, $E_{\text{vb}} = (+1.45)$, $E_{\text{cb}} = (-0.90$ eV)	— 184	
21. Tubular yolk- shell g-C ₃ N ₄ (100 mg)	—	supercritical fluid- grade CO ₂ gas + H ₂ O	300 W Xe lamp 40.3 $\mu\text{mol g}^{-1}$ CO	4	Yes	—	—	Isotherm provided, binding energy did not mention 185	Isotherm provided, binding energy did not mention for 24 h	



Table 3 (continued)

E. Catalyst/ no. amount	S _{BET} (m ² g ⁻¹) ^{1/2} precursors and process	Co-catalyst	Reaction conditions and (CO ₂ source)	Light source	Product/s rate	Time (h)	¹³ C isotope CO ₂ tracing pressure Q.E.	Band straddling	CO ₂ adsorption	Ref.
22. Nitrogen vacaney containing C ₃ N ₄ melamine in air followed by H ₂ atmosphere (CN-550)	(89.5) thermal combustion of C ₃ N ₄ melamine in air followed by H ₂	—	(High-purity CO ₂ gas + H ₂ O)	300 W xenon lamp equipped with a 420 nm cut-off filter	6.21 μmol h ⁻¹ CO	Not mentioned	No — —	E _g = 2.77 eV, E _{cb} = (+1.67), E _{cb} = (-1.07 eV) vs. NHE	—	146
23. Cyano and P-doped g-C ₃ N ₄ (g-C ₃ N ₄ -425) (100 mg)	(31.1) urea derived 1 wt% Au C ₃ N ₄ mixed with Na ₂ HPO ₄ followed by heat treatment (100 mg)	1 M 100 mL NaHCO ₃ + CO ₂ gas	300 W xenon lamp equipped with a 420 nm cut-off filter (λ = 420 nm)	1.135 μmol g ⁻¹ CO	3	Yes — —	E _g = 2.77 eV, E _{cb} = (+1.68), E _{cb} = (-0.54 eV) vs. NHE	—	186	
24. CNx _t (30 mg)	(29.4) (melamine + — HX) (X = Cl, Br, I) hydrothermal followed by carbonization in N ₂	CO ₂ gas purged in (ACN + TEOA + H ₂ O)	300 W xenon (λ = 420 nm) lamp with a UV-cut filter (λ = 420 nm)	34.14 CO μmol g ⁻¹ , 12 10.42 μmol g ⁻¹ H ₂ , 1.99 μmol g ⁻¹ CH ₄	No 80 kPa —	E _g = 2.83 eV, E _{cb} = (-1.13 eV) vs. NHE, E _{cb} not defined	—	—	—	187
25. Pyrene-functionalized polymeric carbon nitride (10% Py-PCN)10 mg	(2.11) cyanuric chloride (CC) + cyanamide (CA) + acetonitrile (ACN)	3 wt% Pt	Biphasic (1 mL 3 M 300 W xenon aqueous solution of lamp NaHCO ₃) (3 M) and 9 mL cyclohexene (or 9 mL toluene containing 2 mmol of 2-methyl-2-butene in toluene)	~0.7 μmol CO (using NaHCO ₃ ⁺ cyclohexane); ~0.15 μmol CO and ~0.23 μmol CH ₄ (using NaHCO ₃ + 2-methyl-2-butene in toluene)	4	No — —	E _g = 2.31 eV, E _{cb} = (+1.15), E _{cb} = (-1.16 eV) vs. NHE	—	—	188
26. g-C ₃ N ₄ (catalyst amount not mentioned)	(SA analysis not measured) thermal polymerization of melamine	H ₂ O vapour + CO ₂ gas	100 W xenon lamp	~20 ppm CO	5	No — —	E _g = 2.8 eV, band edge potential not mentioned	—	—	62
27. Se-Modified polymeric carbon nanonitride nano-sheets (m-CNNS) 0.08) 50 mg	(59.9) urea derived g-C ₃ N ₄ mixed in an ethanolic solution of Mg (NO ₃) ₂ 6H ₂ O followed by hydrothermal treatment	—	1 mL TEOA in 5 mL solvent (ACN; 3 mL; H ₂ O, 2 mL), 40 °C (λ > 420 nm)	~10 μmol CO, ~1.42 μmol H ₂	1	No 1 atm —	No information — available	—	—	189
28. Mg-Doped g-C ₃ N ₄ Mg/PCN-20% (50 mg)	(59.9) urea derived g-C ₃ N ₄ mixed in an ethanolic solution of Mg (NO ₃) ₂ 6H ₂ O followed by hydrothermal treatment	—	(100 mL H ₂ O + CO ₂ gas)	CH ₄ 17.09 μmol g ⁻¹ , 6 CO 4.13 μmol g ⁻¹	No — —	—	E _g = 2.54 eV, no information available about g-C ₃ N ₄	—	—	190
29. CN1/Pd nano-tetrahedron (NT) g-C ₃ N ₄ (50 mg of the catalyst was suspended in 6 mL of DI water Na ₂ PdCl ₄ in a glass reactor)	Urea derived g-C ₃ N ₄ followed by seed-mediated polyol-assisted reduction of Na ₂ PdCl ₄	Pd	(CO ₂ and H ₂ O vapor) 0.084 g of NaHCO ₃ + 0.3 mL of 2 M H ₂ SO ₄ solution	300 W Xe arc lamp	2.13 μmol h ⁻¹ g ⁻¹ CH ₄ production rate information of 0.58 μmol h ⁻¹ g ⁻¹ available	No — —	—	E _g = 2.75 eV	Theoretical CO ₂ adsorption energy (E _{ads} = -0.0083 eV) at the 100 surfaces of Pd NT	191



Table 3 (continued)

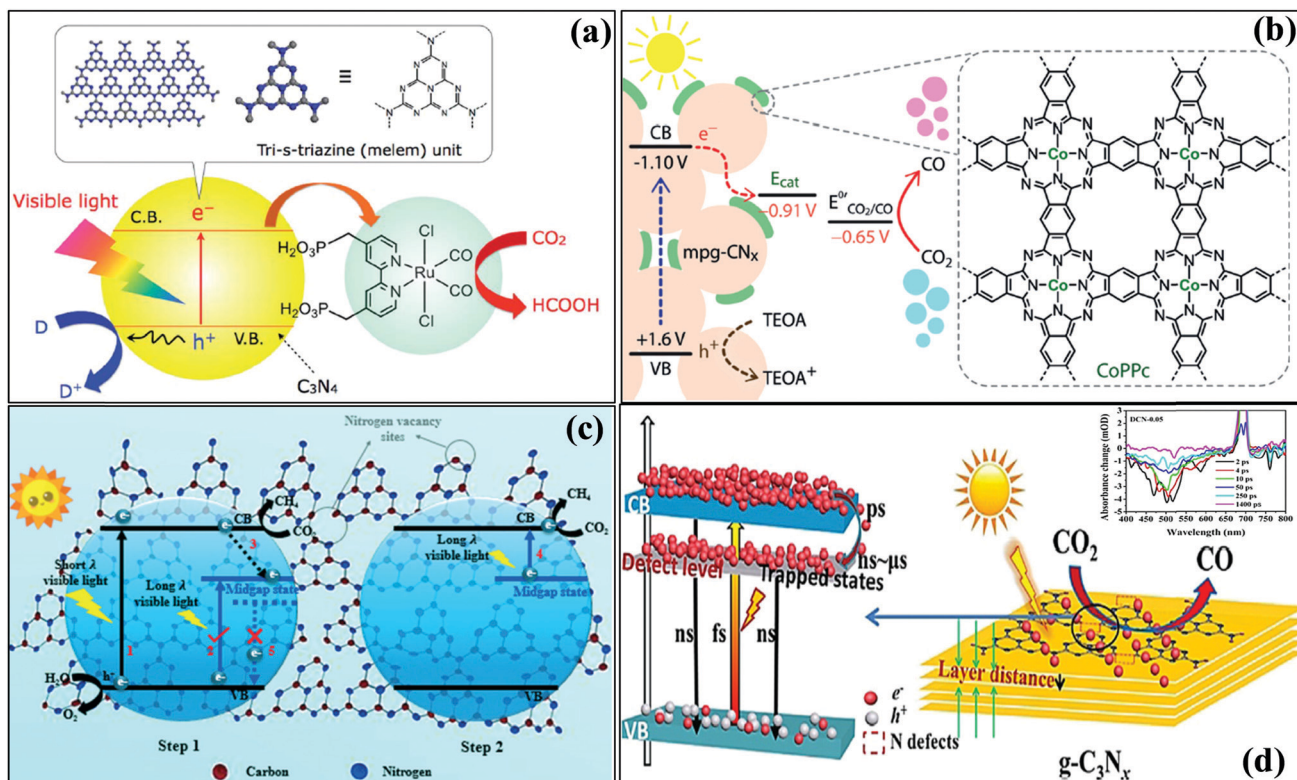
E. Catalyst/ no. amount	$S_{\text{BET}} (\text{m}^2 \text{ g}^{-1})$ / precursors and process	Co-catalyst	Reaction conditions and (CO_2 source)	Light source	Product/s rate	Time (h)	^{13}C isotope CO_2 tracing pressure Q.E.	Bandgap and band straddling	CO_2 adsorption	Ref.
30. Au/P-Doped $\text{g-C}_3\text{N}_4$ (200 mg of the sample was dispersed in 3 mL H_2O)	[Ionic liquid 1-butyl-3-methyl imidazoliumhexafluorophosphate (BmimPF_6) + dicyandiamide (DCDA)] thermal annealing followed by <i>in situ</i> photo-reduction of HAuCl_4	Au	($\text{H}_2\text{O} + \text{CO}_2$) gas	300 W xe-lamp	24 $\mu\text{mol CH}_4$	5	No —	$\text{CH}_4 \sim 2.83\%$, respectively at $\lambda = 420 \text{ nm}$	$E_g = 2.38 \text{ eV}$, $E_{\text{cb}} = (+1.4 \text{ eV})$, $E_{\text{cb}} = (-0.98 \text{ eV})$	192
31. Pt/g- C_3N_4	(The surface area was not mentioned) urea derived $\text{g-C}_3\text{N}_4$ followed by polyol-assisted reduction of H_2PtCl_6	2 wt% Pt	($\text{H}_2\text{O} + \text{CO}_2$) gas	15 W bulb, the average intensity at the reactor	13.02 $\mu\text{mol g}^{-1}$	10	No —	—	$E_g = 2.8 \text{ eV}$, No information available about E_{cb} and E_{bv}	193

(Table 3, entry 4).¹⁶⁹ K. Maeda *et al.* have synthesized high surface area mesoporous $\text{g-C}_3\text{N}_4$ using SiO_2 as a hard template and dicyanamide as a precursor by varying the silica/precursor ratio.¹⁷⁰ The dependency of the pore wall geometry on the CO_2 photoreduction activity has been uncovered in this study. Furthermore, the resulting mesoporous C_3N_4 has been grafted with a Ru complex *trans* (Cl)-[Ru{4,4'-($\text{CH}_2\text{PO}_3\text{H}_2$)₂,2'-bipyridine}(CO_2Cl_2)], where the electrons from the conduction band of $\text{g-C}_3\text{N}_4$ are transferred to the Ru and the bare holes in the valence band of $\text{g-C}_3\text{N}_4$ are engaged in the oxidation of water/triethanolamine, thus completing the total redox cycle (Scheme 15a).¹⁷⁰ The best catalyst of this study exhibits the selective formation of 1854 nmol HCOOH in 5 h by involving ($\text{H}_2\text{O} + \text{TEOA} + \text{CO}_2$) in the catalytic system under visible light illumination. The most fascinating outcome of this work is that high surface area is not always beneficial, rather the average surface area ($240 \text{ m}^2 \text{ g}^{-1}$) with higher pore volume ($0.74 \text{ cm}^3 \text{ g}^{-1}$) has minimized the charge carrier recombination and has shortened the electron-hole diffusion to the reactive sites (Table 3, entry 5).¹⁷⁰ J. Qin *et al.* have investigated the co-polymerization effect of monomer burbutyric acid with urea to synthesize $\text{g-C}_3\text{N}_4$, which eventually extends the pi-conjugated network, engineers the molecular hetero-interface and tailors the optical, surface area and nanostructural properties of $\text{g-C}_3\text{N}_4$ semiconductors for CO_2 reduction with the involvement of $\text{Co}(\text{bpy})_3^{2+}$ as a co-catalyst and acetonitrile containing triethanolamine solution as a sacrificial electron donor, and CO_2 gas.¹⁷¹ In this study, 56.3 μmol selective CO gas production is achieved in 4 h. ^{13}C isotope tracing measurements have confirmed that the CO_2 gas is the sole source of carbon, and, in fact, the control experiment has proved that all the components are essential for triggering CO_2 photoreduction (Table 3, entry 6).¹⁷¹ K. Wang *et al.* have reported S-doped $\text{g-C}_3\text{N}_4$ (TCN) which has been prepared *via* a simple heat combustion method and first-principles calculations suggest that some of the bi-dentate N atoms of the tris-triazine melem framework are replaced by sulfur during this process, having a narrow gap energy ($E_g = 2.63 \text{ eV}$) as compared to the melamine derived bulk $\text{g-C}_3\text{N}_4$ (2.7 eV). The CO_2 photoreduction result demonstrates the selective production of methanol with a yield of $1.25 \mu\text{mol g}^{-1}$ in 3 h from the ($\text{NaHCO}_3 + \text{HCl}$) induced ($\text{CO}_2 + \text{H}_2\text{O}$) vapor medium and Pt co-catalyst (Table 3, entry 7).¹⁷² J. Fu *et al.* have reported O-doped C_3N_4 nanotubes from controlled thermal oxidation etching which exhibit selective CH_3OH production with a yield of $2.6 \mu\text{mol}$ in 3 h from a ($\text{NaHCO}_3 + \text{H}_2\text{SO}_4$) mixture as CO_2 and proton sources, respectively. The oxygen doping causes a lowering of the conduction band by 0.16 eV by substituting the nitrogen atom of the melem unit, as evidenced by theoretical calculations, which is the prime reason for this selectivity control. Moreover, the higher CO_2 affinity and CO_2 uptake are also supported by CO_2 -TPD and CO_2 -adsorption analysis. The mechanism of methanol formation has also been confirmed by *in situ* FTIR and GC analysis (Table 3, entry 8).¹⁷³ B. Liu *et al.* have synthesized phosphorus-doped $\text{g-C}_3\text{N}_4$ nanotubes through a one-step thermal condensation between melamine and sodium hypophosphite monohydrate, which simultaneously dopes P and introduces surface amino groups. These modifications have led to higher

CO₂ uptake and favorable CO₂ adsorption, which have been experimentally confirmed by CO₂-uptake and zeta potential measurements. The resultant material has converted CO₂ to 9.48 μmol CO and 7.24 μmol CH₄ in 3 h. The experimental evidence suggests that phosphorus is interstitially doped into g-C₃N₄ during the synthesis, narrows the bandgap, exhibits a 1D nanotube morphology with high surface area, enhances the visible light absorption, and promotes the separation of charge carriers, which are the inclusive factors for this enhanced catalytic activity (Table 3, entry 9).¹⁷⁴ D. Vidyasagar *et al.* have synthesized a phenyl grafted g-C₃N₄ scaffold by reacting phenyl urea, melamine, and urea with enhanced pi-pi stacking, which lowers the bandgap and provides a favorable band edge potential for CO₂ photoconversion from (DMF + TEOA + H₂O + CO₂ gas) to produce CH₄, CH₃OH, and HCOOH with a yield of 0.907 μmol CH₄, 450 μmol CH₃OH, and 5 μmol HCOOH in 24 h using a 20 W LED bulb. The achieved apparent quantum yield is calculated to be 0.96% (Table 3, entry 10).¹⁷⁵ S. Samanta *et al.* have synthesized C, O co-doped C₃N₄ through a thermal poly-condensation of urea, thiourea, and 2-methyl imidazole as starting materials in an air atmosphere. The co-doping has increased the CO₂ uptake, gives a porous cotton-like morphology, lowers the conduction band edge potentials, and also red-shifts the light-harvesting domain. The material converts CO₂ gas saturated (TEOA + H₂O) solution to methanol with a yield of 4.18 mmol g⁻¹ in 6 h under visible light illumination. More importantly, theoretical calculations have provided favorable evidence about the high CO₂ binding energy after C, O co-doping, which is also supported by CO₂-TPD and CO₂-adsorption studies (Table 3, entry 11).¹⁰⁸ In interesting work, A. Roy *et al.* have synthesized a cobalt phthalocyanine (CoPPC) grafted polymeric graphitic carbon nitride photocatalyst in which the favorable CO₂ electro-reduction capability, as well as the light sensitization properties of cobalt phthalocyanine, has been emphasized. Combining the characteristic features of C₃N₄ and CoPPC enables the material to reduce CO₂ to CO in organic solvents (ACN + TEOA) under UV/vis light (AM 1.5 G, 100 mW cm⁻², $\lambda > 300$ nm) with a cobalt-based turnover number of 90 for CO after 60 h. More interestingly, in complete aqueous phase reaction conditions, the catalyst exhibits 60 μmol CO corresponding to a TON of 5.1 per CO. When the reaction condition is changed by keeping acetonitrile fixed and replacing TEOA with 10% H₂O the activity is reduced to 41%, indicating phase separation in aqueous medium (Table 3, entry 12).¹⁷⁸ CoPPC acts as an electron acceptor and lowers the conduction band edge potential of the overall system (Scheme 15b). A ¹³C isotope experiment fully agrees that CO₂ gas is the only source of CO in the reaction. The external quantum efficiency (E.Q.E) of CO is 0.11% and 0.03% at $\lambda_{\text{ex}} = 400$ and 360 nm, respectively (Table 3, entry 12).¹⁷⁸ Very recently, a 2D g-C₃N₄ nanosheet has been prepared *via* one-step tartaric acid-assisted thermal polymerization of dicyandiamide having nitrogen vacancies (g-C₃N₄) with preferential location at both three-coordinate N atoms and uncondensed terminal NH_x species. The material has produced 284.7 μmol g⁻¹ CO and 51.6 μmol g⁻¹ H₂ from the CO₂ gas dissolved in (TEOA + ACN) solution and Co(bpy)₃²⁺ as a co-catalyst in 15 h. The charge carrier migration and utilization

are demonstrated with transient absorption spectroscopy (Table 3, entry 13) (Scheme 15d).¹⁷⁹ M. Li *et al.* have synthesized polydopamine and barbituric acid co-modified carbon nitride nanospheres through thermal silica template-polymerization followed by a post-modification method, which has produced 158 μmol g⁻¹ CO and 28 μmol H₂ from CO₂ gas dissolved in aqueous (TEOA + ACN) solution and Co(bpy)₃²⁺ as a co-catalyst in 4 h using a 300 W xenon lamp (visible light). The co-modification tunes the band edge potentials and favors CO₂-adsorption, which are the key factors for the activity improvement (Table 3, entry 14).¹⁸⁰ J. Zhang *et al.* have synthesized grain boundary controlled carbon nitride using 5-amino tetrazole as a high nitrogen-containing organic compound and NaCl/KCl. The synthesized catalyst (CN-ATZ-NaK) exhibits 14 μmol g⁻¹ h⁻¹ CO, 1.2 μmol g⁻¹ h⁻¹ CH₄, and <1 μmol g⁻¹ h⁻¹ CH₃OH production rates from an activated CO₂ source (NaHCO₃) and H₂SO₄ as a proton donor. The grain boundary tailoring is the main reason for this impressive catalytic activity (Table 3, entry 15).¹⁸¹ Another carbon and oxygen co-doped g-C₃N₄ has been achieved by aqueous dispersion of glucose with melamine followed by thermal treatment. The resultant optimized material has produced 55.2 μmol CO g⁻¹ with nominal amounts of CH₄ and CH₃OH under visible light from CO₂ dissolved in a (TEOA + ACN + TEOA) reaction mixture in 12 h. Simultaneous co-doping has improved the visible light absorption and given fast electron extraction, which are responsible for this activity enhancement (Table 3, entry 16).¹⁸² Very recently J.-Y. Tiang *et al.* have synthesized nitrogen-vacancy enriched carbon nitride by two-step thermal copolymerization between NH₄Cl and melamine in a controlled environment, which induces mid-gap band state dangling between the conduction and valence band edge positions. The material has produced 9.28 μmol g⁻¹ CO in 8 h in the presence of a catalyst-coated graphite rod and (CO₂ + H₂O) vapors under visible light illumination. The main reasons underlying this enhanced CO₂ reduction activity are the introduction of dense nitrogen vacancies, extended light absorptivity of visible light leading to a wide range of light wavelength due to the strategic mid-gap arising, and prolonged lifetime of the charge carriers trapped inside the midgap. The obtained apparent quantum efficiency is calculated to be 0.089% (Table 3, entry 17) (Scheme 15c).¹⁸³ J. Fu *et al.* have reported boron as a dopant that induces charge localization inside the cavity of tris tri-azine by the interaction with the two co-ordinated -(N)₂ at the interstitial position. This claim is also justified by DFT calculations. The resulting 1%B/C₃N₄ has produced 0.32 μmol g⁻¹ CH₄ + 0.45 μmol g⁻¹ CO from (CO₂ + H₂O) vapor under visible light irradiation in 3 h. A ¹³C isotope tracing experiment has supported the CO intermediate end product CH₄ formation (Table 3, entry 18) (J. Fu *et al.*, 2019).¹⁸⁴ Trimesic acid-modified g-C₃N₄ (CNU-TMU-13) has been synthesized *via* a thermal combustion method which produces 70.63 μmol of CO and 14.99 μmol of H₂ in 5 h from aqueous TEOA saturated with CO₂ gas and Co(bpy)₃²⁺ as a co-catalyst. The origin of the carbon in the produced carbon is analyzed by a ¹³C isotope experiment and high CO₂ uptake is also in favor of the surface modification





Scheme 15 (a) CO₂ photoreduction over (a) Ru-complex g-C₃N₄, reprinted with permission, Copyright Royal Society of Chemistry, ref. 172; (b) Co(bpy)₃²⁺/g-C₃N₄, reprinted with permission, Copyright John Wiley and Sons, ref. 178; (c) N-vacancy containing g-C₃N₄ with a midgap state, reprinted with permission, Copyright Royal Society of Chemistry, ref. 183; and (d) defect and trap state containing g-C₃N₄, reprinted with permission, Copyright John Wiley and Sons, ref. 179.

by trimesic acid, leading to high catalytic activity (Table 3, entry 19).¹⁸⁵ Simultaneous B, K co-doped g-C₃N₄ has been synthesized using dicyandiamide and KBH₄ under an H₂ thermal etching process, which has accelerated the CO₂ reduction activity with the formation of 5.93 μmol g⁻¹ CH₄ and 3.16 μmol g⁻¹ CO from CO₂ dissolved in H₂O in the absence of any co-catalyst, electron donor, or CO₂ miscibility agent like DMF or acetonitrile in 5 h under visible light. This is also ascribed to the creation of nitrogen-vacancies and the incorporation of B and C together according to the reported theoretical simulation (Table 3, entry 20).¹⁸⁶ The morphology also has a great impact on photocatalytic CO₂ reduction. Tubular yolk-shell g-C₃N₄ has been hydrothermally synthesized from melamine and urea at 200 °C. The material has produced 40.3 μmol g⁻¹ CO in 4 h from super-critical grade CO₂ and H₂O. The formation of CO is also analyzed by a ¹³C isotopic experiment. This catalytic improvement is correlated to the higher CO₂ uptake as evident by the CO₂-uptake profile and also due to the obtained tubular morphology (Table 3, entry 21).¹⁸⁷ Another study reports the synthesis of nitrogen-vacancy containing C₃N₄ through the controlled polymerization of melamine in different atmospheres, which selectively produces 6.21 μmol h⁻¹ CO from the catalyst suspension medium of CO₂ and H₂O under visible light illumination (Table 3, entry 22).¹⁴⁶ The replacement of nitrogen has profoundly controlled selective CO production, which is established *via* DFT calculations

(Table 3, entry 22).¹⁴⁶ In a very strategic approach, X. Liu *et al.* have synthesized cyano-groups and phosphorus-doped C₃N₄ by treating pre-synthesized carbon nitride with NaH₂PO₂ under an argon atmosphere at different temperatures. The authors have proposed and proved that the thermal decomposition of NaH₂PO₂ produced PH₃ gas, which itself was doped as phosphorus and was also accountable for the conversion of the terminal, uncondensed =C-NH₂ to -CN groups during the synthesis process. In fact, the attachment of -CN groups served as electron-withdrawing groups over the carbon nitride surface, which benefited CO₂ activation. The phosphorus doping has enlarged the light absorption and has inhibited photogenerated charge recombination. The active material (g-C₃N₄-425) has converted NaHCO₃ saturated CO₂ gas to CO with a yield of ~1.14 μmol g⁻¹ in 3 h using 1 wt% Au as a co-catalyst under a 300 W xenon lamp (Table 3, entry 23).¹⁸⁸ S. Wan *et al.* have prepared hexagonal tubular carbon nitride by the heat treatment of the supra-molecular organization of the *in situ* hydrogen-bonded melamine cyanuric acid assembly under hydrothermal conditions. Hydrogen fluoride is found to be the best suitable haloic acid (H-X; X = F, Cl, Br, I) that promotes the dissolution of melamine, which eventually facilitated the pi-pi stacking as evidenced by the intense EPR spectra. The light absorption has been blue-shifted and charge separation is maximized with HF. The best active catalyst has produced 34.14 CO μmol g⁻¹, 10.42 μmol g⁻¹ H₂, and 1.99 μmol g⁻¹ CH₄ in 12 h under

visible light from 0.8 bar CO_2 gas pressure dissolved in a mixture solution of (acetonitrile + TEOA + H_2) (Table 3, entry 24).¹⁸⁹ The authors have also calculated the average electron consumption rate (R_{electron}) during the CO_2 reduction reaction as equal to $8.96 \text{ mol g}^{-1} \text{ h}^{-1}$ on the basis of the equation $R_E = (2R_{\text{H}_2}) + (2R_{\text{CO}}) + (8R_{\text{CH}_4})$, where R is the rate, expressed in $\mu\text{mol g}^{-1} \text{ h}^{-1}$ (Table 3, entry 24).¹⁸⁹ For the first time ever, the stability aspect of $\text{g-C}_3\text{N}_4$ in the CO_2 photoreduction reaction has been investigated in-depth by F. R. Poimilla *et al.*, in which the authors provide insights about the stability of the melem framework before and after catalytic activity evaluation (Table 3, entry 25).⁶² They have synthesized $\text{g-C}_3\text{N}_4$ by following a two-step thermal polymerization of melamine. For comparison purposes, they have also synthesized O-doped $\text{g-C}_3\text{N}_4$ by treating carbon nitride with H_2O_2 . They observed a marginal difference in the catalytic activity after repetitive cycles. In gas phase CO_2 reduction, the catalyst exhibits 20 ppm selective CO in 5 h under 100 W xenon light (Table 3, entry 25).⁶² But, surprisingly, CO is obtained even in the absence of CO_2 gas under light illumination, which raised the question about the origin of carbon from the graphitic carbon nitride photocatalyst. In association with detailed optoelectronic and physicochemical measurements and also with controlled analysis, the authors concluded that the photo-corrosion rather than the thermal decomposition of melamine is responsible for this unexpected behavior of the catalyst under their experimental conditions. In another breakthrough, X. Gong *et al.* have synthesized pyrene functionalized graphitic carbon nitride, which endows biphasic CO_2 reduction combining CO_2 reduction by the electrons in the aqueous phase and hole generated (OH) radical-induced olefin oxidation in the organic phase. The process of accessibility of the organic olefin into the aqueous system is facilitated by the increased lipophilicity of the grafted pyrene-functionality over $\text{g-C}_3\text{N}_4$. The authors have achieved $\sim 0.7 \mu\text{mol CO}$ from (NaHCO_3 + cyclohexane) and ($\sim 0.15 \mu\text{mol CO} + \sim 0.23 \mu\text{mol CH}_4$) from (NaHCO_3 + 2-methyl-2-butene in toluene) under 300 W xenon light illumination in 4 h (Table 3, entry 26).¹⁹⁰

Various noble and non-noble metal modified carbon nitrides also exhibited profound CO_2 reduction catalytic activity. H. Ou *et al.* have prepared selenium modified thin $\text{g-C}_3\text{N}_4$ porous nanosheets (m-CNNs_S) using pre-synthesized $\text{g-C}_3\text{N}_4$ in an ethanolic solution of diphenyl diselenide (DDS) followed by thermal polymerization. The evolution of $\sim 10 \mu\text{mol CO}$ and $\sim 1.42 \mu\text{mol H}_2$ is obtained over this catalyst from a reaction mixture containing (TEOA + acetonitrile + H_2O) at 40°C in 1 h using 420 nm light irradiation using $\text{Co}(\text{bpy})_3^{2+}$ as a co-catalyst (Table 3, entry 27).¹⁹¹ The role of selenium is investigated with density of state calculations, which evidences that selenium has narrowed the conduction band by creating an electronic distribution with the conduction band of CN. But it has not hampered the conduction and valence band composition as its Fermi level exists in the middle of the CB and VB level of $\text{g-C}_3\text{N}_4$. J. Tang *et al.* have synthesized Mg-doped $\text{g-C}_3\text{N}_4$ considering the high CO_2 philiicity of MgO and the light-harnessing capacity of the Mg^{2+} ions in natural chlorophyll. The synthesized material has produced $17.09 \mu\text{mol g}^{-1} \text{ CH}_4$ and $4.13 \mu\text{mol g}^{-1}$

CO from CO_2 gas saturated H_2O under a 300 W xenon lamp in 6 h (Table 3, entry 28).¹⁹² Though the light-harvesting capacity is enhanced, they did not emphasize the CO_2 uptake phenomenon with any experimental evidence. S. Cao *et al.* have prepared Pd nano-tetrahedron doped $\text{g-C}_3\text{N}_4$ from urea derived $\text{g-C}_3\text{N}_4$ followed by seed-mediated polyol-assisted reduction of Na_2PdCl_4 . They focused on the facet dependent CO_2 reduction catalytic activity of $\text{Pd NT/g-C}_3\text{N}_4$, which exhibits a CH_3OH and CH_4 production rate of $2.13 \mu\text{mol h}^{-1} \text{ g}^{-1}$ and $0.58 \mu\text{mol h}^{-1} \text{ g}^{-1}$, respectively, from activated ($\text{CO}_2 + \text{H}_2\text{O}$) vapor under 300 W visible light illumination (Table 3, entry 29).¹⁹³ Furthermore, DFT calculations confirm that the $\text{Pd}(100)$ facet over $\text{g-C}_3\text{N}_4$ exhibits high CO_2 uptake and high CO_2 binding energy and thus facilitates CH_3OH desorption. M. Humayun *et al.* have synthesized Au NP loaded P-doped $\text{g-C}_3\text{N}_4$ in ionic liquid followed by thermal annealing of a mixture of [1-butyl-3-methyl imidazoliumhexafluorophosphate (BmimPF_6) + dicyandiamide (DCDA)] and then finally the *in situ* photoreduction of HAuCl_4 for the decoration of Au NPs. The catalyst exhibits selective CH_4 evolution of $24 \mu\text{mol}$ in 5 h from CO_2 gas saturated H_2O under 300 W visible light (Table 3, entry 30).¹⁹⁴ The calculated quantum efficiency for CH_4 formation at 420 nm is $\sim 2.83\%$. The impressive catalytic activity is ascribed to the extended visible-light absorption along with the improved charge carrier separation *via* the phosphorus induced surface states and the Au nanoparticle decoration. The impact of Pt on the CO_2 reduction over $\text{g-C}_3\text{N}_4$ is revealed by W.-J. Ong *et al.*, using 2 wt% Pt loaded $\text{g-C}_3\text{N}_4$ nanocomposites. The catalyst exhibits the highest CH_4 yield of $13.02 \mu\text{mol g}^{-1} \text{ catalyst}^{-1}$ after 10 h of light irradiation, which is 5.1-fold higher in comparison with pure $\text{g-C}_3\text{N}_4$ ($2.55 \mu\text{mol g}^{-1} \text{ catalyst}^{-1}$), from CO_2 gas dissolved in H_2O under a 300 W xenon lamp (Table 3, entry 31).¹⁹⁵ The enhancement in the photocatalytic activity of the $\text{Pt/g-C}_3\text{N}_4$ nanocomposite for CO_2 photo-reduction CH_4 production can be attributed to the enhanced visible light absorption and smooth interfacial photogenerated electron transfer from $\text{g-C}_3\text{N}_4$ to Pt by lowering the Fermi level of Pt in the $\text{Pt/g-C}_3\text{N}_4$ hybrid as evidenced by the UV-vis and photoluminescence studies. The accumulated electron density on Pt facilitates the reduction of CO_2 to CH_4 *via* a multi-electron transfer process.

5.3 Critical factors regarding catalytic activity assessment and result presentation

Amidst the CO_2 photoreduction reports published in several journals, there is great concern regarding the precise catalytic activity evaluation, supportive characterization, and data presentation. Despite addressing this matter in several perspectives, edge articles, and editorials, this problem still persists.^{196–200} Although the intention is not to indicate or draw attention to any inappropriateness about the results reported on $\text{g-C}_3\text{N}_4$ for CO_2 photoreduction, the aim is to emphasize and regulate the standard requirements for a particular report that can be followed precisely by the readers. The following points may be considered during an experiment and result presentation. If $\text{g-C}_3\text{N}_4$ is the appointed photocatalyst, the abundance or source of carbon in the resultant product may be ensured with



a ^{13}C isotope tracing experiment since the catalyst itself is a carbonaceous material which eventually may be contributing as a carbon source. The amount of catalyst and co-catalyst may be clearly mentioned; otherwise, it is hard to follow since only the amount of catalyst can decide the rate of product formation and TON/TOF calculation. For obtaining the CO_2 reduction mechanism, *in situ*/DRIFT IR, HPLC, and GC-MS are the standard requirements that may be carried out. Since the activity is solely dependent on the CO_2 -uptake capacity, therefore as a matter of fact CO_2 -adsorption and CO_2 -TPD analysis may be considered. The binding energy of CO_2 over the catalyst surface will also provide useful information. Pre-requisite knowledge about the applied light source and especially the cut-on/off filter is also a vital factor. A cut-off filter implies the upward wavelength above the specified wave-length and *vice versa* in the case of a cut-on filter. The apparent quantum yield may be reported using monochromatic light only otherwise it is not appropriate to report as per the definition of the quantum yield. On many occasions, it has been reported by considering a range of wavelengths, which has no real scientific significance. For comparative purposes, only the quantum yield is a parameter suitable for consideration, since the activity and rate are definitely variable factors depending on the type of the photo-reactor and the amount of the catalyst used. Also, when the quantum yield is mentioned, the time must be mentioned as with the progress of the reaction the yield also increases and thus it is a collective parameter. Consequently, the product yield may not be reported like $\mu\text{mmol g}^{-1} \text{h}^{-1}$ as the amount and time are two variable factors. Also, the catalytic activity is not always linearly enhanced with time or amount. For example, catalysts which are close to the surface of the exposed site of incoming light illumination will exhibit better activity than a bulk amount settled at the bottom of the reactor. It is always advisable to report only the amount of product formed along with specifying the other reaction parameters. Also for comparison purposes, the solid-gas phase induced CO_2 reduced products may not be compared with the suspension medium even in the case of the same catalyst since the entire reaction condition is different, and thus it is not at all comparable. A minor alteration can change the entire catalytic investigation, which would mislead the readers. Therefore, these cumulative points may be considered during and after performing any CO_2 photoreduction reaction.

5.4 Device fabrication using $\text{g-C}_3\text{N}_4$ -based materials in photocatalysis

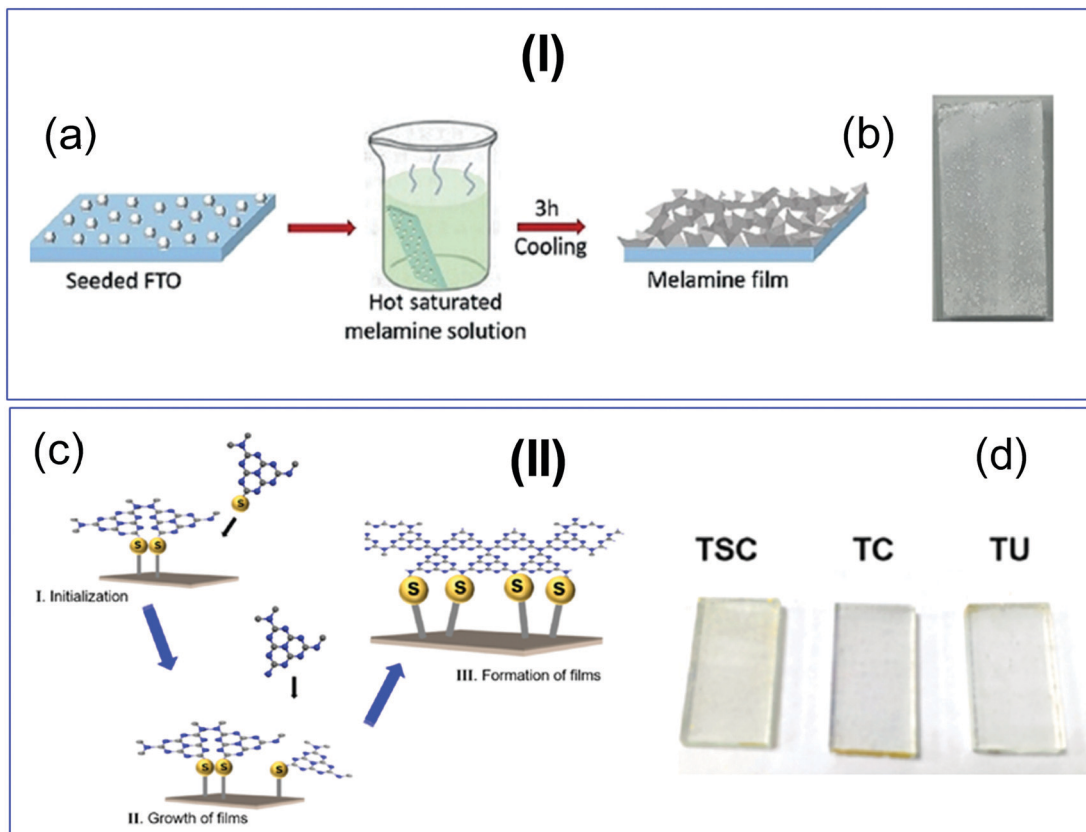
Miniaturization of the photocatalytic process *via* device fabrication is an important step towards industrial deployment that fulfills social demands. The progress in this direction over $\text{g-C}_3\text{N}_4$ catalysts is very little explored. Moreover, a $\text{g-C}_3\text{N}_4$ based device for the photocatalytic CO_2 conversion to C_1 fuel is not yet reported to the best of our knowledge. The effective device ideally should have provisions for (a) CO_2 capture and (b) its conversion to C_1 fuels under natural sunlight, on-board, in the same unit. Powder $\text{g-C}_3\text{N}_4$ -induced suspension photocatalysis may not be suitable for this purpose. The catalyst effectively

captures solar photons when it is fabricated as a film. Therefore, coating $\text{g-C}_3\text{N}_4$ powder over a conducting surface like fluorine-doped-tin oxide (FTO) or synthesis of a layer by layer free-standing $\text{g-C}_3\text{N}_4$ thin film can accomplish this requirement. Therefore, significant efforts are required to develop a prototype for the industrial-scale conversion of CO_2 to fuel. However, one can get some insight from the already developed $\text{g-C}_3\text{N}_4$ based devices for photoelectrochemical (PEC) water-splitting.^{201–204} G. Peng *et al.* have reported a robust seed-growth method for the synthesis of a layer-packed crystalline $\text{g-C}_3\text{N}_4$ film on FTO using melamine as a precursor for carbon nitride followed by heating at high temperature (Scheme 16(I)).²⁰¹ The fabricated device exhibited an outstanding photocurrent density of $116 \mu\text{A cm}^{-2}$ *vs.* RHE without any sacrificial agent in a wide pH range (0–13).²⁰¹ The same author has reported a free-standing $\text{g-C}_3\text{N}_4$ paper-based electrode for hole-driven photoelectrochemical dye degradation at the anode and electron-driven H_2 gas production in a single setup. Here, the authors have used carbon paper instead of FTO, and this is considered to be a proof of concept for the simultaneous utilization of holes and electrons to perform disproportionation reactions.²⁰² The very same group reported a graphene oxide (GO) coupled crystalline carbon nitride film in an FTO photoelectrochemical cell for the water splitting reaction. This time, different amounts of GO and melamine were mixed in ethylene glycol by varying the contents, and then the resulting paste was thermally annealed at high temperature. The fabricated cell produced a photocurrent density of $124 \mu\text{A cm}^{-2}$ *vs.* RHE in the absence of a sacrificial agent under alkaline solution. Moreover, the fabricated cell has performed with long-standing durability, which could be attributed to the smooth junction formation between GO and $\text{g-C}_3\text{N}_4$, efficient charge separation, high electronic conductivity, and sizeable electrochemical surface area.²⁰³ In other exciting work, Y. Feng *et al.* have reported an adhesive interface containing a polymeric $\text{g-C}_3\text{N}_4$ film-based device for solar water splitting (Scheme 16(II)).²⁰⁴ The authors found that both sulfur and non-sulfur precursors are necessary to achieve a high current density of $100 \mu\text{A cm}^{-2}$ *vs.* RHE in NaOH electrolyte. $\text{g-C}_3\text{N}_4$ based device fabrication for PEC has recently been reviewed, and this could be very helpful in designing a prototype for photocatalytic CO_2 conversion to C_1 fuel or related applications.^{205,206}

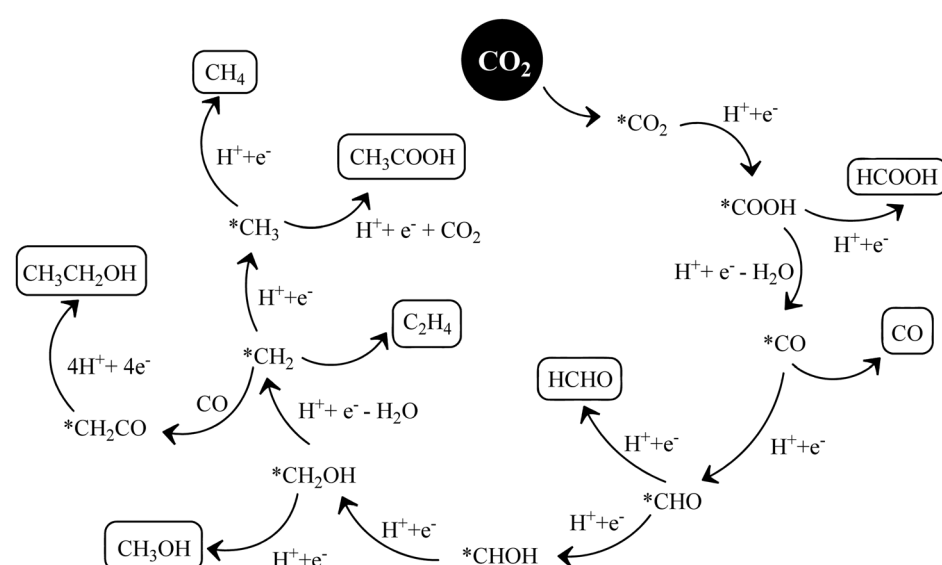
6. Electrocatalytic CO_2 reduction reaction (e- CO_2RR)

The electrocatalytic reduction of carbon dioxide into clean fuels is not fairly straightforward. In the last two decades, several research groups have studied purely metallic electrodes for this purpose and have segregated them based on the products that are obtained during the electrocatalytic CO_2 reduction reaction (e- CO_2RR) and the photoelectrocatalytic CO_2 reduction reaction (pe- CO_2RR). There are three major steps involved during the heterogeneous catalytic conversion of CO_2 on the electrode surface: (i) adsorption of the originally linear CO_2 molecule





Scheme 16 (I) (a) Fabrication of a crystalline carbon nitride based-PEC device, and (b) the resultant FTO based device, reprinted with permission, Copyright John Wiley and Sons, ref. 201; and (II) (c) a polymeric carbon nitride-based adhesive connected-PEC device, and (d) corresponding images of the FTO coated PEC devices synthesized from different precursors: TSC-thiobenzimidazole, TC-tri-thiocyanuric acid, TU-thiourea and urea, respectively, reprinted with permission, Copyright American Chemical Society, ref. 204.



Scheme 17 Various products formed due to multi-step processes during electrochemical CO_2 reduction.

during such processes is diverse. They include carbon monoxide, formic acid or formate, formaldehyde, methanol, ethanol, methane, ethylene *etc.* The half-cell reactions involved in these processes along with their standard electrode potentials have already been listed in Section 5.1.1.

6.1 The various rudiments of an e-CO₂RR experiment

Based on the mechanistic pathways of the abovementioned processes, electrocatalysts can be tailored for efficient performance and high selectivity. The performance of various electrocatalysts can be judged by electrochemical techniques such as linear sweep voltammetry (LSV), cyclic voltammetry (CV) and electrochemical impedance spectroscopy (EIS). While the overpotentials can be calculated for different products at various current densities directly from the LSV and CV profiles, the kinetics can be understood using the Tafel slopes that can be derived from the relevant voltammograms and/or the impedance spectra. All experiments should be performed using a two-compartment H-shaped electrochemical cell separating the cathode and the anode. This separation can be achieved using a thin frit glass membrane or a semi-permeable conducting membrane such as that of Nafion. A detailed gas-leak-proof setup design has been proposed by Pander *et al.*²⁰⁹ Since e-CO₂RR involves the reduction of CO₂, the working electrode is always a cathode which is capable of reducing other gaseous contaminants such as O₂ and N₂. Therefore, the e-CO₂RR process should be preceded by the removal of air from the cathodic chamber. Subsequently, to accurately determine the products formed during the e-CO₂RR, it is inevitable to saturate the cathodic chamber with high purity CO₂. The electrolyte is generally KHCO₃ and the counter-electrode (anode in this case) is graphite or a carbon electrode. In several cases, researchers have demonstrated the e-CO₂RR in KOH medium in order to elevate the pH, and, thereby, suppress the reduction of protons/water (hydrogen evolution). However, saturation of the KOH electrolyte with CO₂ reduces its pH due to the spontaneous formation of K₂CO₃ and KHCO₃. Although the pH is maintained between 6.8 and 7.5 under normal conditions, the exact pH of the medium should be monitored to correctly convert the potential *vs.* reference electrode (commonly, a pre-calibrated Ag/AgCl or SCE) to the potential *vs.* reversible hydrogen electrode (RHE). The reference electrode is placed in the cathode chamber of the H-cell. The working electrode should be kept protected from metal impurities present in the electrolyte, such as that of Fe and Zn, in order to avoid poisoning and severe deterioration of the catalytic performance. For this, the aqueous electrolyte can be pre-electrolyzed so as to eradicate the contaminants by depositing them on a sacrificial cathode.²¹⁰ Chelex is another option to prevent metal ion deposition due to its chelating action. The current densities that are reported for electrochemical experiments such as CV, LSV *etc.* should be normalized with respect to the electrochemical surface area (ECSA), which can be calculated as per an earlier report.²¹¹ To evaluate the faradaic efficiencies (FE) of various electrocatalysts, the aforesaid electrochemical measurements are generally correlated with the

chromatograms obtained from GC (gas chromatography) and/or HPLC (high-performance liquid chromatography) of the product mixtures. A bulk-electrolysis experiment should be carried out for about an hour to obtain products that are enough for further analysis.²¹² It is wise to carry out experiments under potentiostatic conditions to avoid deviations from the product selectivity. Galvanostatic experiments are likely to generate potentials that are not suitable for the e-CO₂RR, or can generate a variety of products. However, the latter may be preferred only under certain special conditions where the working electrode is studied well in advance and the applied current is precise for scaling up e-CO₂RR processes.²⁰⁹ The complexity of e-CO₂RR experiments, therefore, lies in the varied physical states of the products that are generated in the reaction medium. In the separate evaluation of the FE for various products, the faradaic selectivity or faradaic yield, defined as the fraction of the FE for a given product with respect to the total FE for all products, should also be calculated and reported. For the analysis of the H₂ gas which is invariably evolved during e-CO₂RR experiments due to very close potentials, the evolving gases should be directly delivered to the sampling loop of an online gas chromatograph equipped with a thermal conductivity detector (TCD) using argon as the inert carrier gas. Besides, a flame ionization detector (FID) should be used to analyze the possible carbon-containing gaseous products such as CO, CH₄, C₂H₄, and C₂H₆ as described in the mechanistic pathway (Scheme 17). On identification of the constituents present in the liquid (*e.g.*, HCOOH, CH₃OH, and C₂H₅OH) and gaseous mixtures, the selectivity of the product can be evaluated. Relevantly, nuclear magnetic resonance (NMR) spectroscopy and mass spectroscopy (MS) are often used to confirm the associated products. However, to minimize interfering proton signals arising from the aqueous electrolyte, a solvent-suppression method (suppresses the solvent peak, such as water) and deuterium locking (usually done to every NMR sample before acquisition of the spectra) should be necessarily adopted during NMR measurements.²⁰⁹ As the mechanistic pathway involved in the catalysis over a given heterogeneous surface may be completely changed with the change in the nanoarchitecture of various carbon-based electrodes, structural characterizations of the electrode materials are also important. These include Fourier transform-infrared (FT-IR) spectroscopy, Raman spectroscopy, X-ray diffraction measurements (XRD), X-ray photoelectron spectroscopy (XPS), X-ray absorption near-edge spectroscopy (XANES), X-ray absorption fine structure (XAES), scanning electron microscopy (SEM), transmission electron microscopy (TEM) and aberration-corrected-scanning transmission electron microscopy (AC-STEM). Even when coupled with active metallic catalyst nanoparticles, various carbon materials may often be seen generating very different products than what can be expected from the purely metallic catalysts. Hence, it is important to understand the structure–activity relationships of the active catalysts with the reactant and product molecules. For detailed analyses of these processes, *in situ* techniques are often used. To understand the source of CO₂ especially with carbon-based electrocatalysts or



Table 4 Electrocatalysts and electrocatalytic parameters of the CO₂ reduction reaction

E. no.	Electrocatalyst	Electrolyte	Major product (F.E., optimal potential)	Onset potential	Ref.
1.	2D-pg-C ₃ N ₄	2 M NaHCO ₃	CO (~80%, -0.35 V vs. RHE)	-0.13 V (vs. RHE)	214
2.	Au-BCN _{3.0} (gold decorated boron-doped carbon nitride)	0.5 M NaHCO ₃	Ethanol (78%)	0.15 V (vs. Ag/AgCl)	215
3.	BCN _{3.0} (boron-doped carbon nitride)	0.5 M NaHCO ₃	Ethanol (47%)	0.15 V (vs. Ag/AgCl)	217
4.	g-C ₃ N ₄ /MWCNT	0.5 M NaHCO ₃	CO (~60%, -0.75 V vs. RHE)	—	217
5.	Cu-C ₃ N ₄	0.1 M KHCO ₃	—	—	219
6.	Au/C ₃ N ₄	0.5 M KHCO ₃	CO (90%, -0.45 V vs. RHE)	—	220
7.	Au-CDot-C ₃ N ₄	0.5 M KHCO ₃	CO (79.8%)	-0.3 V	221
8.	OA-PCN (hydroxyl and amino functionalized polymeric carbon nitride)	0.5 M NaHCO ₃	CO (40.1%)	-0.56 V	222

electrode materials/substrates, it is often important to carry out isotopic ¹³C-labelling experiments where ¹³CO₂ is used as the feed gas instead of CO₂. Since the focus of this article is on C₃N₄-based electrodes that have been studied for CO₂ utilization to date, a relevant discussion in the said direction is imperative. Studies related to other carbon-based materials or carbon-free catalysts have however been regarded to exist beyond the scope of the present article.

6.2 Impact of g-C₃N₄ as an interesting e-CO₂RR catalyst

In recent times, heteroatom doping in carbon materials has evolved as an interesting domain of research to fine-tune their catalytic performances. For example, Sagara *et al.* have reported a boron-doped g-C₃N₄ photocathode catalyst that produces ethanol as the major product from CO₂ in an aqueous phase with or without the loading of metal nanoparticle co-catalysts Au, Ag or Rh for activity enhancement. It has been generally understood through this study that the enhanced production of ethanol is an outcome of restrained recombination of C1 moieties and the increased selectivity owing to metal nanoparticle loading could be due to the multi-electron reduction by electron capture on metal particles.²¹³ However, CO is generally the major product when Au or Ag is used as the catalyst, whereas alcohols are formed over Cu electrocatalysts.²¹⁴ Zhang *et al.* have reported a polarized few-layer metal-free g-C₃N₄ electrocatalyst that can selectively form CO (with trace HCOOH) from CO₂ with a high faradaic efficiency (F.E.) of ~80% (Table 4, entry 1).²¹⁴ This electrocatalyst has been prepared using hydrothermal pre-treatment of dicyandiamide followed by thermal exfoliation to reduce the number of stray basic sites. This catalyst is able to suppress the hydrogen evolution reaction and, thereby, efficiently catalyze CO₂ reduction. The authors have argued that the large surface area and mesoporous structure of the benchmark photocatalyst mpg-C₃N₄ (mesoporous graphitic carbon nitride) are not capable of electroreduction of CO₂ whereas the hierarchical structure of the foam-like monolith composed of 2D-pg-C₃N₄ is proven to facilitate the diffusion of carbon dioxide molecules to the active surface of the catalyst. Electrochemical impedance spectroscopy, further, has justified the improved mass transfer efficiency of 2D-pg-C₃N₄ exhibiting a larger slope in the low-frequency range (Table 4, entry 2).²¹⁵ This result is better than an earlier report on a metal-free g-C₃N₄/MWCNT electrocatalyst that converts CO₂ to CO. Of the total 98% faradaic efficiency obtained for H₂ and CO,

H₂ accounts for 58% of the total FE, while that of CO is only 41% (Table 4, entry 3).²¹⁶ Zhao *et al.* on the other hand have reported a ternary Au-CDot-C₃N₄ electrocatalyst with 4 wt% Au that can reduce CO₂ to CO selectively with an F.E. of ~79.8% at a potential of -0.5 V (vs. RHE). Employing theoretical calculations, the authors have proven the importance of the interaction between the CDots and C₃N₄. The authors have suggested the enhancement of the catalytic activity to be a direct outcome of the superior adsorption capability of CDots for both H⁺ and CO₂. A narrower bandgap of 1.35 eV due to the newly introduced valence band maximum has been observed in CDot-C₃N₄ in contrast to pure g-C₃N₄ (1.92 eV). Again, with the introduction of AuNPs, the electrocatalyst Au-CDot-C₃N₄ has shown a further decrease in the bandgap to 0.32 eV (Table 4, entry 3).²¹⁶ Also, adsorption studies have shown better capability of the 4 wt% Au-CDot-C₃N₄ electrocatalyst to adsorb both CO₂ (~0.34 mmol g⁻¹ at 1.2 atm) and H⁺ (0.37 g g⁻¹, on the basis of HCl) in comparison to 4 wt% Au-C₃N₄ (~0.22 mmol g⁻¹ at 1.2 atm of CO₂ and 0.18 mmol g⁻¹ of H⁺ on the basis of HCl) affirming the necessity of CDot incorporation (Table 4, entry 3).²¹⁷ Employing Cu as the most widely investigated probe for CO₂ reduction, Jiao *et al.* have studied g-C₃N₄ as a molecular scaffold that appropriately modifies the electronic structure of Cu in the resultant Cu-C₃N₄ complex. Through a combination of DFT computation and experimental justification, their work contributes to understanding the high selectivity of the e-CO₂RR toward hydrocarbons/alcohols. The existence of 'mock chemisorption' on the nitrogen atom of the C₃N₄ scaffold is suggested in the study, where CO₂ is adsorbed through a carbon-nitrogen bond on Cu-C₃N₄. This is believed to afford Cu-C₃N₄ to activate CO₂ with the application of a suitable electrode potential. Further, the C-centres of the C₃N₄ framework are shown to have a higher ability to bind with species that ligate using oxygen atoms such as *OCH₂, *OCH₃, *O, and *OH. This is due to the electrophilicity in the C-atoms of C₃N₄, which are connected to nitrogen atoms with high electronegativity. Moreover, the Cu active site is shown to have a higher preference to bind with intermediates, *COOH, *CO and *CHO, that use the C-centre for coordination. This kind of dual active center model has been demonstrated to uplift copper's d-orbital position toward the Fermi level, which is critical in adsorbing the intermediate for CO₂ activation. Their work successfully validates the formation of C2 products with the presence of two catalytically active centers (Table 4, entry 4).²¹⁸ In contrast to this mechanism for CO₂ activation,



Xu *et al.* have unraveled the intriguing role of nitrogen species in the carbon framework during the electroreduction of CO_2 (Table 4, entry 5).²¹⁹ They have enumerated the activity of four types of N-species present in N-doped carbon nanotubes: pyrrolic, pyridinic, and quaternary nitrogen. A conjugated outcome of systematic DFT calculations and experimental observations suggested that the improved activity in N-doped CNTs, in contrast to undoped CNTs, is due to the stabilization of the key intermediate $\text{CO}_2^{\cdot-}$. The best correlation is found to be the presence of quaternary N-species (Table 4, entry 5).²¹⁹ Recently, Zhang *et al.* have corroborated that carbon nitride supported Au nanoparticles ($\text{Au}/\text{C}_3\text{N}_4$) are better for CO_2 electroreduction than carbon-supported Au nanoparticles (Au/C). This is consistent with an earlier report²²⁰ and the study has been extended to the interaction of Ag with C_3N_4 . Experimental and theoretical data prove that C_3N_4 intensifies the electron-density over the Au surface, strengthening the adsorption of key reaction intermediate $^*\text{COOH}$. The F.E. for CO is found to be maintained above 90% over a wide potential window of -0.45 V to -0.85 V *vs.* RHE for $\text{Au}/\text{C}_3\text{N}_4$, while that for Au/C is always lesser than 80% in this range (Table 4, entry 6).²²⁰ This result is comparable to a recently reported electrocatalyst Au-Py-CNT-O which reportedly reduces CO_2 to CO with 93% F.E. over a wide potential range (-0.58 to -0.98 V) (Table 4, entry 7).²²¹ Meng *et al.*, in a recent report, have shown that a surface-modification strategy to introduce hydroxyl and amino groups on polymeric carbon nitride (PCN) can successfully be used to develop a metal-free electrocatalyst which is able to enhance the CO yield rate 17.1-fold as compared to its unmodified counterpart. The modification process has been carried out by treating PCN at 520 °C for 6 h in a controlled airflow to obtain O-PCN (PCN containing only hydroxyl species). Further, for 1 h O-PCN has been annealed in an NH_3 atmosphere to obtain OA-PCN (containing amino groups along with hydroxyl groups). The catalytic efficiency of OA-PCN towards CO_2 electroreduction is compared with that of A-PCN (containing only amino groups), O-PCN, and PCN. It is observed that the introduction of surface hydroxyl or amino groups alone cannot boost the e- CO_2RR rate but the one with both functional groups has been found to suppress hydrogen evolution, thereby enhancing the rate of CO production. The CO/H_2 ratio for the OA-PCN electrocatalyst is determined to be 0.67, which is in the range for the Fischer-Tropsch reaction (0.25–3.34). To investigate the ostensibly magical role of dual functionalization of PCN in the e- CO_2RR , density functional theory (DFT) calculations have been carried out. It is revealed that the conversion of CO_2 to COOH^* possessed the highest energy barrier of 0.62 eV at the NH_2 terminal. Furthermore, a higher barrier of 0.83 eV is required, at the $-\text{OH}$ terminal, to desorb the CO product. Therefore, mono-functionalization does not boost the overall performance. However, according to the theoretical calculations, it is possible to infer that a proton–electron transfer process initiates the generation of the $^*\text{COOH}$ intermediate at the $-\text{OH}$ terminal, which is transferred to the $-\text{NH}_2$ terminal and, then, converted to $^*\text{CO}$. The more facile desorption of the CO product is believed to occur at the $-\text{NH}_2$ terminal, thereby exhibiting a fascinatingly high performance of the dual functionalized OA-PCN electrocatalyst

(Table 4, entry 8).²²² From the perspective of consistency, reproducibility and ease of synthesis, C_3N_4 -based materials should, therefore, be advocated as efficient potential electrocatalysts for CO_2 reduction.

7. Overall summary, conclusions, and future perspectives

In summary, this article covered three important CO_2 conversion processes, thermal CO_2 activation, photocatalytic CO_2 conversion, and electrochemical CO_2 reduction, focused on the rising star carbonaceous material ‘g- C_3N_4 ’. A summary indicating the general characteristics, advantages, and disadvantages of the thermocatalytic/photocatalytic/electrocatalytic CO_2 conversion process is provided in Table 5.

The merits of g- C_3N_4 for the above mentioned processes are: (a) It is a thermally stable, non-toxic, easy to synthesize material at moderate temperature (550 °C), whereas other carbon-based catalysts need high temperature (1200–1400 °C) and also require chemical activation. (b) In contrast to other carbon materials, N-doped carbon materials, especially g- C_3N_4 , are more effective for acidic CO_2 activation and conversion. Tailored synthesis parameters, varied carbon and nitrogen precursors, and different synthesis strategies allowed us to synthesize g- C_3N_4 with different types of N species having Lewis and Brønsted basic sites (uncondensed $-\text{NH}_2$) suitable for CO_2 activation and utilization. Moreover, it is also possible to incorporate other functional sites in g- C_3N_4 so that a multi-functional catalyst for the appointed CO_2 activation reactions can be designed to deliver a designated product. (c) g- C_3N_4 is the only carbon catalyst having a bandgap energy with appropriate valence and conduction band edge potentials for the utilization of visible light of the solar spectrum. It can reduce CO_2 and oxidize H_2O simultaneously and thus effectively serve in the CO_2 photoreduction reaction. Except for carbon dots, all other carbons do not have any bandgap and, therefore, are photocatalytically inactive for the CO_2 reduction reaction. However, carbon dots cannot themselves trigger CO_2 reduction; instead, they need another support material eventually to exhibit their up-conversion photoluminescence property. (d) It is easy to functionalize g- C_3N_4 to improve the visible-light harnessing capability, which is not possible with other carbonaceous materials.

Some of the demerits of g- C_3N_4 are: (a) It is thermally stable, but it is prone to light-induced framework oxidation/decomposition. If CO_2 is a reactant, then it requires deep investigation because the framework oxidation/decomposition product and CO_2 derived product could give misleading information. Therefore, integrating g- C_3N_4 with another semiconductor is necessary to stop its framework degradation caused by light absorption. (b) It contains less oxygen in the form of hydroxyl groups, which is not enough to make it a steam reforming chemical looping catalyst. (c) It has low electrochemical conductivity and thus exhibits inferior activity for electrocatalytic CO_2 reduction. Moreover, in the absence of an



Table 5 Summary of the thermocatalytic/photocatalytic/electrocatalytic CO_2 conversion process

Process	General characteristics	Advantages	Disadvantages
Thermocatalytic	<p>(1) Thermal energy is the driving force to disrupt the stable atomic and molecular bonds of CO_2 and other reactants over a bi-functional catalyst to produce various platform chemicals and fuels.</p> <p>(2) Industrially available high-pressure liquid phase and gas phase reactors can be employed to convert CO_2 to important feedstock chemicals and fuels under the influence of mild to high CO_2 pressure (1–500 bar or so).</p> <p>(3) Catalysts can be easily designed for the appointed applications.</p>	<p>(1) Easy to implement in large scale production.</p> <p>(2) A variety of chemicals and building blocks can be produced.</p> <p>(3) Catalyst recovery is easy.</p> <p>(4) More than 90% of CO_2 is converted <i>via</i> this process.</p> <p>(5) Can be applied in a broad range of pressure (1–500 bar or so).</p> <p>(6) Thermodynamic and kinetic parameters can be easily tuned.</p>	<p>(1) Not sustainable due to the involvement of a non-renewable energy source.</p> <p>(2) The trade-off between conversion and energy efficiency is very low.</p> <p>(3) The requirement of high pressure and temperature.</p> <p>(4) Pure CO_2 gas is required.</p> <p>(5) Atmospheric CO_2 gas cannot be converted.</p>
Photocatalytic	<p>(1) The driving force is light-energy under ambient conditions to bring down the thermodynamic constraint of stable CO_2 molecules over a semiconductor photocatalyst having efficient photon capturing ability.</p> <p>(2) It depends on the chemisorption magnitude of CO_2 at $[P/P_0 = 1]$.</p> <p>(3) The design of a photocatalyst is more challenging than the thermocatalytic process.</p>	<p>(1) Light energy is available abundantly.</p> <p>(2) Eco-friendly and sustainable process.</p> <p>(3) A selective product can be achieved since one-pot CO_2 reduction and H_2O oxidation takes place.</p> <p>(4) The source of CO_2 can be varied and, accordingly, different products can be achieved.</p> <p>(5) Recyclability is high if a powder suspension system is employed.</p>	<p>(1) A custom-made catalytic reactor coupled with a suitable light source makes the process less user-friendly.</p> <p>(2) Low light-harnessing and quick charge carrier recombination of the photocatalyst are a major drawback.</p> <p>(3) Product isolation and separation are comparatively tough.</p> <p>(4) Mechanistic investigation is somewhat difficult.</p> <p>(5) The competitive reduction tendency between CO_2 and H^+ by the light-induced electrons suppresses the overall activity.</p> <p>(6) Large-scale implementation and night time operation are not possible due to the absence of sunlight.</p> <p>(7) Only low CO_2 pressure can be employed (<10 bar).</p> <p>(8) Atmospheric CO_2 gas cannot be converted.</p>
Electrocatalytic	<p>(1) A suitable external potential is a driving force (under ambient conditions) to bring down the thermodynamic constraint of a stable CO_2 molecule over a highly electrochemically conductive electrocatalyst.</p> <p>(2) Mainly carried out under alkaline solution as a CO_2 source.</p> <p>(3) Electrolyte and potential bias both play a key role.</p> <p>(4) The design of an electrocatalyst is highly challenging.</p>	<p>(1) Easy to operate.</p> <p>(2) Eco-friendly and sustainable process.</p> <p>(3) Highly economic.</p> <p>(4) The trade-off between conversion and energy efficiency is very high.</p> <p>(5) Product selectivity can be finely tuned.</p> <p>(6) Less dependent on the CO_2 chemisorption process.</p> <p>(7) The liquid phase reaction medium is primarily followed.</p> <p>(8) High turnover number (TON) and turnover frequency (TOF).</p>	<p>(1) It is extremely difficult to design the electrocatalytic reactor.</p> <p>(2) An appropriate membrane is difficult to synthesize.</p> <p>(3) A redox-active metal is required owing to its inherent redox properties.</p> <p>(4) Catalyst recovery is very difficult if a thin-film is used.</p> <p>(5) Product quantification from a basic medium by GC, GC-MS, and HPLC leads to low yield.</p> <p>(6) Only low CO_2 pressure can be employed (<10 bar).</p> <p>(7) Atmospheric CO_2 gas cannot be converted.</p> <p>(8) Mechanistic investigation is difficult.</p>



active metal, it exhibits limited redox activity in electrochemical CO_2 reduction. Other carbonaceous materials, primarily N-doped carbons, are more suitable for electrochemical CO_2 reduction owing to their superior electronic conductivity. (d) Porous carbon can be derived from any natural resources, but specific carbon and nitrogen-containing precursors are required for $\text{g-C}_3\text{N}_4$ synthesis. Moreover, it is a visible light active catalyst and cannot cover the UV and NIR regions of the solar spectrum, which is also a drawback for its limited photocatalytic CO_2 reduction activity.

The most crucial feature of $\text{g-C}_3\text{N}_4$ is its facile synthesis, which can be performed without any complex synthesis setup. But plenty of research is required to improve its catalytic CO_2 conversion efficiency. $\text{g-C}_3\text{N}_4$ exhibited activity in all these three processes but with limited efficiency. For example, thermal CO_2 activation needs high temperature and pressure, which is not sustainable. Moreover, the involvement of an added co-catalyst raises the question of its effectiveness. Integrating an alkali metal oxide with the $\text{g-C}_3\text{N}_4$ framework can enhance CO_2 adsorption and activation. Therefore, further improvement of $\text{g-C}_3\text{N}_4$ based catalysts is required for CO_2 ambient condition activation and utilization. Since $\text{g-C}_3\text{N}_4$ does not have enough oxygen content, integrating it with transition metal oxides like CeO_2 and MnO_2 , or spinel based oxides like NiCo_2O_4 with high oxygen exchange capacity can make it an active catalyst for steam reforming of methane coupled with the CO_2 splitting reaction. In the case of photocatalytic CO_2 reduction, the target of mole scale product yield is not yet achieved. Moreover, selectivity control and inclusion of additional organic additives like acetonitrile and dimethylformamide, and sacrificial agents like triethanolamine along with a co-catalyst are the serious drawbacks of this photocatalytic process. It is noteworthy that an ideal CO_2 photoreduction system involves a light-harvesting material, CO_2 gas, and H_2O only. But very rarely has this target been served by this catalyst to date. Another controversial aspect is the source of carbon in the converted product during CO_2 photo-reduction, especially when the catalyst itself is a carbon-based material. Utilization of suitable precursors during thermal polymerization (or other synthesis strategies) can incorporate required C, N, O, or S functionalities that have the capability to alter its solar light harnessing capability and can improve the charge carrier separation suitable for high photocatalytic CO_2 reduction reaction activity. Another vital area is the configuration of thin-film based-device fabrication for practical CO_2 photoreduction. $\text{g-C}_3\text{N}_4$ has a triazine skeleton, and therefore single-metal-atoms can be entrapped in the framework *via* wet impregnation followed by thermal annealing in a reducing environment. It will minimize attrition and deactivation, which are advantages for catalyst long term stability. High overpotential, low current densities, and limited redox-tunability are the shortcomings in its electrochemical CO_2 reduction application. Therefore these concerns should be carefully considered for its further efficiency improvement. Carbon nitride-based single-atom-catalysts can be a viable solution to improve photocatalytic, electrocatalytic, or photoelectrocatalytic CO_2 reduction.

We have concisely covered almost all the parameters starting from the synthesis of materials to fundamentals of CO_2

activation, followed by critical operational parameters for collective 'thermo-photo-electro'-chemical CO_2 conversion focusing on the $\text{g-C}_3\text{N}_4$ catalyst. The conclusion section has provided the details of the merits and demerits of $\text{g-C}_3\text{N}_4$ along with a concise perspective on the application of carbon nitride for CO_2 conversion. We envisage that this review will be helpful for beginners in their early stage of research on heterogeneous CO_2 conversion reactions for further technological advancement in the 21st century.

Author contributions

The theme of the review article was proposed by SS and RS jointly. The manuscript was co-written by S. S. and R. S. The authors thank Mr Aniruddha Mukherjee for the preparation of some figures and helpful discussion and drafting the electrochemical section. All the authors proofread and approved the final version of the manuscript.

Conflicts of interest

The authors state that no competitive and non-competitive conflicts of interest exist to declare. The authors also declare that some of the figures included in this manuscript have been prepared by themselves with the appropriate citations wherever it is applicable. Copyright permission has been obtained for the required figures of this manuscript.

Acknowledgements

RS is grateful to the Director IIT Ropar for the Mid-career Excellence in Research through grant number 9-35/2009/IITRPR/3121. SS acknowledges the research fellowship received from the Ministry of Human Resource Development, New Delhi, and Director's Fellowship, IIT Ropar. We also thank the anonymous reviewers for their critical comments for the quality improvement of our review article.

References

- 1 G. Savulich, F. H. Hezemans, V. G. Grothe, J. Dafflon, N. Schulten, A. B. Brühl, B. J. Sahakian and T. W. Robbins, *Transl. Psychiatry*, 2019, 9, 296.
- 2 <https://www.ipcc.ch/report/2019-refinement-to-the-2006-ipcc-guidelines-for-national-greenhouse-gas-inventories/>.
- 3 P. W. Barnes, C. E. Williamson and R. M. Lucas, *et al.*, *Nat. Sustainability*, 2019, 2, 569–579.
- 4 M. G. Lawrence, S. Schäfer, H. Muri, V. Scott, A. Oschlies, N. E. Vaughan, O. Boucher, H. Schmidt, J. Haywood and J. Scheffran, *Nat. Commun.*, 2018, 9, 3734.
- 5 A. V. Herzog, T. E. Lipman and D. M. Kammen. *Renewable energy sources*, Encyclopedia of life support systems (EOLSS) forerunner volume-perspectives and overview of life support systems and sustainable development, 2001.

6 Environmental Impact Comparison of Steam Methane Reformation and Thermochemical Processes of Hydrogen Production G. F. Naterer, O. Jaber, I. Dincer, Detlef Stolten, Thomas Grube (ed.): 18th World Hydrogen Energy Conference 2010 – WHEC 2010 Parallel Sessions Book 3: Hydrogen Production Technologies – Part 2 Proceedings of the WHEC, May 16–21. 2010, Essen Schriften des Forschungszentrums Jlich/Energy & Environment, Vol. 78-3 Institute of Energy Research-Fuel Cells (IEF-3) Forschungszentrum Jlich GmbH, Zentralbibliothek, Verlag, 2010 ISBN: 978-3-89336-653-8.

7 T. P. Senftle and Emily A. Carte, *Acc. Chem. Res.*, 2017, **50**, 472–475.

8 E. S. Sanz-Perez, C. R. Murdock, S. A. Didas and C. W. Jones, *Chem. Rev.*, 2016, **116**, 11840–11876.

9 S. A. Didas, S. Choi, W. Chaikittisilp and C. W. Jones, *Acc. Chem. Res.*, 2015, **48**, 2680–2687.

10 B. Dutcher, M. Fan and A. G. Russell, *ACS Appl. Mater. Interfaces*, 2015, **7**, 2137–2148.

11 D. M. Reiner, *Nat. Energy*, 2016, **1**, 15011.

12 F. A. Rahman, M. M. A. Aziz, R. Saidur, W. A. Bakar, M. R. Hainin, R. Putrajaya and N. A. Hassan, *Renewable Sustainable Energy Rev.*, 2017, **71**, 112–126.

13 R. S. Haszeldine, *Science*, 2009, **325**, 1647–1652.

14 Q. Wang, J. Luo, Z. Zhong and Z. A. Borgna, *Energy Environ. Sci.*, 2011, **4**, 42–55.

15 F. Akhtar, Q. Liu, N. Hedin and L. Bergström, *Energy Environ. Sci.*, 2012, **5**, 7664–7673.

16 D. Bonenfant, M. Kharoune, P. Niquette, M. Mimeaule and R. Hausler, *Sci. Technol. Adv. Mater.*, 2008, **9**, 013007.

17 R. Banerjee, H. Furukawa, D. Britt, C. Knobler, M. O'Keeffe and O. M. Yaghi, *J. Am. Chem. Soc.*, 2009, **131**, 3875–3877.

18 S. Xiang, Y. He, Z. Zhang, H. Wu, W. Zhou, R. Krishna and B. Chen, *Nat. Commun.*, 2012, **3**, 954.

19 J. Liu, P. K. Thallapally, B. P. McGrail, D. R. Brown and J. Liu, *Chem. Soc. Rev.*, 2012, **41**, 2308–2322.

20 J. Wang, A. Heerwig, M. R. Lohe, M. Oschatz, L. Borchardt and S. Kaskel, *J. Mater. Chem.*, 2012, **22**, 13911–13913.

21 J. Gong, M. Antonietti and J. Yuan, *Angew. Chem., Int. Ed.*, 2017, **56**, 7557–7563.

22 F. Inagaki, C. Matsumoto, T. Iwata and C. Mukai, *J. Am. Chem. Soc.*, 2017, **139**, 4639–4642.

23 M. Oschatz, M. Leistner, W. Nickel and S. Kaskel, *Langmuir*, 2015, **31**, 4040–4047.

24 V. Presser, J. McDonough, S.-H. Yeon and Y. Gogotsi, *Energy Environ. Sci.*, 2011, **4**, 3059–3066.

25 W. G. Tu, Y. Zhou and Z. G. Zou, *Adv. Mater.*, 2014, **26**, 4607–4626.

26 J. Lee, D. C. Sorescu and X. Deng, *J. Am. Chem. Soc.*, 2011, **33**, 10066–10069.

27 E. Karamian and S. Sharifnia, *J. CO₂ Util.*, 2016, **16**, 194–203.

28 R. Srivastava, D. Srinivas and P. Ratnasamy, *J. Catal.*, 2005, **233**, 1–15.

29 R. Srivastava, D. Srinivas and P. Ratnasamy, *Catal. Lett.*, 2003, **91**, 133–139.

30 N. Keller, G. Rebmann and V. Keller, *J. Mol. Catal. A: Chem.*, 2010, **317**, 1–18.

31 J. E. Hallgren, *US Pat.*, US4410464A, 1983.

32 S. Fukuoka, M. Kawamura, K. Komiya, M. Tojo, H. Hachiya, K. Hasegawa, M. Aminaka, H. Okamoto, I. Fukawad and S. Konnog, *Green Chem.*, 2003, **5**, 497–507.

33 Z. Marković, S. Marković, N. Manojlović and J. Predojević-Simović, *J. Chem. Inf. Model.*, 2007, **47**, 1520–1525.

34 K. C. Waugh, *Catal. Today*, 1992, **15**, 51–75.

35 L.-H. Zhang, W.-C. Li, L. Tang, Q.-G. Wang, Q.-T. Hu, Y. Zhang and A.-H. Lu, *J. Mater. Chem. A*, 2018, **6**, 24285–24290.

36 G.-P. Hao, Z.-Y. Jin, Q. Sun, X.-Q. Zhang, J.-T. Zhang and A.-H. Lu, *Energy Environ. Sci.*, 2013, **6**, 3740.

37 Y. Xia, R. Mokaya, G. S. Walker and Y. Zhu, *Adv. Energy Mater.*, 2011, **1**, 678–683.

38 F. Rodfguez-reinoso, *Carbon*, 1998, **36**, 159–175.

39 X. Shao, Z. Feng, R. Xue, C. Ma, W. Wang, X. Peng and D. Cao, *AIChE J.*, 2011, **57**, 3042–3051.

40 R. Wang, P. Wang, X. Yan, J. Lang, C. Peng and Q. Xue, *ACS Appl. Mater. Interfaces*, 2012, **4**, 5800–5806.

41 J. Chen, J. Yang, G. Hu, X. Hu, Z. Li, S. Shen, M. Radosz and M. Fan, *ACS Sustainable Chem. Eng.*, 2016, **4**, 1439–1445.

42 R. J. White, V. Budarin, R. Luque, J. H. Clark and D. J. Macquarrie, *Chem. Soc. Rev.*, 2009, **38**, 3401–3418.

43 C. Robertson and R. Mokaya, *Microporous Mesoporous Mater.*, 2013, **179**, 151–156.

44 M. Sevilla and A. B. Fuertes, *Energy Environ. Sci.*, 2011, **4**, 1765.

45 Z. Liu, Z. Zhang, Z. Jia, L. Zhao, T. Zhang, W. Xing, S. Komarneni, F. Subhan and Z. Yan, *Chem. Eng. J.*, 2018, **337**, 290–299.

46 T.-Y. Ma, L. Liu and Z.-Y. Yuan, *Chem. Soc. Rev.*, 2013, **42**, 3977–4003.

47 Y. Meng, D. Gu, F. Zhang, Y. Shi, H. Yang, Z. Li, C. Yu, B. Tu and D. Zhao, *Angew. Chem., Int. Ed.*, 2005, **44**, 7053–7059.

48 Z. Xing, N. Gao, Y. Qi, X. Ji and H. Liu, *Carbon*, 2017, **115**, 271–278.

49 T. Kim, J. Lee and K.-H. Lee, *RSC Adv.*, 2016, **6**, 24667–24674.

50 Y. Zhao, H. Ding and Q. Zhong, *Appl. Surf. Sci.*, 2012, **258**, 4301–4307.

51 C. Lu, H. Bai, B. Wu, F. Su and J. F. Hwang, *Energy Fuels*, 2008, **22**, 3050–3056.

52 R. Vaidhyanathan, S. S. Iremonger, G. K. H. Shimizu, P. G. Boyd, S. Alavi and T. K. Woo, *Science*, 2010, **330**, 650–653.

53 W. Xing, C. Liu, Z. Zhou, L. Zhang, J. Zhou, S. Zhuo, Z. Yan, H. Gao, G. Wang and S. Z. Qiao, *Energy Environ. Sci.*, 2012, **5**, 7323–7327.

54 D. Qian, C. Lei, E.-M. Wang, W.-C. Li and A.-H. Lu, *ChemSusChem*, 2014, **7**, 291–298.

55 J. V. Liebig, *Ann. Pharm.*, 1834, **10**, 10.

56 F. Goettmann, A. Fischer, M. Antonietti and A. Thomas, *Chem. Commun.*, 2006, 4530–4532.

57 X. Wang, K. Maeda, A. Thomas, K. Takanabe, G. Xin, J. M. Carlsson, K. Domen and M. Antonietti, *Nat. Mater.*, 2009, **8**, 76–80.



58 D. M. Teter and R. J. Hemley, *Science*, 1996, **271**, 53–55.

59 A. Thomas, A. Fisher, F. Goettmann, M. Antonietti, J. O. Muller, R. Schlogl and R. Carlsson, *J. Mater. Chem.*, 2008, **18**, 4893–4908.

60 E. Kroke, M. Schwarz, E. Horath-Bordon, P. Kroll, B. Noll and A. D. Norman, *New J. Chem.*, 2002, **26**, 508–512.

61 B. Jurgens, E. Irran, J. Senker, P. Kroll, H. Muller and W. Schnick, *J. Am. Chem. Soc.*, 2003, **125**, 10288–10300.

62 F. R. Pomilla, M. A. L. R. M. Cortes, J. W. J. Hamilton, R. Molinari, G. Barbieri, G. Marci, L. Palmisano, P. K. Sharma, A. Brown and J. A. Byrne, *J. Phys. Chem. C*, 2018, **122**, 28727–28738.

63 C. Chen, J. Kim and W.-S. Ahn, *Fuel*, 2012, **95**, 360–364.

64 B. Zhu, K. Li, J. Liu, H. Liu, C. Sun, C. E. Snape and Z. Guo, *J. Mater. Chem. A*, 2014, **2**, 5481–5489.

65 P. P. Sharma, J. J. Wu, R. M. Yadav, M. J. Liu, C. J. Wright, C. S. Tiwary, B. I. Yakobson, J. Lou, P. M. Ajayan and X. D. Zhou, *Angew. Chem., Int. Ed.*, 2015, **54**, 13701–13705.

66 S. Ni, Z. Y. Li and J. L. Yang, *Nanoscale*, 2012, **4**, 1184–1189.

67 M. Sevilla, P. Valle-Vigón and A. B. Fuertes, *Adv. Funct. Mater.*, 2011, **21**, 2781–2787.

68 J. Zhou, W. Li, Z. Zhang, W. Xing and S. Zhuo, *RSC Adv.*, 2012, **2**, 161–167.

69 X. Wang, K. Maeda, A. Thomas, K. Takanabe, G. Xin, J. M. Carlsson, K. Domen and M. Antonietti, *Nat. Mater.*, 2009, **8**, 76–80.

70 S. C. Yan, Z. S. Li and Z. G. Zou, *Langmuir*, 2009, **25**, 10397–10401.

71 Y. Zhang, J. Liu, G. Wu and W. Chen, *Nanoscale*, 2012, **4**, 5300–5303.

72 Z. Mo, X. She, Y. Li, L. Liu, L. Huang, Z. Chen, Q. Zhang, H. Xu and H. Li, *RSC Adv.*, 2015, **5**, 101552–101562.

73 D. Hollmann, M. Karnahl, S. Tschierlei, K. Kailasam, M. Schneider, J. Radnik, K. Grabow, U. Bentrup, H. Junge and M. Beller, *Chem. Mater.*, 2014, **26**, 1727–1733.

74 F. Dong, Z. Wang, Y. Sun, W.-K. Ho and H. Zhang, *J. Colloid Interface Sci.*, 2013, **401**, 70–79.

75 P. Niu, L. Zhang and G. Liu, *Adv. Funct. Mater.*, 2012, **22**, 4763–4770.

76 F. He, G. Chen, Y. Zhou, Y. Yu, Y. Zheng and S. Hao, *Chem. Commun.*, 2015, **51**, 16244–16246.

77 B. Long, J. Lin and X. Wang, *J. Mater. Chem. A*, 2014, **2**, 2942–2951.

78 P. Niu, L.-C. Yin, Y.-Q. Yang, G. Liu and H.-M. Cheng, *Adv. Mater.*, 2014, **26**, 8046–8052.

79 S. Yang, Y. Gong, J. Zhang, L. Zhan, L. Ma, Z. Fang, R. Vajtai, X. Wang and P. M. Ajayan, *Adv. Mater.*, 2013, **25**, 2452–2456.

80 T. Sano, S. Tsutsui, K. Koike, T. Hirakawa, Y. Teramoto, N. Negishi and K. Takeuchi, *J. Mater. Chem. A*, 2013, **1**, 6489–6496.

81 J. Tong, L. Zhang, F. Li, M. Li and S. Cao, *Phys. Chem. Chem. Phys.*, 2015, **17**, 23532–23537.

82 K. S. Lakhi, D.-W. Park, K. Al-Bahily, W. Cha, B. Viswanathan, J.-H. Choy and A. Vinu, *Chem. Soc. Rev.*, 2017, **46**, 72–101.

83 F. Goettmann, A. Fischer, M. Antonietti and A. Thomas, *Angew. Chem., Int. Ed.*, 2006, **45**, 4467–4471.

84 Y.-S. Jun, W. H. Hong, M. Antonietti and A. Thomas, *Adv. Mater.*, 2009, **21**, 4270–4274.

85 J. Zhang, F. Guo and X. Wang, *Adv. Funct. Mater.*, 2013, **23**, 3008–3014.

86 Y. Wang, X. Wang and M. Antonietti, *Angew. Chem., Int. Ed.*, 2012, **51**, 68–89.

87 J. Wang, C. Zhang, Y. Shen, Z. Zhou, J. Yu, Y. Li, W. Wei, S. Liu and Y. Zhang, *J. Mater. Chem. A*, 2015, **3**, 5126–5131.

88 W. Shen, L. Ren, H. Zhou, S. Zhang and W. Fan, *J. Mater. Chem.*, 2011, **21**, 3890–3894.

89 Y. Wang, X. Wang, M. Antonietti and Y. Zhang, *ChemSusChem*, 2010, **3**, 435–439.

90 Y. Wang, J. Zhang, X. Wang, M. Antonietti and H. Li, *Angew. Chem., Int. Ed.*, 2010, **49**, 3356–3359.

91 Y.-S. Jun, E. Z. Lee, X. Wang, E. W. Hong, G. D. Stucky and A. Thomas, *Adv. Funct. Mater.*, 2013, **23**, 3661–3667.

92 M. Shalom, M. Guttentag, C. Fettkenhauer, S. Inal, D. Neher, A. Llobet and M. Antonietti, *Chem. Mater.*, 2014, **26**, 5812–5818.

93 Y. Liao, S. Zhu, J. Ma, Z. Sun, C. Yin, C. Zhu, X. Lou and D. Zhang, *ChemCatChem*, 2014, **6**, 3419–3425.

94 T. Jordan, N. Fechler, J. Xu, T. J. K. Brenner, M. Antonietti and M. Shalom, *ChemCatChem*, 2015, **7**, 2826–2830.

95 J. Li, B. Shen, Z. Hong, B. Lin, B. Gao and Y. Chen, *Chem. Commun.*, 2012, **48**, 12017–12019.

96 Z.-F. Huang, J. Song, L. Pan, Z. Wang, X. Zhang, J.-J. Zou, W. Mi, X. Zhang and L. Wang, *Nano Energy*, 2015, **12**, 646–656.

97 Z. Zhao, Y. Sun, F. Dong, Y. Zhang and H. Zhao, *RSC Adv.*, 2015, **5**, 39549–39556.

98 S. Hu, L. Ma, J. You, F. Li, Z. Fan, F. Wang, D. Liu and J. Gui, *RSC Adv.*, 2014, **4**, 21657–21663.

99 Y. Zhou, L. Zhang, J. Liu, X. Fan, B. Wang, M. Wang, W. Ren, J. Wang, M. Li and J. Shi, *J. Mater. Chem. A*, 2015, **3**, 3862–3867.

100 J. Ran, T. Y. Ma, G. Gao, X.-W. Du and S. Z. Qiao, *Energy Environ. Sci.*, 2015, **8**, 3708–3717.

101 G. Liu, P. Niu, C. Sun, S. C. Smith, Z. Chen, G. Q. Lu and H.-M. Cheng, *J. Am. Chem. Soc.*, 2010, **132**, 11642–11648.

102 K. Wang, Q. Li, B. Liu, B. Cheng, W. Ho and J. Yu, *Appl. Catal., B*, 2015, **176–177**, 44–52.

103 J. Zhang, J. Sun, K. Maeda, K. Domen, P. Liu, M. Antonietti, X. Fu and X. Wang, *Energy Environ. Sci.*, 2011, **4**, 675–678.

104 S. C. Yan, Z. S. Li and Z. G. Zou, *Langmuir*, 2010, **26**, 3894–3901.

105 Y. Wang, H. Li, J. Yao, X. Wang and M. Antonietti, *Chem. Sci.*, 2011, **2**, 446–450.

106 H. Li, Y. Liu, X. Gao, C. Fu and X. Wang, *ChemSusChem*, 2015, **8**, 1189–1196.

107 S. Samanta and R. Srivastava, *Sustainable Energy Fuels*, 2017, **1**, 1390–1404.

108 S. Samanta, R. Yadav, A. Kumar, A. K. Sinha and R. Srivastava, *Appl. Catal., B*, 2019, **259**, 118054.

109 Y. Gao, K. Qian, B. Xu, Z. Li, J. Zheng, S. Zhao, F. Ding, Y. Sun and Z. Xu, *Carbon Resour. Convers.*, 2020, **3**, 46–59.



110 A. Akhundi, A. Habibi-Yangjeh, M. Abitorabi and S. R. Pouran, *Catal. Rev.*, 2019, **61**, 595–628.

111 M. Shen, L. Zhang and J. Shi, *Nanotechnology*, 2018, **29**, 412001.

112 C. H. Bartholomew, *Chem. Eng.*, 1984, **91**, 96–112.

113 J.-S. Chang, V. P. Vislovskiy, M.-S. Park, D. Y. Hong, J. S. Yoo and S.-E. Park, *Green Chem.*, 2003, **5**, 587–590.

114 M.-O. Sugino, H. Shimada, T. Turuda, H. Miura, N. Ikenaga and T. Suzuki, *Appl. Catal., A*, 1995, **121**, 125–137.

115 V. Ansari and S.-E. Park, *Energy Environ. Sci.*, 2012, **5**, 9419–9437.

116 F. Goettmann, A. Thomas and M. Antonietti, *Angew. Chem., Int. Ed.*, 2007, **46**, 2717–2720.

117 M. B. Ansari, B.-H. Min, Y.-H. Mo and S.-E. Park, *Green Chem.*, 2011, **13**, 1416–1421.

118 X. Lan, Y. Li, C. Du, T. She, Q. Li and G. Bai, *Chem. – Eur. J.*, 2019, **25**, 8560–8569.

119 A. J. Kamphuis, F. Picchioni and P. P. Pescarmona, *Green Chem.*, 2019, **21**, 406–448.

120 Z. Huang, F. Li, B. Chen and G. Yuan, *Catal. Sci. Technol.*, 2016, **6**, 2942–2948.

121 M. B. Ansari, B.-H. Min, Y.-H. Mo and S.-E. Park, *Green Chem.*, 2011, **13**, 1416–1421.

122 Z. Huang, F. Li, B. Chen, T. Lu, Y. Yuan and G. Yuan, *Appl. Catal., B*, 2013, **136–137**, 269–277.

123 J. Xu, F. Wu, Q. Jiang, J.-K. Shang and Y.-X. Li, *J. Mol. Catal. A: Chem.*, 2015, **403**, 77–83.

124 Q. Su, J. Sun, J. Wang, Z. Yang, W. Cheng and S. Zhang, *Catal. Sci. Technol.*, 2014, **4**, 1556–1562.

125 J. Xu, F. Wu, Q. Jiang and Y.-X. Li, *Catal. Sci. Technol.*, 2015, **5**, 447–454.

126 D.-H. Lan, H.-T. Wang, L. Chen, C.-T. Au and S.-F. Yin, *Carbon*, 2016, **100**, 81–89.

127 Q. Su, X. Yao, W. Cheng and S. Zhang, *Green Chem.*, 2017, **19**, 2957–2965.

128 X. Li, B. Lin, H. Li, Q. Yu, Y. Ge, X. Jin, X. Liu, Y. Zhou and J. Xiao, *Appl. Catal., B*, 2018, **239**, 254–259.

129 J. Zhu, T. Diao, W. Wang, X. Xu, X. Sun, S. A. C. Carabineiro and Z. Zhao, *Appl. Catal., B*, 2017, **219**, 92–100.

130 T. Biswas and V. Mahalingam, *New J. Chem.*, 2017, **41**, 14839–14842.

131 Z. Sun, N. Talreja, H. Tao, J. Texter, M. Muhler, J. Strunk and J. Chen, *Angew. Chem., Int. Ed.*, 2018, **57**, 7610–7627.

132 A. A. Tountas, X. Peng, A. V. Tavasoli, P. N. Duchesne, T. L. Dingle, Y. Dong, L. Hurtado, A. Mohan, W. Sun, U. Ulmer, L. Wang, T. E. Wood, C. T. Maravelias, M. M. Sain and G. A. Ozin, *Adv. Sci.*, 2019, **6**, 1801903.

133 M. Khalil, J. Gunlazuardi, T. A. Ivandini and A. Umar, *Renewable Sustainable Energy Rev.*, 2019, **113**, 109246.

134 Z. Wang, C. Li and K. Domen, *Chem. Soc. Rev.*, 2019, **48**, 2109–2125.

135 M.-H. Vu, M. Sakar, S. A. Hassanzadeh-Tabrizi and T.-O. Do, *Adv. Mater. Interfaces*, 2019, **6**, 1900091.

136 J. Kou, C. Lu, J. Wang, Y. Chen, Z. Xu and R. S. Varma, *Chem. Rev.*, 2017, **117**, 1445–1514.

137 R. N. Compton, P. W. Reinhardt and C. D. Cooper, *J. Chem. Phys.*, 1975, **63**, 3821–3827.

138 N.-N. Vu, S. Kaliaguine and T.-O. Do, *Adv. Funct. Mater.*, 2019, **29**, 1901825.

139 K. Li, B. Peng and T. Peng, *ACS Catal.*, 2016, **6**, 7485–7527.

140 T. Inoue, A. Fujishima, S. Konishi and K. Honda, *Nature*, 1979, **277**, 637–638.

141 J. Fu, K. Jiang, X. Qiu, J. Yu and M. Liu, *Mater. Today*, 2019, **32**, 222–243.

142 N. Sasirekha, S. J. S. Basha and K. Shanthi, *Appl. Catal., B*, 2006, **62**, 169–180.

143 K. Mori, H. Yamashita and M. Anpo, *RSC Adv.*, 2012, **2**, 3165–3172, DOI: 10.1039/C2RA01332K.

144 I. A. Shkrob, T. W. Marin, H. Y. He and P. Zapol, *J. Phys. Chem. C*, 2012, **116**, 9450–9460.

145 L. B. Hoch, P. Szymanski, K. K. Ghuman, L. He, K. Liao, Q. Qia, L. M. Reyes, Y. Zhu, M. A. El-Sayed, C. V. Singh and G. A. Ozin, *Proc. Natl. Acad. Sci. U. S. A.*, 2016, **113**, E8011–E8020.

146 W. Tu, Y. Xu, J. Wang, B. Zhang, T. Zhou, S. Yin, S. Wu, C. Li, Y. Huang, Y. Zhou, Z. Zou, J. Robertson, M. Kraft and R. Xu, *ACS Sustainable Chem. Eng.*, 2017, **5**, 7260–7268.

147 S. C. Bhatia, *Advanced Renewable Energy Systems*, 2014, pp. 32–67.

148 G. M. Hasselman, D. F. Watson, J. R. Stromberg, D. F. Bocian, D. Holten, J. S. Lindsey and G. J. Meyer, *J. Phys. Chem. B*, 2006, **110**, 25430–25440.

149 S. N. Habisreutinger, L. Schmidt-Mende and J. K. Stolarczyk, *Angew. Chem., Int. Ed.*, 2013, **52**, 7372–7408.

150 H. Lang, S. Zhang and Z. Liu, *Phys. Rev. B*, 2016, **94**, 235306.

151 L. Liu, H. Zhao, J. M. Andino and Y. Li, *ACS Catal.*, 2012, **2**, 1817–1828.

152 X. Chang, T. Wang and J. Gong, *Energy Environ. Sci.*, 2016, **9**, 2177–2196.

153 Z. Sun, H. Wang, Z. Wu and L. Wang, *Catal. Today*, 2018, **300**, 160–172.

154 J. Chen, Y.-F. Li, P. Sit and A. Selloni, *J. Am. Chem. Soc.*, 2013, **135**, 18774–18777.

155 O. Ola and M. M. Maroto-Valer, *J. Photochem. Photobiol. C*, 2015, **24**, 16–42.

156 K. Li, X. An, K. H. Park, M. Khraisheh and J. Tang, *Catal. Today*, 2014, **224**, 3–12.

157 X. Li, J. Yu, M. Jaroniec and X. Chen, *Chem. Rev.*, 2019, **119**, 3962–4179.

158 J. Ran, M. Jaroniec and S.-Z. Qiao, *Adv. Mater.*, 2018, **30**, 1704649.

159 N. Syed, J. Huang, Y. Feng, X. Wang and L. Cao, *Front. Chem.*, 2019, **7**(713), 1–7.

160 J. Z. Y. Tan and M. M. Maroto-Valer, *J. Mater. Chem. A*, 2019, **7**, 9368–9385.

161 L. Wang, W. Chen, D. Zhang, Y. Du, R. Amal, S. Qiao, J. Wu and Z. Yin, *Chem. Soc. Rev.*, 2019, **48**, 5310–5349.



162 J. Fu, J. Yu, C. Jiang and B. Cheng, *Adv. Energy Mater.*, 2018, **8**, 1701503.

163 J. K. Stolarczyk, S. Bhattacharyya, L. Polavarapu and J. Feldmann, *ACS Catal.*, 2018, **8**, 3602–3635.

164 M. M. Kandy, *Sustainable Energy Fuels*, 2020, **4**, 469–484.

165 S. Ye, R. Wang, M.-Z. Wu and Y.-P. Yuan, *Appl. Surf. Sci.*, 2015, **358**, 15–27.

166 G. Dong and L. Zhang, *J. Mater. Chem.*, 2012, **22**, 1160–1166.

167 J. Mao, T. Peng, X. Zhang, K. Li, L. Ye and L. Zan, *Catal. Sci. Technol.*, 2013, **3**, 1253–1260.

168 P. Niu, Y. Yang, J. C. Yu, G. Liu and H.-M. Cheng, *Chem. Commun.*, 2014, **50**, 10837–10840.

169 Y.-P. Yuan, S.-W. Cao, Y.-S. Liao, L.-S. Yin and C. Xue, *Appl. Catal., B*, 2013, **140–141**, 164–168.

170 K. Maeda, R. Kuriki, M. Zhang, X. Wang and O. Ishitani, *J. Mater. Chem. A*, 2014, **2**, 15146–15151.

171 J. Qin, S. Wang, H. Ren, Y. Hou and X. Wang, *Appl. Catal., B*, 2015, **179**, 1–8.

172 K. Wang, Q. Li, B. Liu, B. Cheng, W. Ho and J. Yu, *Appl. Catal., B*, 2015, **176–177**, 44–52.

173 J. Fu, B. Zhu, C. Jiang, B. Cheng, W. You and J. Yu, *Small*, 2017, **13**, 1603938.

174 B. Liu, L. Ye, R. Wang, J. Yang, Y. Zhang, R. Guan, L. Tian and X. Chen, *ACS Appl. Mater. Interfaces*, 2018, **10**, 4001–4009.

175 D. Vidyasagar, N. Manwar, A. Gupta, S. G. Ghugal, S. S. Umare and R. Boukherroub, *Catal. Sci. Technol.*, 2019, **9**, 822–832.

176 S. Roy and E. Reisner, *Angew. Chem., Int. Ed.*, 2019, **58**, 12180–12184.

177 H. Shi, S. Long, J. Hou, L. Ye, Y. Sun, W. Ni, C. Song, K. Li, G. G. Gurzadyan and X. Guo, *Chem. – Eur. J.*, 2019, **25**, 5028–5035.

178 M. Li, S. Zhang, X. Liu, J. Han, X. Zhu, Q. Ge and H. Wang, *Eur. J. Inorg. Chem.*, 2019, 2058–2064.

179 G. Zhang, G. Li, T. Heil, S. Zafeiratos, F. Lai, A. Savateev, M. Antonietti and X. Wang, *Angew. Chem., Int. Ed.*, 2019, **58**, 3433–3437.

180 S. Wan, M. Ou, X. Wang, Y. Wang, Y. Zeng, J. Ding, S. Zhang and Q. Zhong, *Dalton Trans.*, 2019, **48**, 12070–12079.

181 J.-Y. Tang, X. Y. Kong, B.-J. Ng, Y.-H. Chew, A. R. Mohamed and S.-P. Chai, *Catal. Sci. Technol.*, 2019, **9**, 2335–2343.

182 J. Fu, K. Liu, K. Jiang, H. Li, P. An, W. Li, N. Zhang, H. Li, X. Xu, H. Zhou, D. Tang, X. Wang, X. Qiu and M. Li, *Adv. Sci.*, 2019, **6**, 1900796.

183 A. Hayat, J. Khan, M. U. Rahman, S. B. Mane, W. U. Khan, M. Sohail, N. U. Rahman, N. Shaista, Z. Chi and M. Wu, *J. Colloid Interface Sci.*, 2019, **548**, 197–205.

184 K. Wang, J. Fu and Y. Zheng, *Appl. Catal., B*, 2019, **254**, 270–282.

185 N. Tian, K. Xiao, Y. Zhang, X. Lu, L. Ye, P. Gao, T. Ma and H. Huang, *Appl. Catal., B*, 2019, **253**, 196–205.

186 X. Liu, P. Wang, H. Zhai, Q. Zhang, B. Huang, Z. Wang, Y. Liu, Y. Dai, X. Qin and X. Zhang, *Appl. Catal., B*, 2018, **232**, 521–530.

187 S. Wan, M. Ou, Q. Zhong and W. Cai, *Carbon*, 2018, **138**, 465–474.

188 X. Gong, S. Yu, M. Guan, X. Zhu and C. Xue, *J. Mater. Chem. A*, 2019, **7**, 7373–7379.

189 H. Ou, C. Tang, Y. Zhang, A. M. Asiri, M.-M. Titirici and X. Wang, *J. Catal.*, 2019, **375**, 104–112.

190 J.-Y. Tang, W.-G. Zhou, R.-T. Guo, C.-Y. Huang and W.-G. Pan, *Catal. Commun.*, 2018, **107**, 92–95.

191 S. Cao, Y. Li, B. Zhu, M. Jaroniec and J. Yu, *J. Catal.*, 2017, **349**, 208–217.

192 M. Humayun, Q. Fu, Z. Zheng, H. Li and W. Luo, *Appl. Catal., A*, 2018, **568**, 139–147.

193 W.-J. Ong, L.-L. Tan, S.-P. Chai and S.-T. Yong, *Dalton Trans.*, 2015, **44**, 1249–1257.

194 K. Takanabe, *J. Catal.*, 2019, **370**, 480–484.

195 P. V. Kamat and S. Jin, *ACS Energy Lett.*, 2018, **3**, 622–623.

196 Q. Wang and K. Domen, *Chem. Rev.*, 2020, **120**, 919–985.

197 P. V. Kamat and J. M. Buriak, *ACS Energy Lett.*, 2019, **4**, 2473–2474.

198 J. M. Buriak, P. V. Kamat and K. S. Schanze, *ACS Appl. Mater. Interfaces*, 2014, **6**, 11815–11816.

199 M. Melchionna and P. Fornasiero, *ACS Catal.*, 2020, **10**, 5493–5501.

200 J. Albero, Y. Peng and H. García, *ACS Catal.*, 2020, **10**, 5734–5749.

201 G. Peng, J. Albero, H. García and M. Shalom, *Angew. Chem., Int. Ed.*, 2018, **57**, 15807–15811.

202 G. Peng, J. Qin, M. Volokh and M. Shalom, *ACS Appl. Mater. Interfaces*, 2019, **11**, 29139–29146.

203 G. Peng, J. Qin, M. Volokh, C. Liu and M. Shalom, *J. Mater. Chem. A*, 2019, **7**, 11718–11723.

204 Y. Fang, X. Li and X. Wang, *ACS Catal.*, 2018, **8**, 8774–8780.

205 W. Xiong, F. Huang and R.-Q. Zhang, *Sustainable Energy Fuels*, 2020, **4**, 485–503.

206 J. Safaei, N. A. Mohamed, M. F. M. Noh, M. F. Soh, N. A. Ludin, M. A. Ibrahim, W. N. R. W. Isahak and M. A. M. Teridi, *J. Mater. Chem. A*, 2018, **6**, 22346–22380.

207 D. D. Zhu, J. L. Liu and S. Z. Qiao, *Adv. Mater.*, 2016, **28**, 3423–3452.

208 R. J. Lim, M. Xie, M. A. Sk, J. M. Lee, A. Fisher, X. Wang and K. H. Lim, *Catal. Today*, 2014, **233**, 169–180.

209 J. E. Pander, D. Ren and B. S. Yeo, *Catal. Sci. Technol.*, 2017, **7**, 5820–5832.

210 Y. Hori, H. Konishi, T. Futamura, A. Murata, O. Koga, H. Sakurai and K. Oguma, *Electrochim. Acta*, 2005, **50**, 5354–5369.

211 S. Trasatti and O. A. Petrii, *J. Electroanal. Chem.*, 1992, **327**, 353–376.

212 A. J. Bard and L. R. Faulkner, *Electrochemical Methods: Fundamentals and applications*, John Wiley & Sons, Inc., 2nd edn, 2001.



213 N. Sagara, S. Kamimura, T. Tsubota and T. Ohno, *Appl. Catal., B*, 2016, **192**, 193–198.

214 C. M. S-Sánchez, V. Montiel, D. A. Tryk, A. Aldaz and A. Fujishima, *Pure Appl. Chem.*, 2001, **73**, 1917–1927.

215 B. Zhang, T.-J. Zhao, W.-J. Feng, Y.-X. Liu, H.-H. Wang, H. Su, L.-B. Lv, X.-H. Li and J.-S. Chen, *Nano Res.*, 2018, **11**, 2450–2459.

216 X. Lu, T. H. Tan, Y. H. Ng and R. Amal, *Chem. – Eur. J.*, 2016, **22**, 11991–11996.

217 S. Zhao, Z. Tang, S. Guo, M. Han, C. Zhu, Y. Zhou, L. Bai, J. Gao, H. Huang, Y. Li, Y. Liu and Z. Kang, *ACS Catal.*, 2017, **8**, 188–197.

218 Y. Jiao, Y. Zheng, P. Chen, M. Jaroniec and S.-Z. Qiao, *J. Am. Chem. Soc.*, 2017, **139**, 18093–18100.

219 J. Xu, Y. Kan, R. Huang, B. Zhang, B. Wang, K. H. Wu, Y. Lin, X. Sun, Q. Li, G. Centi and D. Su, *ChemSusChem*, 2016, **9**, 1085–1089.

220 L. Zhang, F. Mao, L. R. Zheng, H. F. Wang, X. H. Yang and H. G. Yang, *ACS Catal.*, 2018, **8**, 11035–11041.

221 Z. Ma, C. Lian, D. Niu, L. Shi, S. Hu, X. Zhang and H. Liu, *ChemSusChem*, 2019, **12**, 1724–1731.

222 N. Meng, W. Zhou, Y. Yu, Y. Liu and B. Zhang, *ACS Catal.*, 2019, **9**, 10983–10989.

